Strangelet Searches in Pb + Pb Collisions at $158 \cdot A$ GeV/c

Inauguraldissertation
der Philosophisch-naturwissenschaftlichen Fakultät
der Universität Bern

vorgelegt von
Michael Weber
von Willadingen BE

Leiter der Arbeit: Prof.Dr.K.Pretzl
Laboratorium für Hochenergiephysik

Strangelet Searches in Pb + Pb Collisions at $158 \cdot A$ GeV/c

Inauguraldissertation
der Philosophisch-naturwissenschaftlichen Fakultät
der Universität Bern

vorgelegt von
Michael Weber
von Willadingen BE

Leiter der Arbeit: Prof.Dr.K.Pretzl
Laboratorium für Hochenergiephysik

Von der Philosophisch-naturwissenschaftlichen Fakultät angenommen

Der Dekan:

Bern, den 19.4.2001 Prof.Dr.P.Bochsler

Abstract

NA52 is a fixed target experiment at CERN SPS belonging to a series of experiments looking at Pb+Pb collisions at 158 A GeV/c. NA52 identifies particles coming from the collisions at $p_t = 0$ in a 550 m long double bend focussing spectrometer. The main goal is the search for strangelets. Besides this NA52 measures (anti)particles and (anti)nuclei over a wide range of rapidity. In this thesis the final results about the strangelets and some updates regarding the particle searches are presented.

Contents

Chapter 1

Introduction

This thesis is about the final results of the searches for strangelets in heavy ion collisions at CERN SPS by the NA52 experiment. This first chapter gives a short insight into what a strangelet (a droplet of strange quark matter (SQM)) is and what its characteristics are. Further, an overview of the question of the existence of SQM in nature is given. The aim is also to see how the NA52 experiment is positioned in the context of the experimental searches for man-made strangelets.

1.1 Strange quark matter

Known particles appearing in nature or produced in experiments can be classified into leptons and hadrons according to the standard model of elementary particles. The interactions between these particles are described by bosons. Hadrons show up either as mesons, which are pairs of quarks and anti-quarks, or baryons, which are bound states of three quarks. States with a larger number of quarks are not known, although there is no basic principle excluding it. These larger objects of many deeply bound quarks are called *quark matter*. Quark matter has to be distinguished from clusters of hadrons well known as nuclei. It is believed that, besides the up and down quark as constituents of quark matter, also the strange quark plays an important role. If quark matter contains similar amounts of up, down and strange quarks it is called *strange quark matter* (SQM). The anticipated mass range of SQM lies anywhere between the mass of light nuclei and that of neutron stars $A \sim 10^{57}$ (which would then be called *strange stars*). Smaller amounts of SQM are referred to as *droplets of SQM*, or simply *strangelets*. The charge of SQM is expected to be small due to the s-quark content. Their low charge to mass ratio is therefore a prominent experimental signature. However, strangelets might also be neutral or even negatively charged depending on the relative quark content.

Stability and decay modes have been widely investigated [1, 2]. Calculations indicate that SQM tends to be more tightly bound for increasing number of constituent quarks because of the lower energy per baryon.[3, 4]. A calculation of

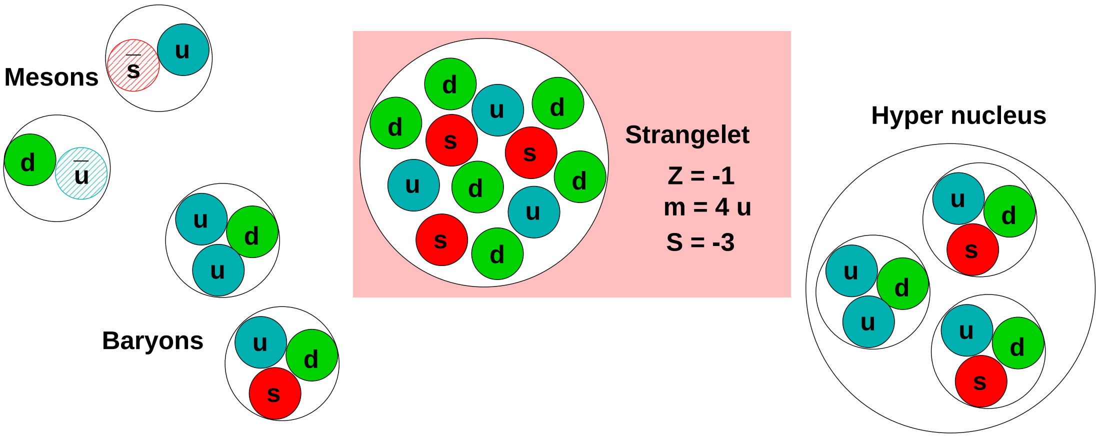

Figure 1.1: Illustration of a strangelet compared to hadronic and hyper nuclear matter. Hadronic matter shows up either as mesons, which are pairs of quarks and antiquarks, or baryons, which are bound states of three quarks. Strangelets are deeply bound states of many u,d and s quarks. They also have to be distinguished from hyper nuclei, which also consist of u,d and s quarks, but the quarks are grouped to baryons.

the energy per baryon as a function of the baryon number within a (MIT-)Bag model is shown in figure 1.2. On the other hand there are predictions that also small strangelets might gain stability due to shell effects [6, 7]. For experimental searches of man-induced strangelets, the stability as well as the production probability has to be considered (see section 1.1.2). A more inclusive overview and the status quo on SQM including experimental searches can be found in [8] and comprehensive introductions to theoretical issues in [9, 10].

1.1.1 The existence of SQM in nature

First ideas about the existence of quark matter were published by Bodmer (1971)[11] under the title 'Collapsed Nuclei'. According to those ideas, collapsed nuclei have a higher density than ordinary nuclei and may also have a lower energy level. The spontaneous decay of nuclei into these collapsed states is inhibited by a saturation barrier which prolongs the lifetime of nuclei to more than 10^{14} times the age of the universe. It is presumed that such collapsed states were created in the initial extremely hot and dense stages of the Universe and part of them may still exist somewhere [12]. If SQM were produced during the Big-bang and is stable, we should be able even today to detect it in cosmic rays and terrestrial or extraterrestrial matter. In cosmic ray experiments a class of unusual events called *Centauro* events is known. These events are considered to be related to the existence of SQM.

SQM could also be an invisible component of the cosmic radiation [13] contributing to the dark matter mass in the Universe. Although 'dark', it could leave

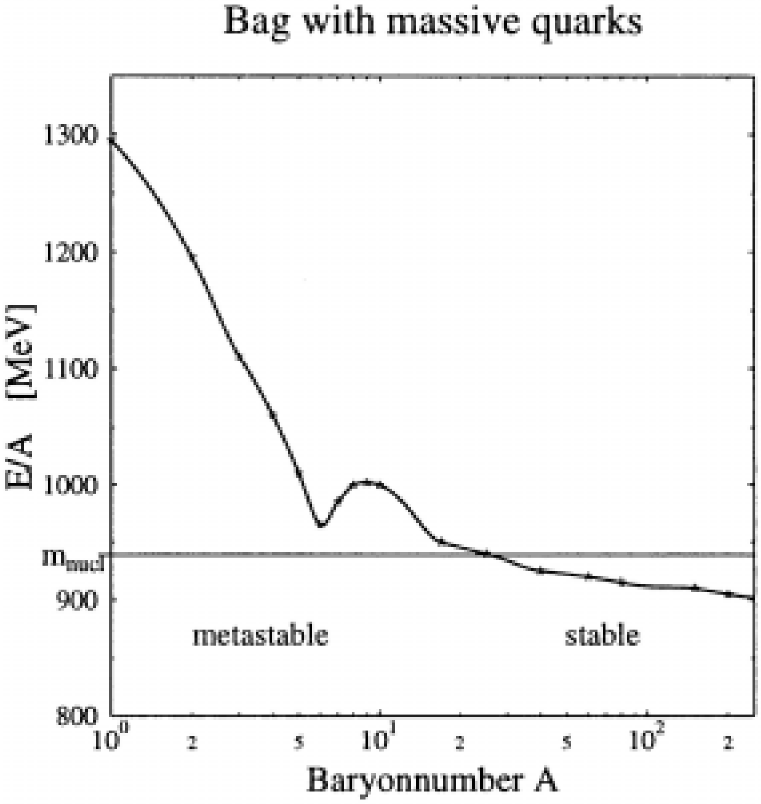

Figure 1.2: Energy per baryon versus baryon number from a calculation within the (MIT-)Bag model with non interacting quarks. Equal number of u,d and s quarks are assumed ($m_s = 150$ GeV$/c^2$, $B^{1/4} = 145$ MeV). Taken from [5].

anomalous traces in rocks or meteorites. In experimental searches [14] no candidate has shown up.

The possibility of SQM being part of terrestrial material has also been investigated [15, 16, 17]. But again only negative results have been presented.

Even if SQM was not produced in the early stages of the Universe, there are further possibilities that it could exist in nature, e.g. in neutron stars. Under the large pressure in the core of neutron stars, nuclear matter may be converted to two-flavour quark matter which might achieve a higher stability through conversion to SQM. Rotating neutron stars (pulsars) might therefore be rotating strange stars. Experimentally this would be detected by an acceleration in the spin (spin-up) during the phase transition. Up to now no spin-up has been observed. However, the phase transition takes little time compared to the life of a neutron star, pulsars are rare and the measurement of the spin-up is quite difficult. In my opinion, this is the most promising field to find SQM in the near future.

1.1.2 Strangelets produced in experiments

SQM which could be produced in experiments typically contains small amounts of quarks, therefore one speaks about strangelets. The smallest strangelet is the H^0 dibaryon which was first proposed by Jaffe in 1977 [18]. It is a neutral flavour-singlet uuddss-state with parity $J^P = 0^+$ and a mass of $m \approx 2150$ MeV$/c^2$. Many searches for the H^0 have been performed. First experiments studied the kinematics of $\Lambda - \Lambda$ production [19] in Σ^- capture on light nuclei. Also, a six quark resonance in p-p reactions [20] or recoil H^0 in strangeness exchange reactions [21, 22, 23] were being searched for. No unambiguous signal has been seen.

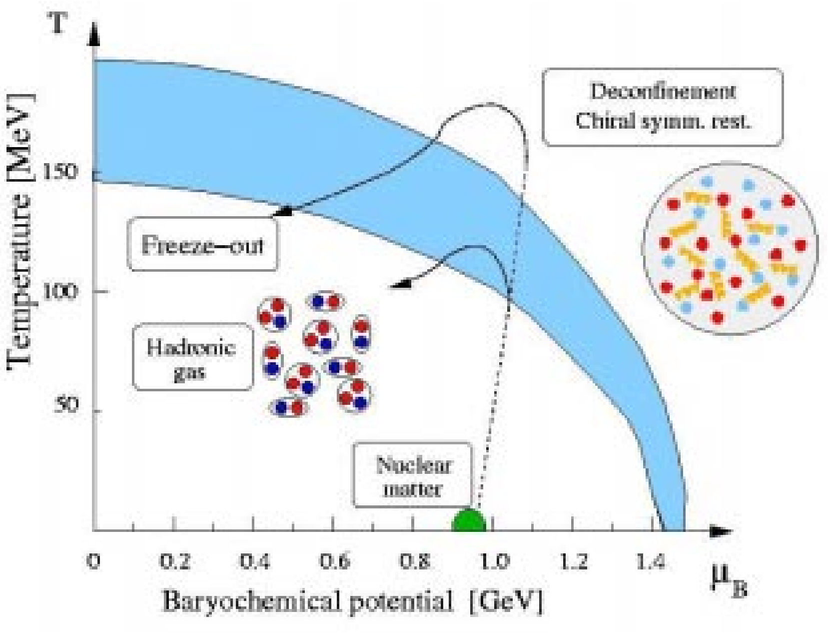

Figure 1.3: Phase diagram of matter with limits to the QGP phase and the history of the transition in a heavy ion collision.

More general searches for SQM were undertaken with the advent of heavy ion beams. Gold and silicon beams became available at the AGS at BNL and oxygen, sulfur and lead beams at the SPS at CERN. Collisions of the heavy ions promised to be a good environment for the search for light lumps of quark matter [24]. The NA52 experiment, whose results are presented in this thesis, is the strangelet experiment at the CERN SPS.

Several production models for SQM in heavy ions collisions have been proposed. One of them is production through coalescence. The idea is that a group of

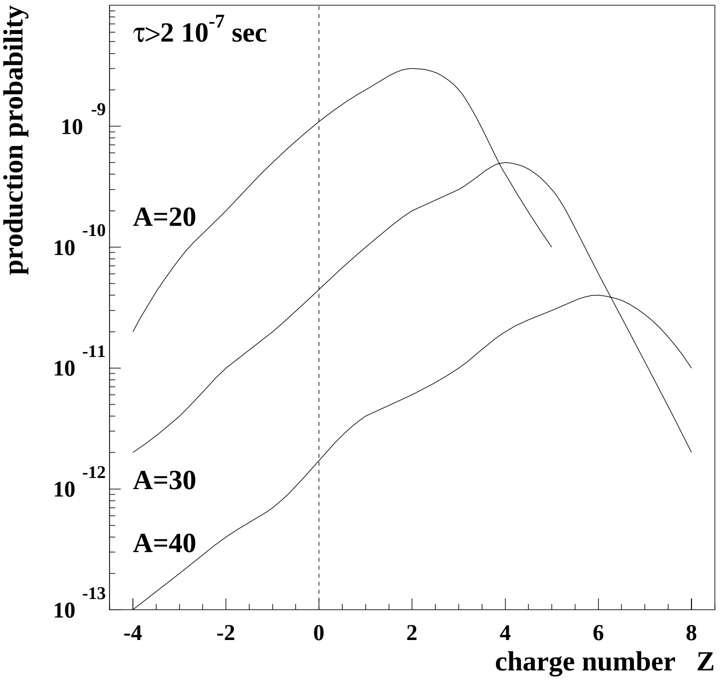

Figure 1.4: Quantitative production probabilities for strangelets in Pb+Pb collisions at $\sqrt{s} = 17A$GeV by Crawford et al. [25]. A selection of the highest production probabilities is shown.

quarks coming from the collision fly nearby in phase space and can merge to form a strangelet [27]. Other thermal production models involve an intermediate quark gluon plasma (QGP) state. The QGP phase could be reached in heavy ion collisions as shown in figure 1.3. In this case strangelets are regarded as cool remnants of the QGP phase. The copious production of strangelets in heavy ion collisions is even a proposed signature for the production of a QGP phase. In this model, the larger amount of up- and down-quarks with respect to anti-quarks leads in this model to an increased hadronisation of $\bar{s}$-quarks and so to an enrichment (distillation) of s quarks [28]. This will enhance the possibility for the production of a strangelet (as a drop) during the cooling of the QGP phase. Quantitative production probabilities for strangelets in Pb+Pb collisions were calculated by Crawford et al. [25]. A selection of the highest production probabilities for strangelets with lifetime $\tau > 10^{-7}$ sec and baryonic number 20,30 and 40 is shown in figure 1.4.

Later calculations [26, 29] favour the detection of negatively charged strangelets if one includes decay schemes and stability. For each such stable strangelets the charge fraction Z/A versus baryon number is shown in figure 1.5.

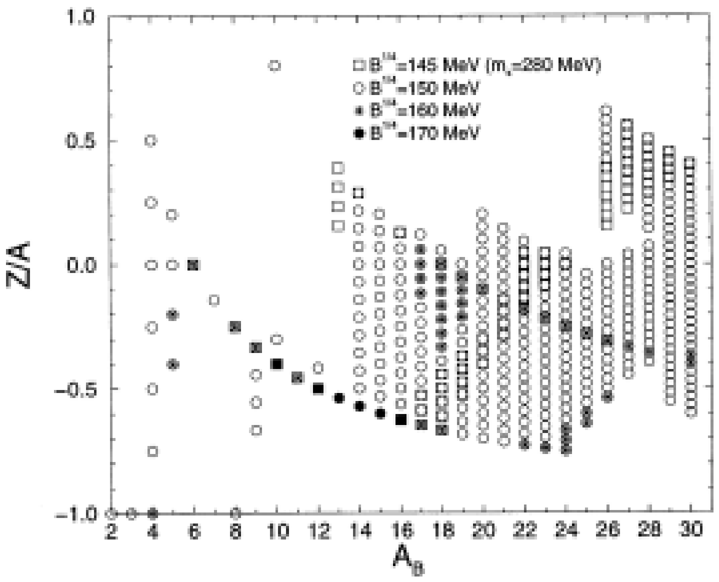

Figure 1.5: Charge fraction Z/A for long-lived strangelets for different choices of the bag parameter B (taken from [26]).

Reports on searches from the AGS can be found in [30](BNL-AGS-E814), [31] E858, [32] E886, [33] E878. One experiment also looked at neutral strangelets [34] E864. To date, no gold plated strangelet candidate appeared. The production of the neutral H^0 has also been studied in heavy ion collisions [35] and experimental searches performed by E810 [36, 37], E888 [38, 39] and E896 [40] which are still ongoing. No conclusive evidence could be provided.

Chapter 2

NA52 experimental setup

NA52 uses the H6 beam line at the CERN SPS as a 550m long double bend focusing spectrometer. The spectrometer transports charged secondary particles coming from the Pb+Pb collisions with a rigidity p/Z selectable between ± 5 and ± 200 GeV/c. It looks at a production angle of 0 mrad with an acceptance of approximately 5μsr%. The acceptance is treated in detail in section 2.1. A schematic layout of the experimental setup is shown in figure 2.1. The positions of the detectors along the beam line are listed in table 2.1. For the tracks reaching at least the counter B1 (trigger) located at $L/c = 0.9\mu$s behind the target, full particle identification can be performed.

Various time of flight stations (TOFx and Bx) allow the reconstruction of the mass to charge ratio at a given rigidity. These counters also allow the reconstruction of the charge by the energy loss measurement. Other detector elements like a segmented hadronic calorimeter and a differential Čerenkov counter (CEDAR) add redundancy to the charge and mass measurements.
A set of multi wire proportional chambers (MWPC) has also been used for tracking and rejection of events with multiple particles in the beam line.
The detector elements with relevant features for the results presented in this thesis are described in appendix B. Further information about the experimental setup can be found in [41].

2.1 Acceptance of the spectrometer

Since we give differential cross sections as physics results it is necessary to know the acceptance of the H6 beam line. To get the acceptance two methods can be used. On the one hand a simulation can be done and on the other hand also the measured data can be used to get an estimation of the acceptance.
The TURTLE program [42] simulates the tracks of individual particles through the beam line. TURTLE allows to determine losses due to finite aperture sizes

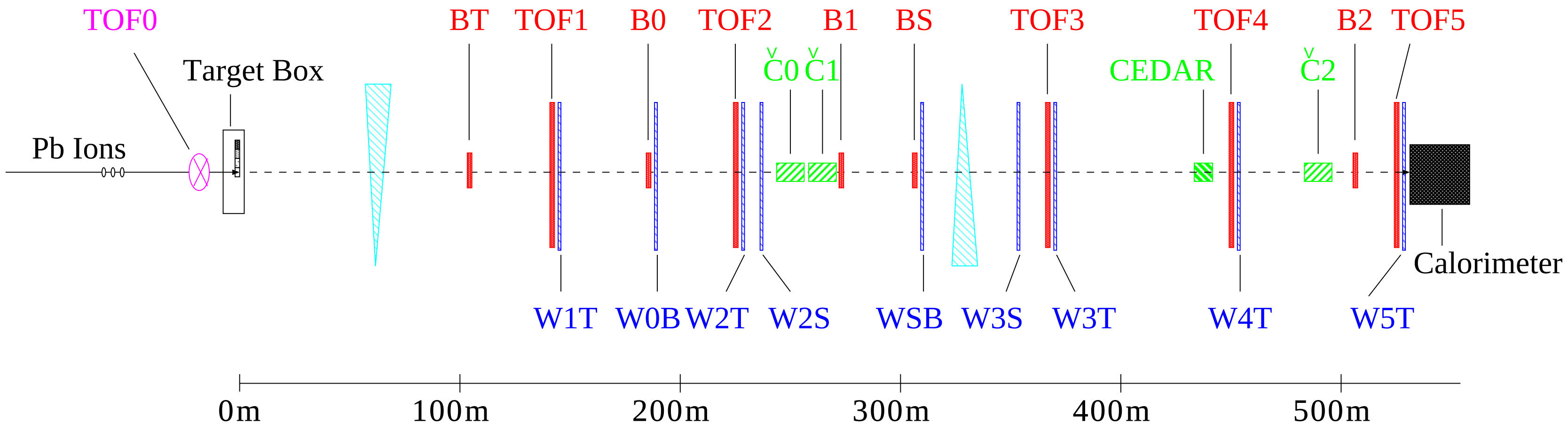

Figure 2.1: NA52 experimental setup in 1998. The position of the detectors along the 550m spectrometer is shown. TOFx and Bx are time of flight stations, Čx threshold Čerenkov counters and Wxx multi wire proportional chambers.

Name	Type	Distance L/c from target in ns	Distance L from target in m
TOF0	Segmented quartz	-3.54	-1.08
T4	Target	0.0	0.0
BT	Scintillator	347.7	104.2
TOF1	Scintillator hodoscope	479.5	143.8
W1T	MWPC	481.2	144.3
B0	Scintillator	636.7	190.9
W0B	MWPC	638.4	191.4
TOF2	Scintillator hodoscope	755.3	226.4
W2T	MWPC	757.0	226.9
W2S	MWPC	798.8	239.5
C0	Threshold Čerenkov	851.9	255.4
C1	Threshold Čerenkov	894.2	268.1
B1	Scintillator	894.7	268.2
BS	Scintillator	1014.5	304.1
WSB	MWPC	1016.1	304.6
W3S	MWPC	1181.5	354.2
TOF3	Scintillator hodoscope	1224.5	367.1
W3T	MWPC	1226.1	367.6
C1	Differential Čerenkov	1480.0	443.7
TOF4	Scintillator hodoscope	1482.7	444.5
W4T	MWPC	1484.4	445.0
C2	Threshold Čerenkov	1685.2	505.2
B2	Scintillator	1685.8	505.4
TOF5	Scintillator hodoscope	1726.4	517.5
W5T	MWPC	1728.0	518.0
Calorimeter	Hadronic calorimeter	1746.5	523.6

Table 2.1: Position of the detectors along the beam line.

and the widening of the beam due to multiple scattering. To get the acceptance in solid angle and momentum, a defined number of particles with wide angular and momentum spread is fed to TURTLE. From the fraction of particles reaching a certain position one deduces the acceptance. As a result iso-transmission lines can be drawn as a function of the polar angle and momentum deviation at the target. Results of a simulation of the acceptances up to B1 and TOF3 at -40 GeV/c rigidity in 1998 are shown in the figures 2.3 and 2.2 (by R. Klingenberg). In this simulation the nominal settings of the magnet currents have been taken. The differences to a simulation taking actual currents after the beam steering are below 2%, which is small compared to the overall systematic error estimated to be 20%.

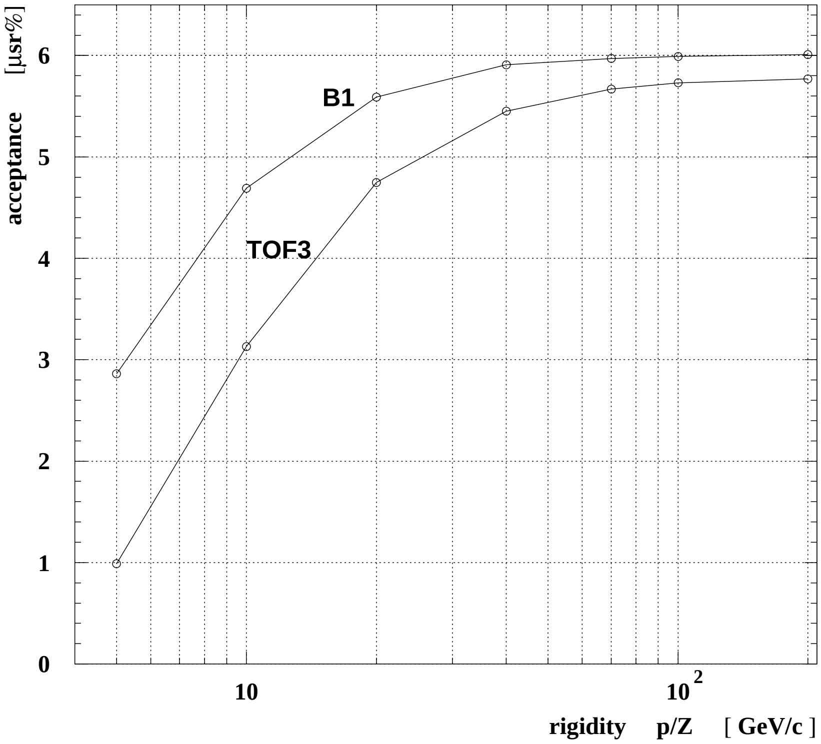

Figure 2.2: The acceptance of the H6 beam line for different track length requirements (B1,TOF3) as a function of the particle rigidity as obtained from the simulation (by R. Klingenberg).

Besides the simulations also measurements can give a hint on the acceptance. The information from the MWPCs allows to trace back the tracks to the target. The distributions of momenta and angular deviations at the target include the information about the acceptance, although biased by the phase space distribution of the considered particles. Assuming the phase space distribution to be wide compared to the acceptance, these values can be compared to those derived from the trace back of the TURTLE simulated tracks. In addition one has to correct the width of the distributions for the resolution of the fit. This measurement could only be done for a few runs. Dedicated and extensive investigations [43, 41] have shown that in general the few measured acceptances are smaller than the simulated ones. A comparison of the anti proton rates at TOF3 for the 4mm target in 1998 and 1995 has shown, that the actual acceptances has been increased by 15% in 1998. From this a correction factor of 0.66 for the simulated acceptances in 1998 was derived. The so obtained acceptances used for the results are summarised in table 2.1.

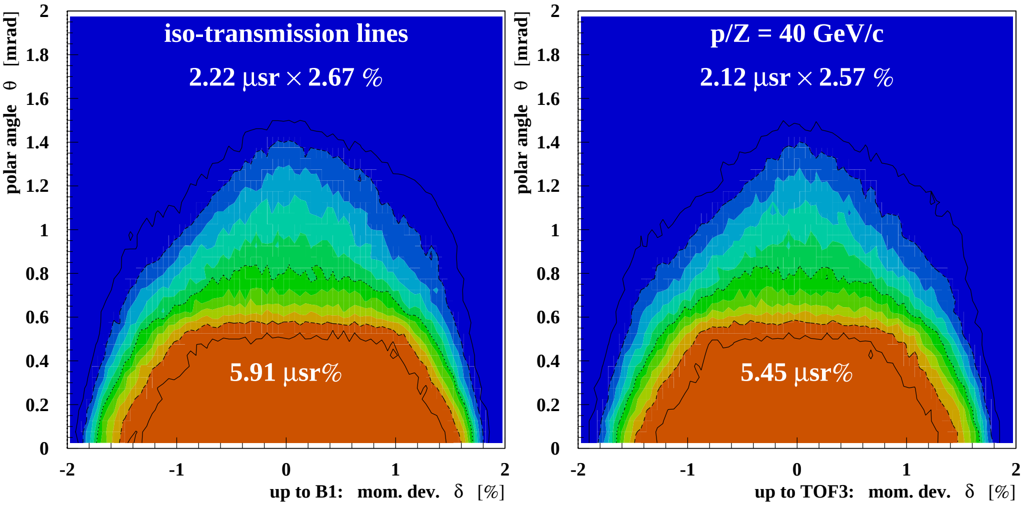

Figure 2.3: Results of a simulation (by R. Klingenberg) of the transmission of particles in terms of their polar angle versus the momentum deviation are shown. The curves correspond to iso-transmission lines of 0.01, 0.1, 0.5, 0.9 and 0.99. The acceptances are calculated as the volumes below this transmission shape. The three plots correspond to tracks up to B1 and TOF3 at -40GeV/c rigidity in 1998. The acceptance slightly decreases for longer tracks especially due to transmission and not due to reduced width of the phase space variables.

	Up to B1			Up to TOF3			Up to TOF5		
p [GeV/c]	$\Delta\Omega$ [μsr]	Δp [%]	α [μsr%]	$\Delta\Omega$ [μsr]	Δp [%]	α [μsr%]	$\Delta\Omega$ [μsr]	Δp [%]	α [μsr%]
-20 GeV/c	1.81	2.14	3.69	1.55	2.02	3.14	1.27	1.79	2.28
-40 GeV/c	1.81	2.17	3.90	1.72	2.08	3.60	1.64	2.07	3.40
-70 GeV/c	1.82	2.17	3.94	1.77	2.10	3.74	1.76	2.11	3.71
-100 GeV/c	1.82	2.17	3.95	1.79	2.11	3.78	1.79	2.11	3.77
-200 GeV/c	1.82	2.18	3.97	1.81	2.11	3.80	1.81	2.11	3.80

Table 2.2: Summary of the acceptances for the H6 beam line used for the results of the 1998 data taking.

2.2 Trigger system

One of the main challenges for the experiment was to cope with the large extension of 550m. Due to this the experimental readout was realized in 2 sections (A upstream to TOF3, and B downstream). Both parts were triggered independently, a coincidence of the two could be required. A trigger condition usually included a coincidence of a TOF hodoscope and a scintillator counter (B1*TOF2 and B2*TOF4) in anti-coincidence with a Čerenkov counter. This last condition was used to select particles with high mass to charge ratio (see section B.1) since we could not record all the particles in the beam line.
The shortest recorded tracks are those reaching the trigger at B1 at 268m (895ns) behind the target. For a given statistics this defines the minimal lifetime for a particle to be seen by NA52. In figure 2.4 the normalised particle rate for charged short-lived particles is shown versus the distance from the target for a 200 GeV/c setting. Kaons with a lifetime of 12 ns are the shortest-lived particles seen by NA52. The next charged candidates, Σ^- and Ξ^- with lifetimes $\tau \approx 10^{-10}$s are not expected to be recorded by NA52 even with a statistics of 10^{13} lead ion collisions and a yield of 100. Besides this we would not be able to distinguish them from anti protons.

2.3 The time of flight (TOF) system

The main part of NA52 is the time of flight system. It consists of a set of time of flight (TOF) scintillator hodoscopes (TOF1-TOF5), the quartz counter (TOF0) and five scintillator counters (BT, BS, B0, B1 and B2). At each trigger (see section 2.2), each of the counters gives a time delay information relative to a particle with nearly speed of light (pion). The time of B2 relative to B1 is also measured to combine all the delay time measurements. Particles are identified calculating the mass to charge ratio from these delay informations versus the counter position (see section 4.2). The resolution of each relative time measurement is better than 100 ps. The calibration was done by means of a 100MHz quartz oscillator. For a more detailed description see [41, 44, 45].
Since the time of flight system is measuring time differences to particles near speed of light, the dynamic range in mass is given by the dynamic range in time of the detector most distant from the trigger (TOF0). The difference in time of flight Δt over the distance from TOF0 to B1 ($L/c = 894.7$ ns) of a particle with mass to charge ratio m/Z compared to a pion (used to calibrate the TOF system) is:

$$\Delta t = 894.7\text{ns} \cdot \left(\frac{1}{2 \cdot (p/Z)^2} \cdot ((m/Z)^2 - m_\pi^2) \right)$$

This time difference has to be smaller than the 120 ns dynamic range of the TOF0 time measurement. A plot of the time delay versus the mass to charge ratio m/Z

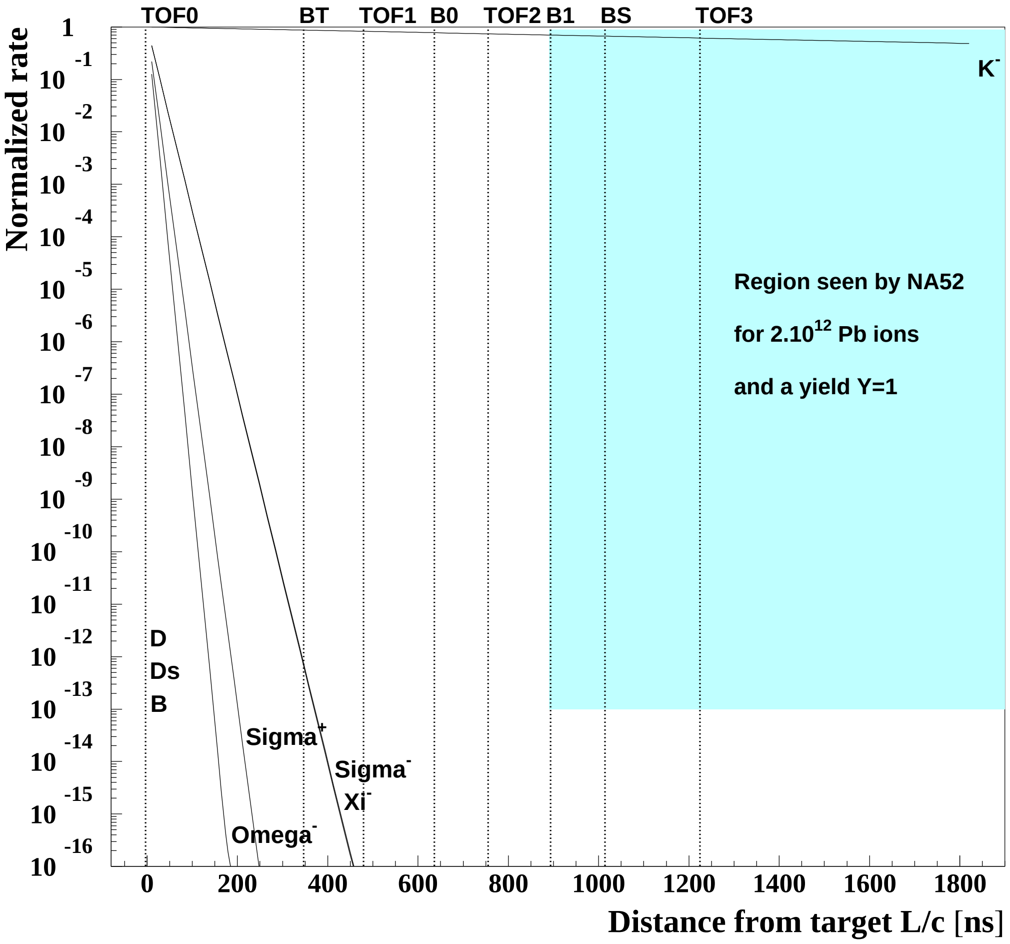

Figure 2.4: Normalised particle rate of different short-lived particles versus the distance from the target for a 200 GeV/c setting. With the accumulated statistics kaons ($\tau = 12$ns) are the shortest-lived charged particles expected to be recorded.

is shown in figure 2.5. The maximal mass to charge ratio which can be detected can also be roughly estimated as:

$$\left.\frac{m}{Z}\right|_{\max} = \frac{1}{2} \cdot \frac{p}{Z}.$$

Please note that often in this work $(m/Z)^2$ is used, which has a dynamic range of:

$$\left(\frac{m}{Z}\right)^2_{\max} = \frac{1}{4} \cdot \left(\frac{p}{Z}\right)^2.$$

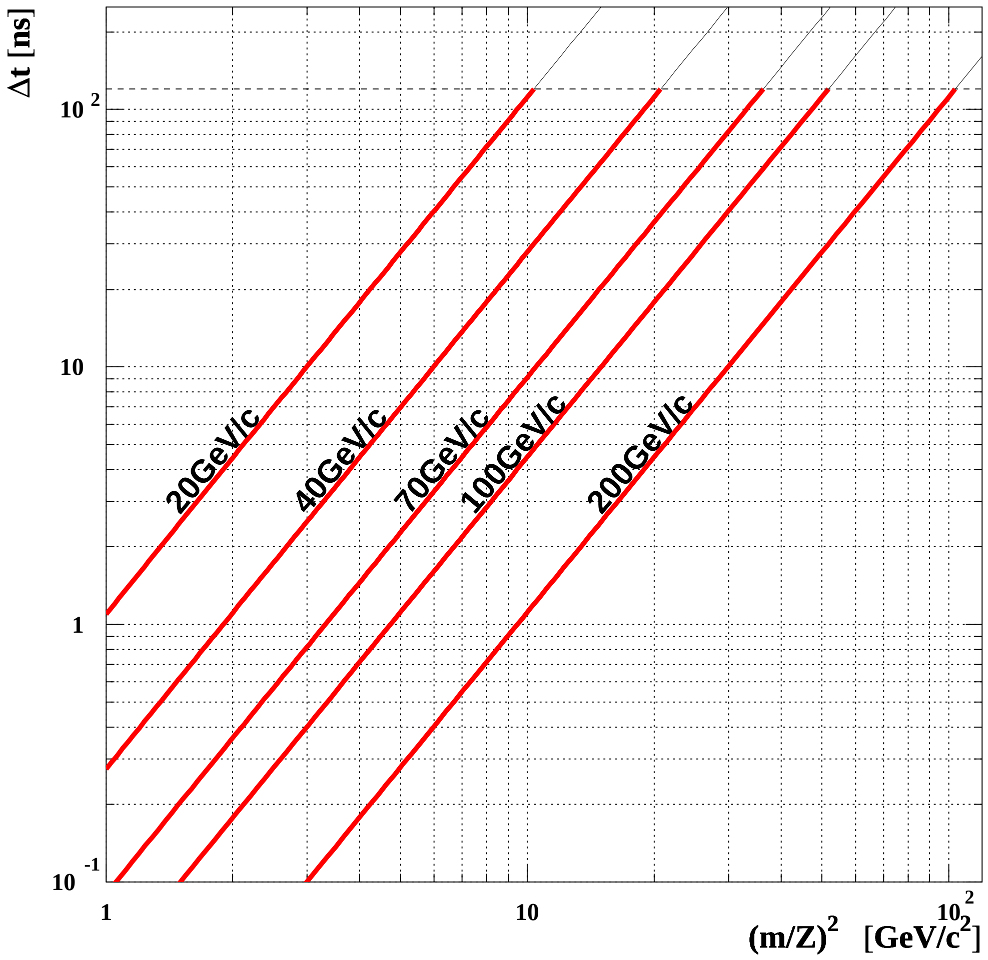

Figure 2.5: Time delay relative to a pion during the flight from TOF0 to B1. The dynamic range for each rigidity is shown as bold line.

2.4 Pulse height measurement

The charge determination is based on the scintillator information. Besides the time of flight information also the "pulse height" is recorded for all the scintillators. What one calls "pulse height" is in fact the integrated signal from the detector indicating the deposited energy. This is used to determine the charge of the particle as the energy deposition goes quadratically with the charge. It is also used to discriminate multi particle events. Redundancy comes from the threshold Čerenkov counters and from the hadronic calorimeter if it is reached. The TOF hodoscopes are set up such that a minimum ionising particle will most probably give a signal which is 1/16th of the dynamic range. Because the measurement is not exactly linear we are able to see charge 5 or even 6. A distribution of measured charges including the information of all the counters can be seen in figure 4.3. Multiple particles in the beam line usually pass through different slabs of the hodoscopes and can therefore even be separated. The scintillators B1 and B2 measured in 1994 up to charge 3 [46]. The other scintillators (BT, B0 and BS) have a special signal shaping which reduces the dynamic range to charge 2. This is an assumption and not measured, since in 1998 we measured at negative rigidities for whose charges $|Z| > 1$ are too scarce. The threshold Čerenkov counters also see double charge as 4 times higher pulse height. The calorimeter sees double charge as double energy since the rigidity (p/Z) is selected by the spectrometer.

Chapter 3

Data taking and accumulated statistics

In this chapter the terms used for different data quantities are explained. Also an overview of the accumulated statistics during the 1998 data taking period will be given. For a summary on the strangelet data takings in 1994 and 1995 see [41] , and for the previous particle search statistics see [44].

First the quantities used to describe the structure and the different amounts of data are described.

The SPS (Super Proton Synchrotron) at CERN delivers pulsed beams. One of these pulses is called a spill. During the lead ion acceleration periods at SPS, one spill has a length of approximately 5 seconds with 14 seconds time between the spills.

A particle produced in a Pb+Pb collision during a spill may travels trough the H6 beam line and reaches our trigger counter. In this case the data of all the detectors is collected by the data acquisition (DAQ) and stored as an event.

The DAQ consists mainly of CAMAC electronics (ADCs, TDCs, MWPC read out) controlled and read out event wise into VME memories. The data of different readout classes (ADCs, wire chambers) are stored in parallel for an entire spill. The events are then built in the spill pauses from the different memories. A very critical point is the correct matching of the data during the online event building. This is checked offline and eventually wrong matches are corrected were possible.

The main data taking quantity for the NA52 experiment is a run. The length of a run is given by a certain amount of data. This typically corresponds to 200 MB of data collected usually in 1 hour of data taking.

The collection of runs taken at the same setting of the beam line (rigidity and target thickness), of the detectors (high voltages, Čerenkov pressures) and of the DAQ (trigger requirements) is called a setting. A setting is usually defined by the type of particles one is measuring. It is the quantity of data used for the presentation of the results and discussion.

A summary of accumulated statistics per setting for the 1998 data taking period

Rigidity [GeV/c]	Target [mm Pb]	Čerenkov mass threshold [GeV/c^2]	Number of Pb ions	Number of interactions
-20	0	0.45	$0.34 \cdot 10^{11}$	–
-20	4	0.45	$4.10 \cdot 10^{11}$	$0.42 \cdot 10^{11}$
-20	8	0.45	$2.07 \cdot 10^{11}$	$0.40 \cdot 10^{11}$
-20	16	0.45	$2.55 \cdot 10^{11}$	$0.90 \cdot 10^{11}$
-20	40	0.84	$1.29 \cdot 10^{12}$	$0.85 \cdot 10^{12}$
-40	0	0.87	$4.39 \cdot 10^{10}$	–
-40	8	0.87	$1.04 \cdot 10^{11}$	$2.02 \cdot 10^{11}$
-40	16	0.87	$4.85 \cdot 10^{10}$	$1.70 \cdot 10^{10}$
-40	40	0.87	$4.65 \cdot 10^{11}$	$3.07 \cdot 10^{11}$
-40	40	1.30	$1.45 \cdot 10^{12}$	$0.96 \cdot 10^{11}$
-70	40	1.32	$1.73 \cdot 10^{12}$	$1.14 \cdot 10^{12}$
-100	40	1.33	$3.33 \cdot 10^{12}$	$2.22 \cdot 10^{12}$
-200	40	0.84	$1.14 \cdot 10^{12}$	$0.75 \cdot 10^{12}$
-200	40	0.84	$1.25 \cdot 10^{11}$	$0.83 \cdot 10^{11}$

Table 3.1: Summary of the accumulated statistics per setting for the 1998 data taking period.

is given in table 3.1.
A compilation and graphical overview of the total data accumulated by NA52 is given in figure 3.1. For this figure all the lead ion interactions accumulated at different target thicknesses for one rigidity have been added up.

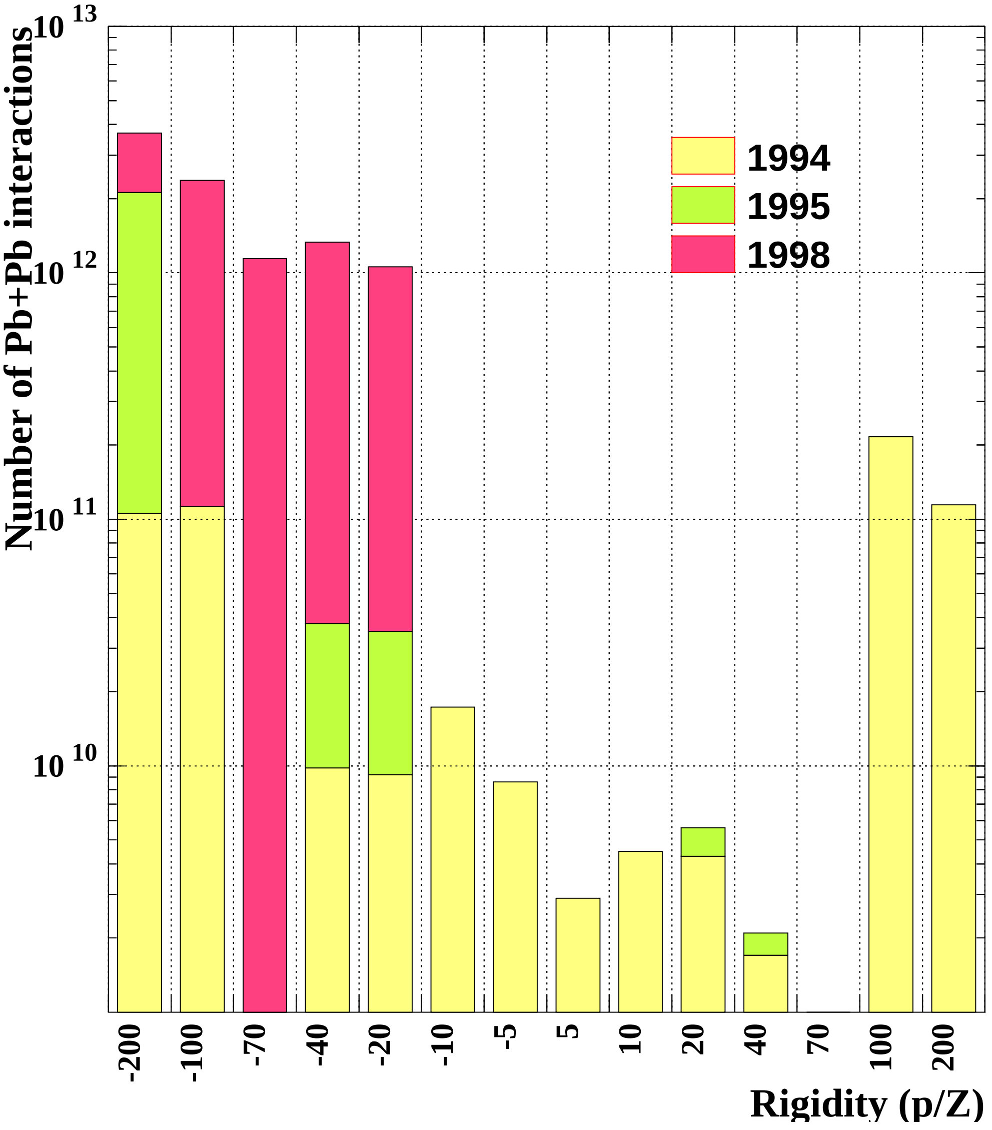

Figure 3.1: Compilation and graphical overview of the total data accumulated by NA52. For this figure all the lead ion interactions accumulated at different target thicknesses for one rigidity have been added up.

Chapter 4

Reconstruction and analysis

The goal of this chapter is to give an insight into the reconstruction methods used. After the selection of usable data, mass and charge are reconstructed from the time and energy loss information of the detectors. Section 4.4 describes how the number of incident lead ions is evaluated accurately. These quantities are used to calculate invariant differential production cross sections as shown in section 4.5. In the last part of the chapter an example of event display is shown, which is used to visualise the recorded data of one event of interest.

4.1 Selection of good data

The data quantities which are checked for their quality are spills. The idea is to keep only spills where the beam line was actually in its nominal setting (magnets or quadrupoles currents, collimators position, etc.) for the analysis. In general the transmissions from the target to B1 (see figure 2.1) and from B1 to B2 are good criteria for this. An example of the distribution of the transmissions from B1 to B2 for all the spills in the -100 GeV/c setting can be found in figure 4.1. This distribution was used to define the window of accepted spills. All the spills with entries inside this window were afterward taken for the various analysis steps.

4.2 Reconstruction of the mass

The mass to charge ratio m/Z is deduced from the slope $a = 1/\beta$ (see figure 4.5) of the time delay measurements t to a fast particle (pion) versus the position in the beam line L/c at a given rigidity $R = p/Z$:

$$\frac{m}{Z} = R \cdot \sqrt{a^2 - 1} = R \cdot \sqrt{1/\beta^2 - 1}.$$

The mass is calculated from m/Z using the measured charge (see section 4.3). For the determination of the mass to charge ratio, the fit is done multiple times.

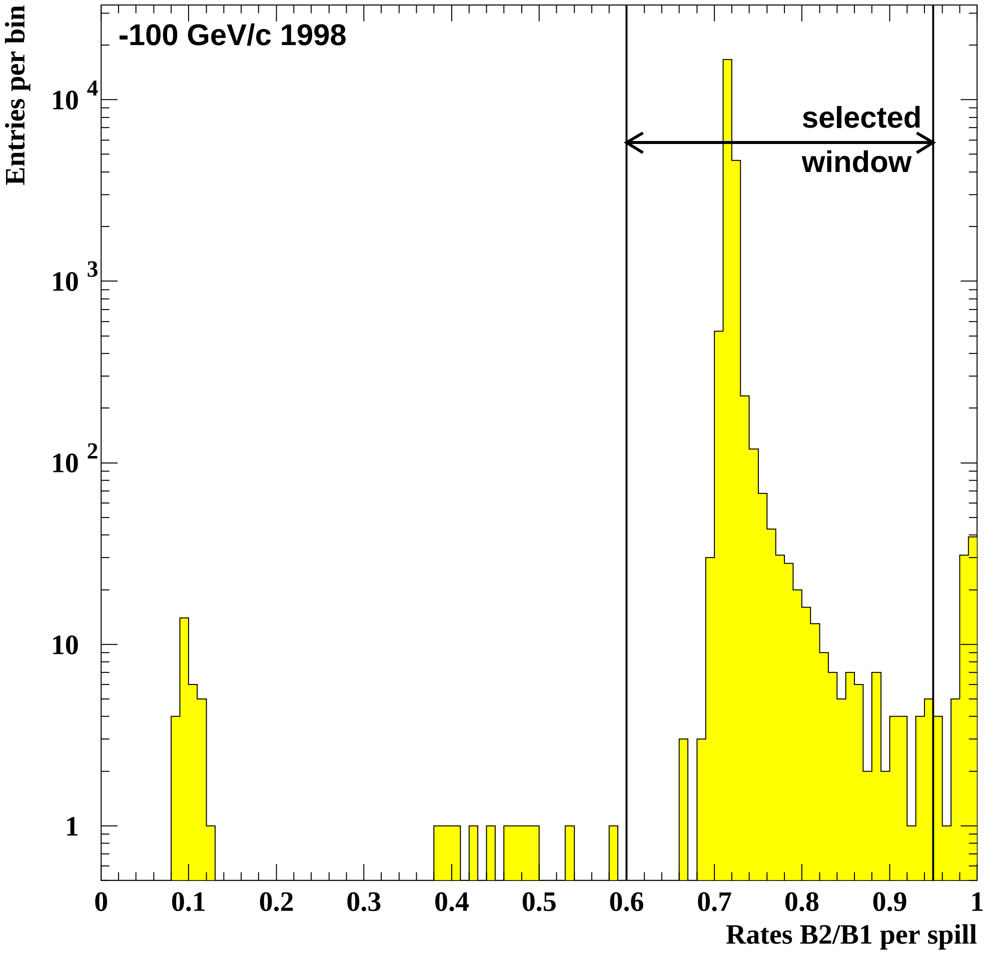

Figure 4.1: Distribution of the transmissions from B1 to B2 for all the spills in the -100 GeV/c setting in 1998. This distribution was used to define the window of accepted spills. All the spills with entries outside this window were afterward tagged as 'bad'.

The reason is TOF0 with the highest rates and the largest distance from the trigger counter implying the largest lever in the TOF fit. For each event TOF0 contains multiple lead ion entries. To select the lead ion which produced the particle identified in the beam line, the fit is done first without TOF0. The entry nearest to the fit extrapolation to TOF0 is then added to the fit. However, an additional lead ion within the double pulse resolution of 7 ns just before the correct one can fake a significant high mass to charge ratio. To avoid such events, TOF0 is added only if the nearest entry lies within three standard deviations of its time resolution which is 250 ps. The rejection of pile-up by looking at the

pulse height was limited in 1998 because of the radiation damages to TOF0 from the previous runs (see appendix B.2).
The particle identification by the mass to charge ratio is further supported by means of threshold Čerenkov counters (see appendix B.1).

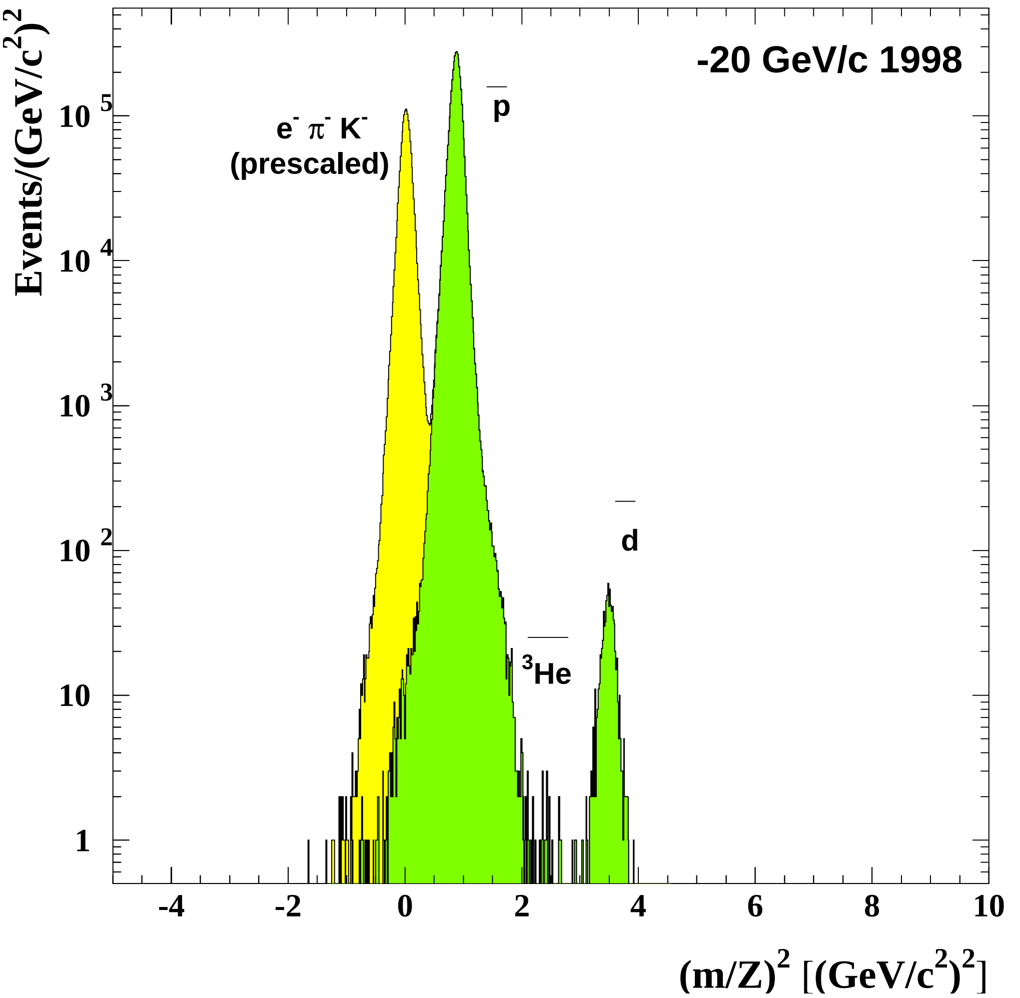

Figure 4.2: Time of flight spectrum obtained at a spectrometer rigidity of -20 GeV/c in the 1998 run. The particle identification capability of the TOF and Čerenkov counters is shown. The light particles (e, π^-, K^-) are pre scaled.

A time of flight spectrum obtained during the -20 GeV/c setting in 1998 is shown in figure 4.2. Figure 4.2 demonstrates the particle identification capabilities of the TOF and the Čerenkov counters. Anti deuterons are significantly separated from anti protons. Also lighter particles (e, π^-, K^-) are separated from the anti

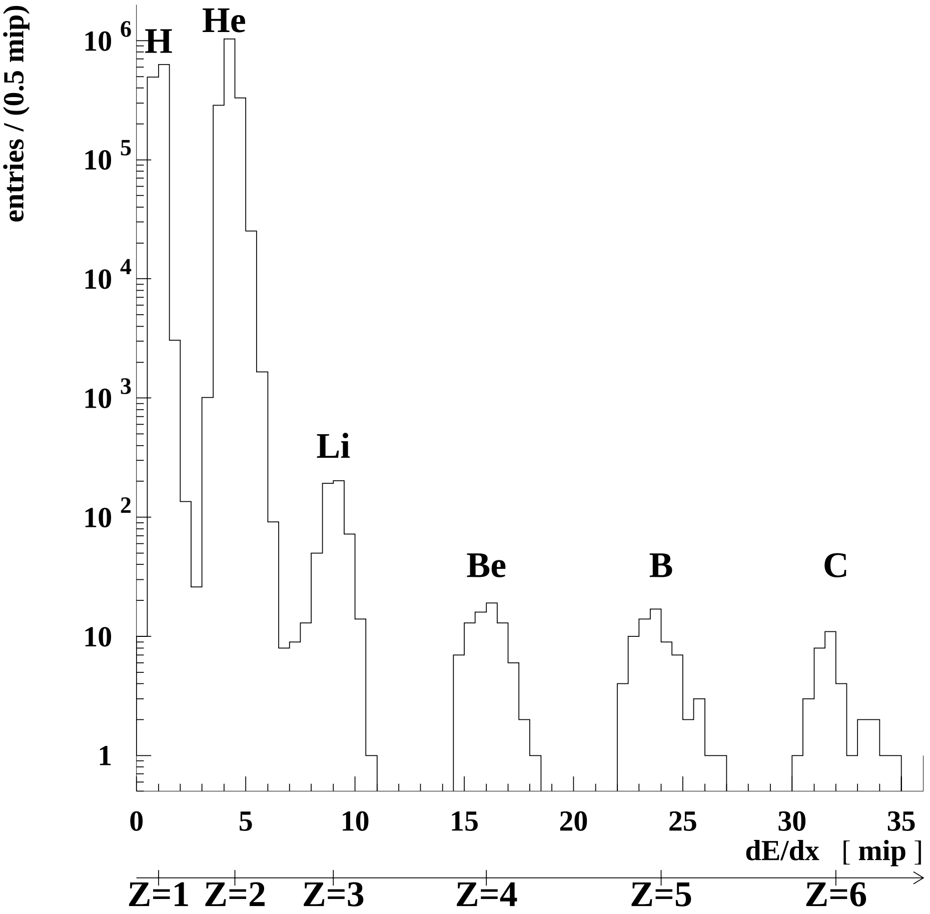

Figure 4.3: Charge distribution from the data taking in 1996. The distribution shows the relative abundance of fragments of the incident lead ion identified by their charge. The dynamic range is proven to go up to charge Z=6.

protons by time of flight and by a threshold Čerenkov counter, as shown with different gray scales.

4.3 Reconstruction of the charge

The charge is derived from measured pulse height (energy loss $\mathrm{d}E/\mathrm{d}x$) in the scintillators. Redundancy is added by the Čerenkov counters and the hadronic calorimeter (see section 2.4). Since the energy deposition in the detectors depends quadratically on the charge, higher charged objects give a clear signal. Although the Landau distribution has a significant tail to higher charges for a single counter, combining many detectors allows to nicely separate different charges, as can be seen in figure 4.3.

The reconstruction of the square charge from the information of all the pulse heights is done by calculating the mean energy loss. Some special precautions have been taken to eliminate events with the pulse heights of the different detectors too much spread (cluster method by P.Hess [46]). In some cases single pulse heights have been discarded if clearly deviating from a series of matching measurements.
It has to be mentioned that the strangelet search bases only on time of flight distributions and does not depend on the charge measurement. Nevertheless, for measured strangelets the charge would be important to know.

4.4 Counting the incident lead ions

The incident lead ions are counted by the quartz detector in front of the target TOF0 (see appendix B.2). The number of incident lead ions is determined by counting spill-wise all the discriminator firings from all the 16 de-multiplexed channels. This section refers to the 1998 data. Details on the lead ion counting for the 1994 and 1995 data can be found in [41, 44]. A critical issue of the incident lead ion counting is to take pile up into account. In 1998 the ion rates delivered by SPS to the NA52 target reached in certain cases 10^8 ions per second. At this rate the probability of having a second ion within the 7 ns resolution of TOF0 is 12%. Due to this the real number of lead ions is larger than the counted one. To correct for this discrepancy the idea is to recount once the entries with possibly at least 2 lead ions, count once again the ones with at least 3 entries and so on. A correction factor to the lead ions counted by the scalers is given by:

$$k = 1 + A_2 + A_3 + A_4$$

with A_n the probability to have at least n entries in the double pulse resolution d (7 ns from appendix B.2). In the analysis, factors of up to $n = 4$ have been taken into account, which guarantees for 1998 rates less than 1% systematic error on $k - 1$. The A_n are calculated by:

$$A_n = 1 - \sum_{N=0}^{n} P_N$$

with P_N the probability to have exactly N lead ions within d at a rate R which is given by a Poisson distribution:

$$P_N = \frac{1}{1 - e^{-d \cdot R}} \frac{(d \cdot R)^N}{N!} \cdot e^{-d \cdot R} \qquad (N = 1, 2, 3, ...)$$

This distribution does not contain P_0, since we trigger on an incident lead ion in the given d time window and so have at least the triggering one. So the native Poisson has to be scaled by $1/(1 - P_0) = 1/(1 - \exp(-d \cdot R))$ for normalisation.

The correction factors k are determined within this model only by the ion rates. The rates are calculated spill-wise by using the mean number of entries in the 2.5μs time window covered by the future past mechanism (see appendix B.2). Since the beam is not always centered relative to TOF0, each quadrant sees its own rate and therefore has its own correction factor. The correction factors are determined for a whole spill, since the rates on each quadrant do not change in time during a spill except for the first and last few percent of it due to the extraction. A typical correction during the -70 GeV/c setting was 4% (k = 1.04) with a distribution shown in figure 4.4.

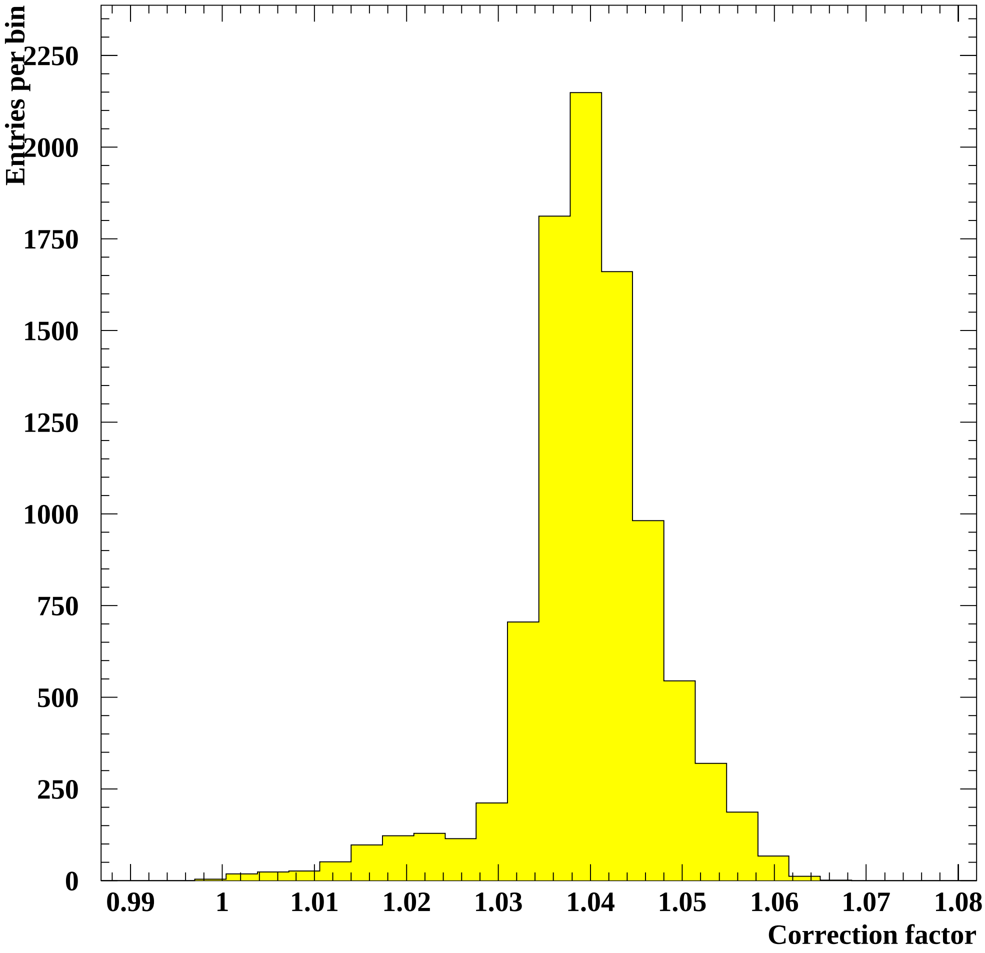

Figure 4.4: Distribution of correction factors for the lead ion counting per spill for one quadrant of TOF0 during the -70 GeV/c rigidity setting.

4.5 Invariant differential production cross sections

The invariant differential production cross section can be written as:

$$E\frac{d^3\sigma}{dp^3} = E \cdot \frac{1}{p^3 \cdot \alpha} \cdot \frac{N_s}{N_{Pb}} \cdot \frac{1}{d} \cdot \frac{1}{A_v}. \tag{4.1}$$

where

E and p	are the energy and momentum of the secondaries,
α	is the relative spectrometer acceptance,
N_s	is the number of secondaries,
N_{Pb}	is the number of Pb+Pb interactions,
d	is the target thickness and
$A_v = 0.033\frac{1}{\text{barn cm}}$	is the volume density of the target.

The above equation does however not take into account any effects due to the target thickness. If a target thickness scan is available absorption of the incident beam and the secondaries and reinteraction can be taken into account. This is the case for some particle cross sections presented in section 6.1, where also the used model is described.

If no target thickness scan is available we can nevertheless take into account that the incident beam has not the full intensity at all target depth. Instead of taking $d \cdot A_v$ as area density A_d, we consider the target as made of thin slices and integrate the local beam intensity times the volume density A_v over the target thickness d:

$$\begin{aligned} N_{Pb} \cdot A_d &= \int_0^d N_{Pb} \cdot e^{-x/\lambda_{Pb}} \cdot A_v \cdot \mathrm{d}x \\ &= N_{Pb} \cdot (1 - e^{-x/\lambda_{Pb}}) \cdot \lambda_{Pb} \cdot A_v \\ &= N_{int} \cdot \lambda_{Pb} \cdot A_v. \end{aligned}$$

with $\lambda_{Pb} = 37$mm the total interaction length for Pb in Pb (extrapolated from [47]). Note that $N_{Pb} \cdot (1 - \exp(-x/\lambda_{Pb}))$ is the number of interactions N_{int}.

Taking also the reconstruction efficiency ϵ into account the resulting formula for the invariant differential cross section is:

$$E\frac{d^3\sigma}{dp^3} = E \cdot \frac{1}{p^3 \cdot \alpha} \cdot \frac{N_m/\epsilon}{N_{int}} \frac{1}{\lambda_{Pb}} \cdot \frac{1}{A_v} \tag{4.2}$$

with N_m the number of measured secondaries.

4.6 Event displays

To have a closer look on some single events of interest we display all the information of the event in what we call event displays. Event displays show graphically the reconstructed data and the complete information stored in the raw data. An example of the graphical display of reconstructed data can be seen in figure 4.5. From this an impression about the quality of the TOF fit, the charge determination and the length of the track can be retrieved. Shown is essentially the time delay to a pion ($\beta \approx 1$) for each time of flight counter. The slope of the points is related to the mass as described in section 4.2. The reconstructed mass is also given numerically together with the charge.
A lot of supplementary information is shown which is not treated here in detail. The event in figure 4.5 could be identified to be an $\overline{^3\text{He}}$.

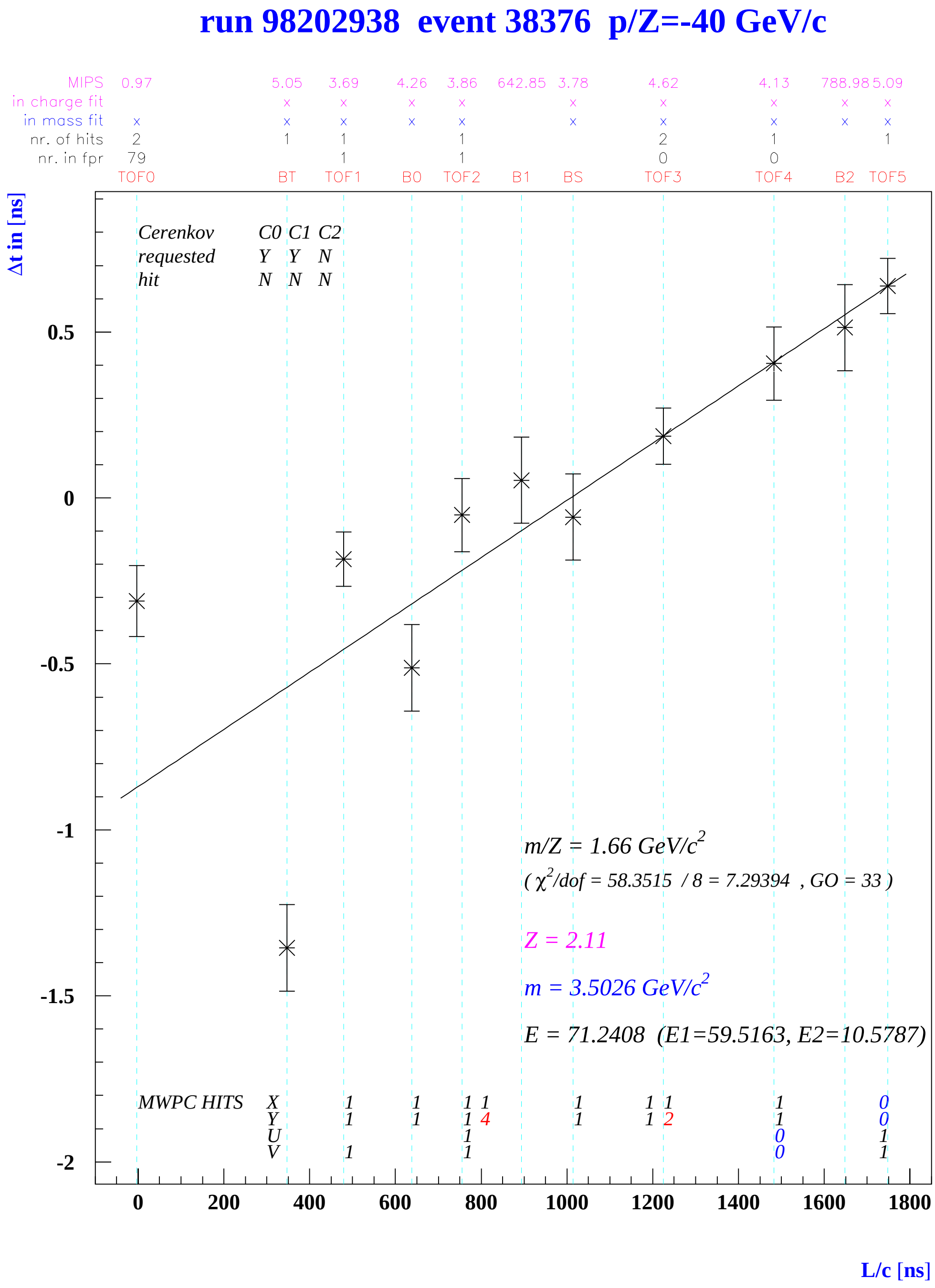

Figure 4.5: An event display showing graphically the reconstructed event data. It allows to get an impression about the quality of the TOF fit, the charge determination and the length of the track. The event in this figure could be identified to be an $^3\overline{\text{He}}$.

Chapter 5

The NA52 strangelet search

In this chapter the NA52 strangelet searches from the 1998 data are described. The final results from NA52 are presented including the results from previously analysed data [41] in section 5.1. It can be mentioned already here that no strangelets have been found. Not having found them does not mean that they do not exist. Nevertheless, the discussion presented is an attempt to give an idea of the extent of the performed searches in terms of differential cross sections and total sensitivities. Also shown are production limits for strangelets with shorter lifetimes than already analysed and published by NA52 [48, 49, 50, 51, 52].

5.1 Results

The search for strangelets is straightforward: the high mass to charge ratio is an evident signature for the analysis. Nevertheless, one of the main issues in searching for strangelets were the cuts to apply to the reconstructed data. The cuts include a reasonable fit ($\chi^2/ndf < 10$), the exclusion of multi particles in the beam line, a plausible TOF0 entry and that the track had to reach TOF3. The definition of the cuts is made weighting the mass resolution with the reconstruction efficiency. The efficiency is studied for known particles under the assumption that strangelets behave the same way. For each setting the reconstruction efficiencies are listed in table 5.1 together with the acceptances and the number of Pb+Pb interactions.

As an example for a resulting time of flight spectrum, the -70 GeV/c one is shown in figure 5.1. The entries in this distribution are 1601 $\overline{\mathrm{d}}$. There is one candidate with a mass to charge ratio $(m/Z)^2 = 26.4$ (GeV/c^2)^2 ($|m/Z| = 5.14$ GeV/c^2). This candidate had to be discarded after a closer look.

As at -70 GeV/c, in none of the mass distribution of the 1998 data taking a strangelet has shown up. A summary over all the analysed settings with all the time of flight distributions can be found in appendix C.

Rigidity [GeV/c]	Target thickness	Reconstruction efficiency	Acceptance [μsr%]	Pb+Pb interactions
-20	16 mm	0.76	3.14	$8.95 \cdot 10^{10}$
-20	4 mm	0.77	3.14	$4.20 \cdot 10^{10}$
-20	0 mm	0.77	3.14	$4.03 \cdot 10^{10}$
-20	8 mm	0.77	3.14	$8.95 \cdot 10^{10}$
-20	40 mm	0.77	3.14	$8.52 \cdot 10^{11}$
-40	40 mm	0.79	3.60	$3.07 \cdot 10^{11}$
-40	40 mm	0.74	3.60	$9.58 \cdot 10^{11}$
-40	0 mm	0.73	3.60	$4.39 \cdot 10^{10}$
-40	8 mm	0.74	3.60	$2.02 \cdot 10^{10}$
-40	16 mm	0.72	3.60	$4.85 \cdot 10^{10}$
-70	40 mm	0.79	3.74	$1.14 \cdot 10^{12}$
-100	40 mm	0.79	3.78	$2.20 \cdot 10^{12}$
-200	40 mm	0.80	3.80	$7.53 \cdot 10^{11}$
-200	40 mm	0.76	3.80	$8.26 \cdot 10^{10}$

Table 5.1: Reconstruction efficiency, acceptance for particles reaching TOF3. Also shown is the number of interactions for each setting. The reconstruction efficiency is determined for known particles. We assume that strangelets behave the same way and therefore have the same reconstruction efficiency.

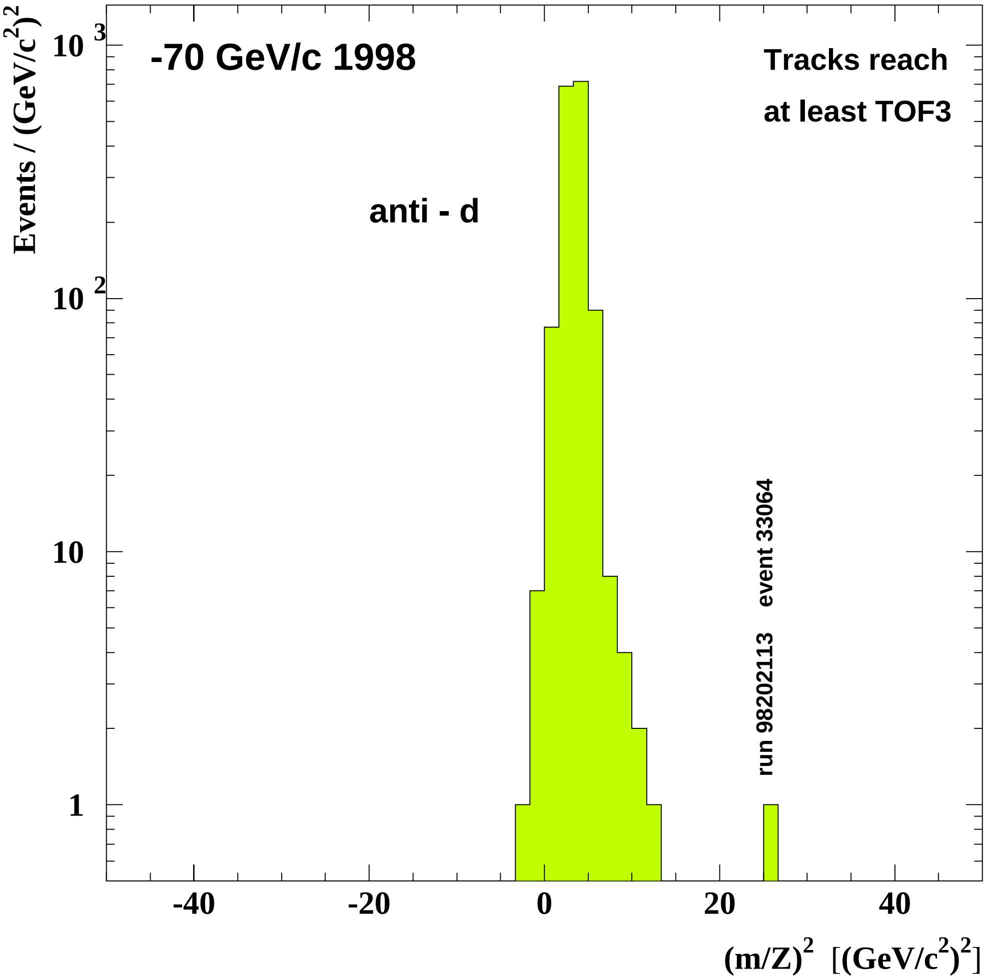

Figure 5.1: Time of flight distribution from the -70 GeV/c setting in 1998. There is one "candidate" with a mass to charge ratio $(m/Z)^2 = 25$. This candidate had to be discarded because the TOF0 time entry was faked by lead ion impinging just before the one that produced the particle in the beam line.

5.2 Upper invariant differential strangelet production cross sections

As no strangelet has been found, we quote upper invariant differential production cross sections which are calculated according to equation 4.2. We choose $N_m = 2.3$, which is the upper number of strangelets there could have been with 90% confidence level. The measurements have been done at p_t=0 and at a rapidity given by the selected spectrometer rigidity and the assumed mass.
The resulting exclusion plot for different rapidities as a function of the assumed strangelet mass is shown in figure 5.2.

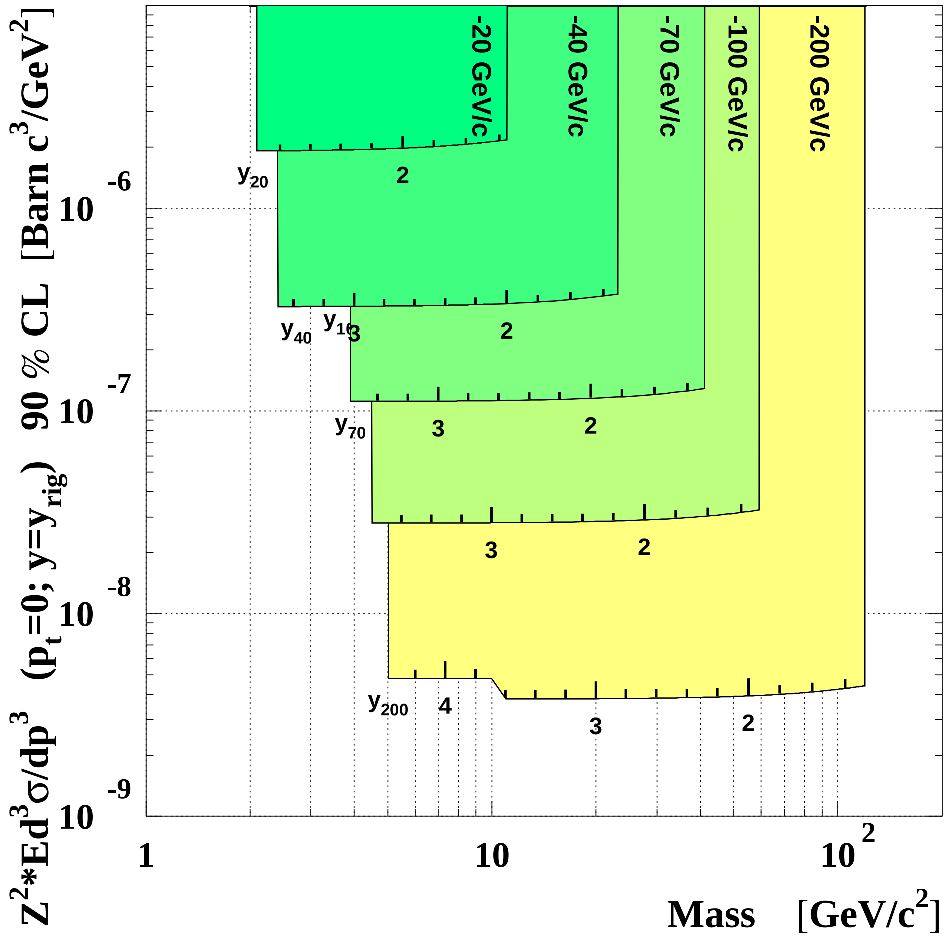

Figure 5.2: Exclusion plot for strangelets according to upper invariant differential production cross sections. These are measured at p_t=0 and at a rapidity given by the selected spectrometer rigidity and the assumed mass. The rapidity is indicated at the bottom of each region.

The rapidity is indicated at the bottom of each region. The limits include the full statistics of 1994, 1995 and 1998. They cannot be added up, since for a given mass different rigidities mean different rapidities. The systematic error is estimated to be 25% from the uncertainty of the acceptance and the counting of the incident lead ions.

5.3 Total strangelet production limits

The total strangelet production limits are given in terms of upper yields (maximal number of strangelets produced per collision). These upper yields can also be interpreted as sensitivity. NA52 probes a small region of the phase space for each setting. In order to quote total upper yields we have to know which portion of the strangelets we see, i.e. which fraction of the strangelets fall into the phase space covered by our acceptance. This is needed in order to extrapolate the measured yields to the full phase space. Since the phase space distribution of the strangelet production is not known, we have to assume one. We use a distribution which is Gaussian in rapidity y and exponential in transverse momentum p_t [53, 54, 27]:

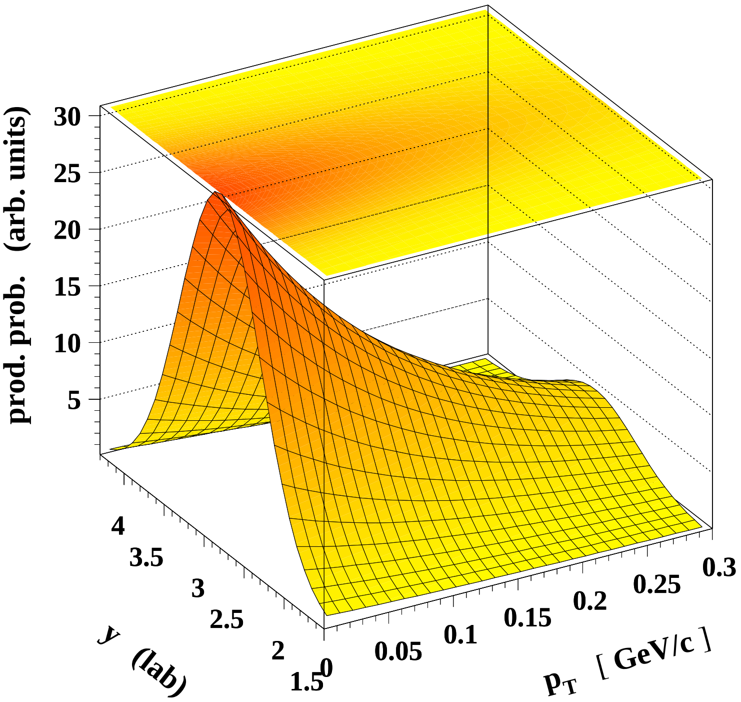

Figure 5.3: Assumed phase space distribution of the production of strangelets.We use a distribution which is Gaussian in rapidity y with $\sigma_y = 0.5$ and exponential in transverse momentum p_t with $\langle p_t \rangle = 0.1\sqrt{m\ (\mathrm{GeV})}$ [53, 54, 27].

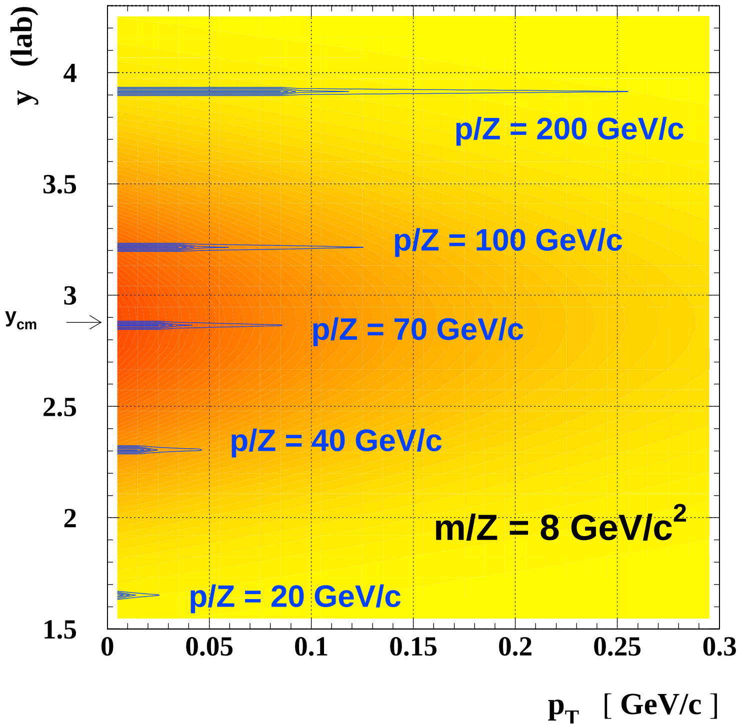

Figure 5.4: The acceptance of the H6 beam line used by NA52 is superimposed on the production model. The darker region is the one of higher production probability. One can also see how small the acceptance of NA52 is.

$$\frac{d^2N}{dy\,dp_t} = \frac{1}{\sqrt{2\pi}\sigma_y} \exp\left(\frac{(y-y_{cm})^2}{2\sigma_y^2}\right) \cdot \frac{4p_t}{\langle p_t\rangle^2} \exp\left(-\frac{2p_t}{\langle p_t\rangle}\right) \tag{5.1}$$

A plot of such a phase space distribution as a function of y and p_t is given in figure 5.3.

The integral of $\frac{d^2N}{dy\,dp_t}$ over the spectrometer acceptance gives the fraction of seen strangelets P (the production model as written in equation 5.1 is normalised).

$$P = \int_0^{\alpha} \frac{d^2N}{dy\,dp_t} \cdot dy \cdot dp_t$$

The acceptance of the H6 beam line at CERN SPS used by NA52 is superimposed on the production model in figure 5.4. The darker region is the one of higher production probability. In this figure one can also see how small the acceptance of NA52 is within the phase space.

The sensitivities as a function of the assumed strangelet mass are then calculated according to:

$$S(m) = \frac{2.3}{N_{int}} \cdot \frac{1}{P} \cdot \frac{1}{\alpha \cdot \epsilon}$$

where N_{int} is the number Pb+Pb interactions, ϵ the detection efficiency and P the fraction of seen strangelets.
Since no strangelets have been observed the 2.3 stands for the upper number of strangelets there could have been with 90% confidence level. The obtained sensitivities are plotted versus the assumed mass to charge ratio of a strangelet (see curves in figure 5.5). In contrast to differential cross sections, sensitivities (total yields) can be added up. The determination of the overall sensitivity is done according to:

$$\frac{1}{S_{\text{tot}}} = \frac{1}{S_1} + \frac{1}{S_2} + \frac{1}{S_3} + \ldots$$

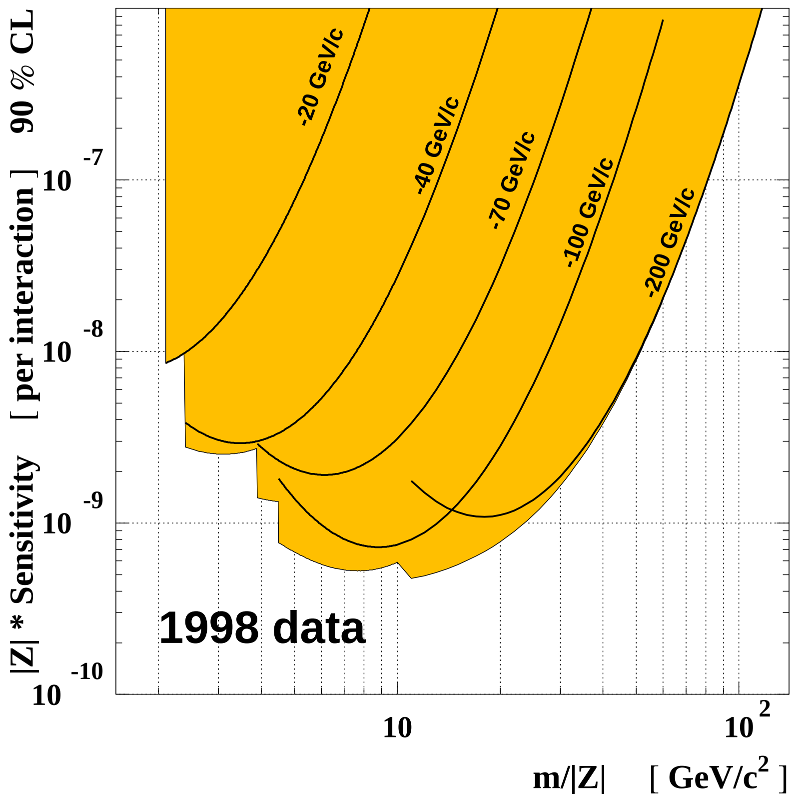

Figure 5.5: Each curve represents the total sensitivity of one setting. The total sensitivities are add up to the shaded exclusion region.

An example of overall sensitivity and its component sensitivities for different rigidities is shown in figure 5.5.

The sensitivity depends not only on experimental quantities (like the number of lead ions) but also on two model assumptions. These are the width of the rapidity distribution and the mean transverse momentum $\langle p_t \rangle$ of the strangelet production phase space distribution. Since no strangelet distribution could be measured one has to make assumptions. The mean transverse momentum has an effect on the vertical position of the sensitivity curve. It is chosen to be $\langle p_t \rangle = a\sqrt{m}$ (GeV) with $a = 0.1$. The parameter a and therefore p_t is expected to be small, under the assumption that strangelets are remnants of a cooling quark-gluon plasma produced at rest. The width of the rapidity distribution is chosen to be $\sigma_y = 0.5$. This parameter has an effect on the width of the sensitivity curve. If the rapidity width of the production is assumed to be narrow, our sensitivity gets drastically worse if we are a bit away from the maximum production probability. A very broad production distribution would make the sensitivity curve in figure 5.5 flat.

5.3.1 Tracks reaching at least TOF3

In a first step we consider strangelets with $\tau > 1.2\mu$s and do not take into account decays in flight. The tracks have to reach at least TOF3 (see figure 2.1) at $L/c = 1.2\mu$s behind the target. The resulting total sensitivities are shown in figure 5.6 as a function of the assumed mass to charge ratio for negatively charged strangelets. It should be mentioned that we do not apply cuts on the centrality of the Pb+Pb collisions, and so the sensitivity is given in units of minimum bias collisions. For the negative charge the sensitivities from the data taken in 1994 and 1995 [41] and from the data taken in 1998 are plotted separately. Also plotted is the overall sensitivity to negatively charged strangelets combining all the data taken by NA52. For a comparison of the sensitivity with theoretical predictions and other data see section 5.4.

Taking into account also decays in flight, figure 5.7 shows how the sensitivity decreases as a function of the assumed lifetime τ for three sample masses. Due to the γ-factor the best sensitivities for the strangelets with very short lifetimes are reached for the lightest ones.

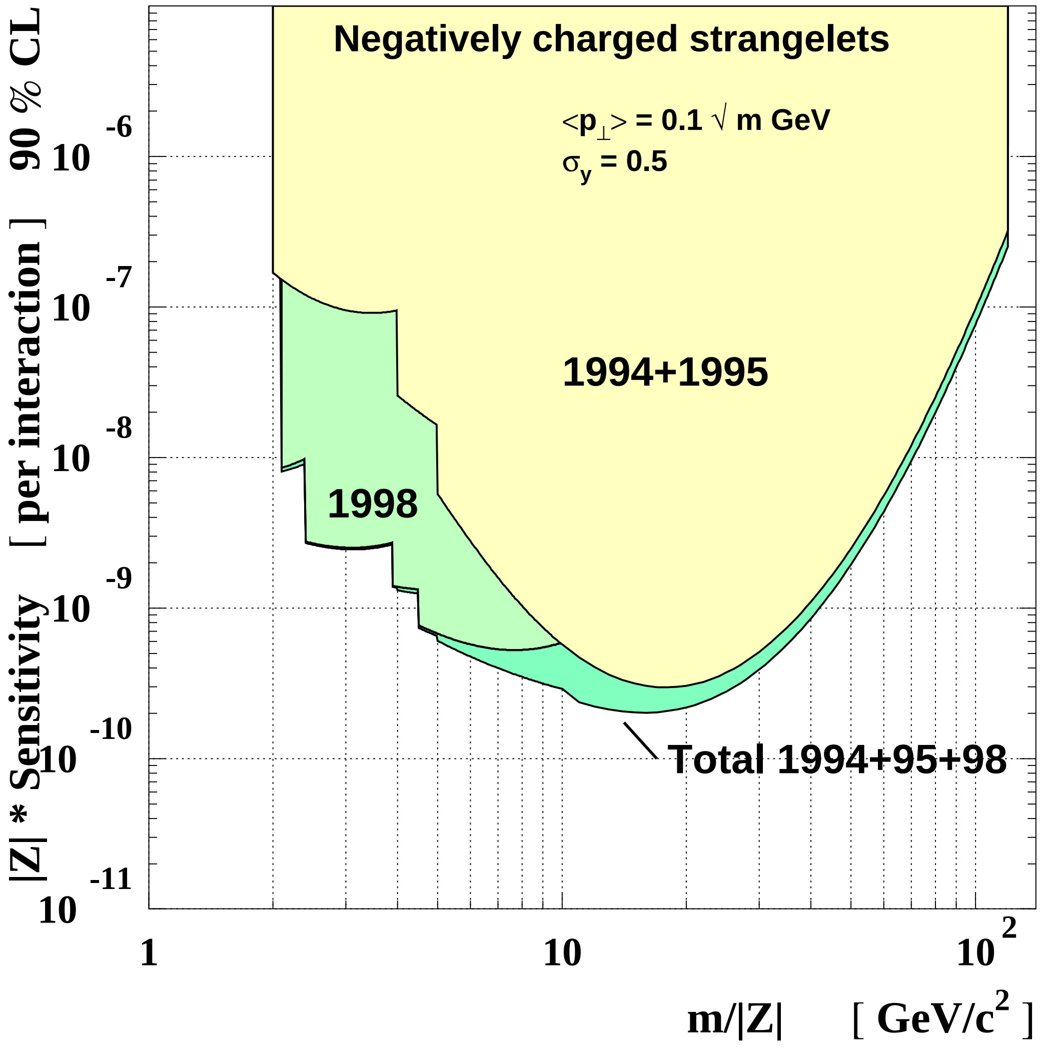

Figure 5.6: NA52 exclusion plot for the production of long lived charged strangelets. The sensitivity reached per minimum bias collision is plotted versus the assumed mass to charge ratio for negatively charged strangelets. The sensitivity reached in the different data taking periods 1994+1995 and 1998 are shown. Also plotted is the overall sensitivity to negatively charged strangelets combining all the data taken by NA52. For a comparison of the sensitivity with theoretical predictions and other data see section 5.4.

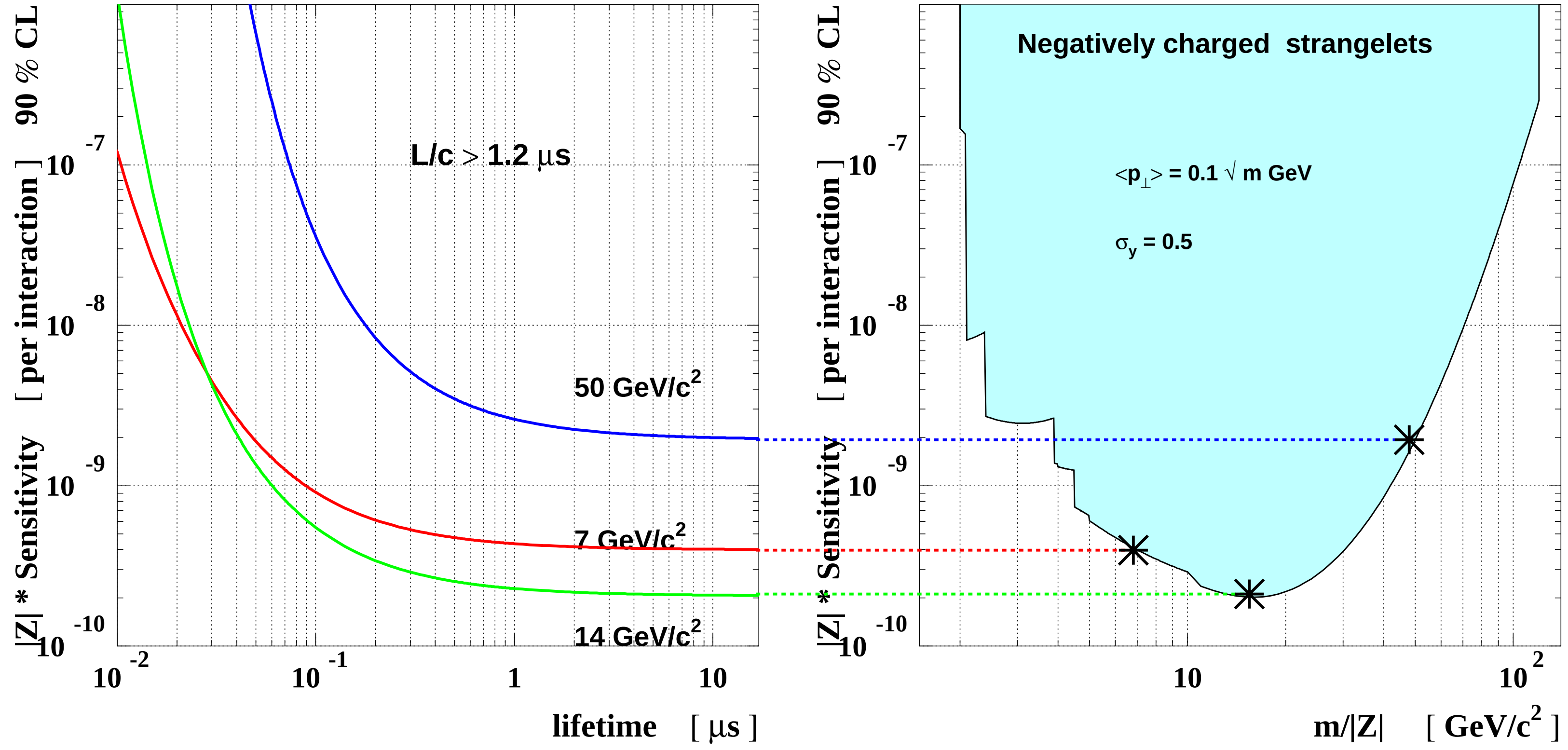

Figure 5.7: On the right side the NA52 sensitivity for negatively charged long lived strangelets as a function of the mass to charge ratio. On the left side the sensitivity is plotted as a function of the assumed lifetime for three sample $m/|Z|$ of 7, 14 and 50 GeV/c^2. The tracks had to reach TOF3 at $L/c = 1.2\mu$s behind the target.

5.3.2 Short tracks (reaching at least B1)

To address the strangelets with shorter lifetimes τ, we also looked at shorter tracks. The shortest tracks recorded reach at least B1 at 0.9μs behind the target,

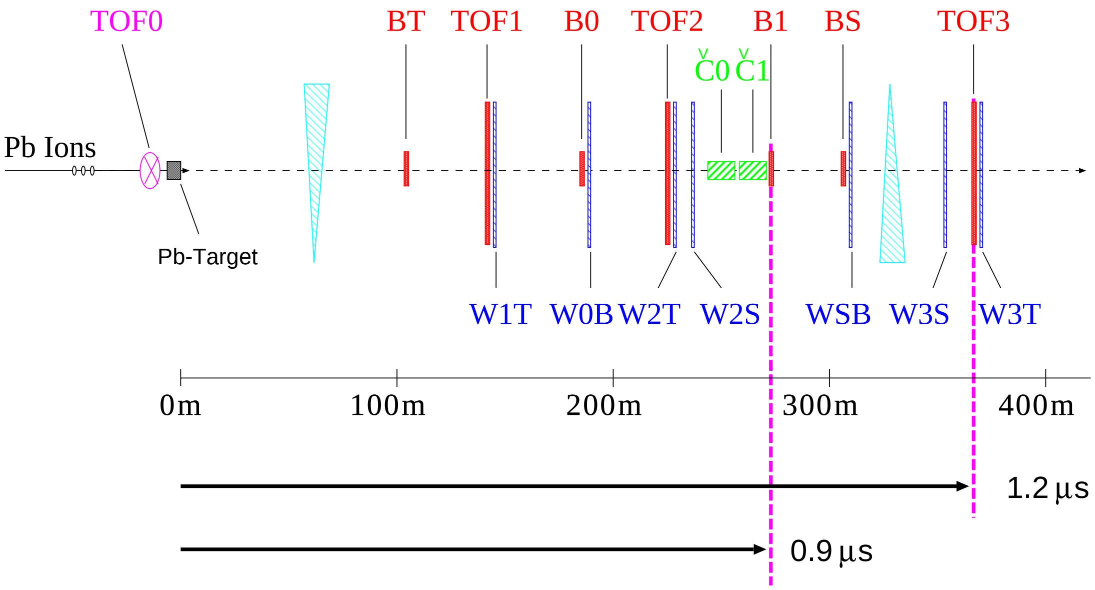

Figure 5.8: Experimental setup in the upstream part of NA52. In a first step of the analysis particles reaching at least TOF3 are taken into account. To address the strangelets with shorter lifetimes τ, we also looked at shorter tracks reaching B1.

which is our trigger counter (see figure 5.8). In 1998 we were able to reconstruct the shorter tracks, since we increased the redundancy of the TOF and track measurements adding the new counters BT, B0. However, the main problem with shorter tracks is due to a large background of particles with small $m/|Z|$. In figure 5.9 the mass distributions for 3 different track length requirements, i.e. B1, BS and TOF3 are shown.

With the chosen Čerenkov counter settings the distribution should peak at $(m/Z)^2 = 3.5\ (\mathrm{GeV}/c^2)^2$ (anti deuterons). This is not the case for the short tracks, therefore these distributions are considered as background and are understood as inefficiency of the Čerenkov counters. In figure 5.10 the beam profile at the wire chamber W2T is shown for the short tracks which give no light in the Čerenkov counters compared to long tracks giving light. A clear concentration of the background tracks at the edge of the beam profile can be identified. However, attempts to select "good" short tracks cutting on the position as suggested from figure 5.10 did not sufficiently eliminate the background.

The short tracks are nevertheless useful for strangelets searches. The background only raises the lower mass limit we can quote and in fact does not affect the

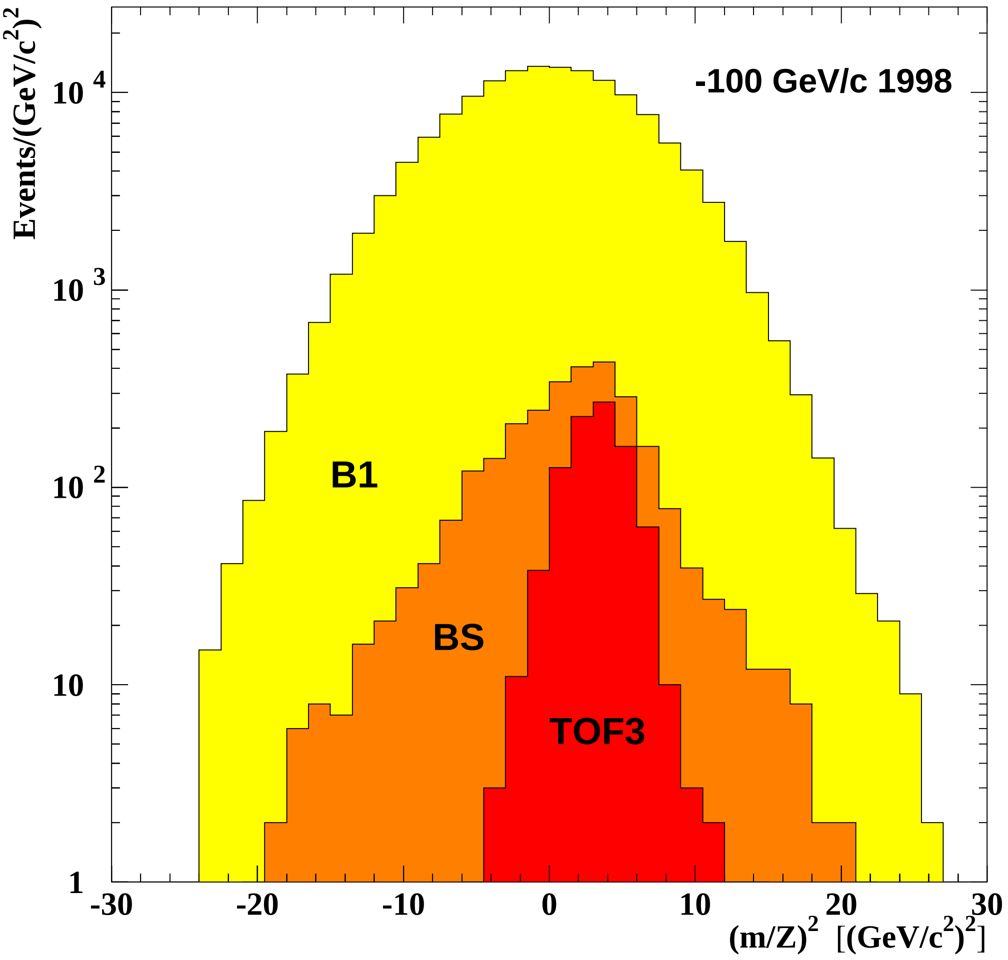

Figure 5.9: Example of the track length dependence on the mass distribution. Three different track length requirements, i.e. B1, BS and TOF3 are shown. With the chosen Čerenkov counter settings the distribution should peak at $(m/Z)^2 = 3.5$ (GeV/c^2)^2 (anti deuterons). This is not the case for the short tracks, therefore these distributions are considered as background and are understood as inefficiency of the Čerenkov counters. The consequence are higher mass limits for exclusion of strangelets.

strangelet measurement for higher $m/|Z|$. The mass limits given by the background are shown in table 5.2.

Finally, however, no strangelet has been observed even in the shorter tracks. The gain in sensitivity taking also shorter tracks into account depends on the assumed lifetime as shown in figure 5.11 left. In this plot an example of strangelets with $m/|Z| = 14$ GeV/c^2 has been selected. A factor of 1.6 is gained in sensitivity if

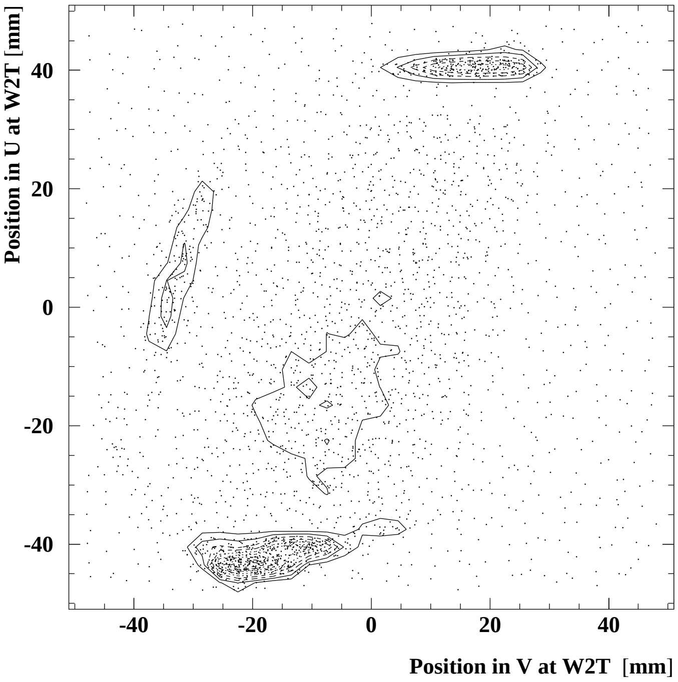

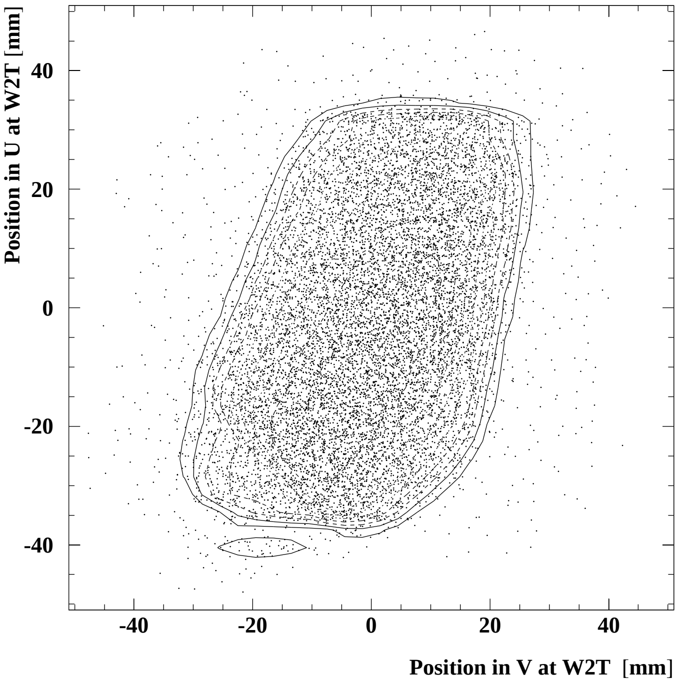

Figure 5.10: Beam profiles at the wire chamber W2T. On the left for the short tracks which give no light in the Čerenkov counters and on the right for long tracks giving light. A clear location of the former tracks considered as background at the border of the beam profile can be identified.

Rigidity [GeV/c]	Minimal track length	Lower mass limit [GeV/c^2]
-20	TOF3	2.1
-20	B1	2.2
-40	TOF3	2.4
-40	B1	3.2
-70	TOF3	3.9
-70	B1	5.5
-100	TOF3	4.5
-100	B1	7.4
-200	TOF3	10.7
-200	B1	13.4

Table 5.2: Lower mass limits for the strangelet searches.

one assumes a lifetime of $\tau = 50$ ns. Figure 5.11 right shows the sensitivity for tracks with $L/c > 0.9\mu$s as a function of the mass to charge ratio for a lifetime $\tau = 50$ ns. The dark region is the contribution from the short tracks. As a result we can quote an upper production limit per Pb+Pb collision of $7 \cdot 10^{-10}$ strangelets with assumed lifetime $\tau = 50$ ns, mass $m = 14$ GeV/c^2 and charge $Z = -1$.

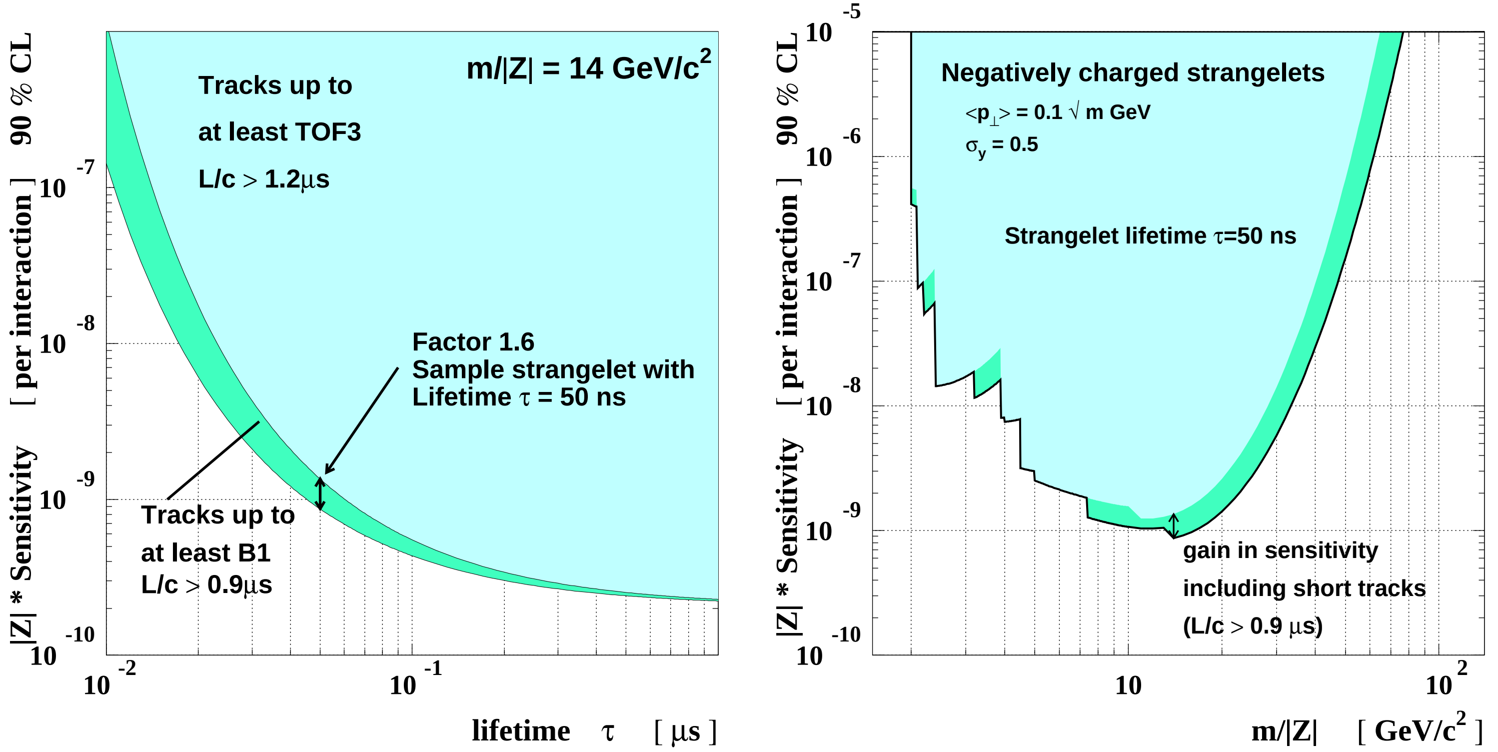

Figure 5.11: Gain in sensitivity including short tracks ($L/c > 0.9\mu$s). Top: as a function of the assumed lifetime τ for a strangelet with $m/|Z| = 14$ GeV/c. The gain is indicated by the darker region (e.g. a factor 1.6 for $\tau = 50$ ns). Bottom: the sensitivity is plotted as a function of the mass to charge ratio for a lifetime of $\tau = 50$ ns. We still have a sensitivity of 10^{-9} per interaction for shorter-lived strangelets.

5.4 Discussion

Motivated by the quest for a new form of matter in dense astrophysical objects a series of heavy ion experiments has been performed to search for strangelets. NA52 looked at Pb+Pb collisions at 158 GeV/c with a small acceptance focussing spectrometer. No strangelets have been observed and upper limits in terms of total cross sections have been presented. This search is complementary to searches with large acceptance spectrometers at lower momenta (11 A GeV/c) accomplished at the BNL-AGS (E858 [55, 31], E878 [33], E886 [32], E864 [56], E814 [30, 57]).

A comparison of the sensitivities reached by several experiments for long-lived strangelets with $Z = -1$ is given in figure 5.12. Also shown are limits achieved by NA52 in S-W collisions [58]. To allow for the comparison with minimal systematic uncertainty the curves are scaled to a specific parameter selection for the phase space distribution (5.1) with $\sigma_y = 0.5$ and $\langle p_t \rangle = 0.5 \ldots 0.7\sqrt{m}$ GeV).

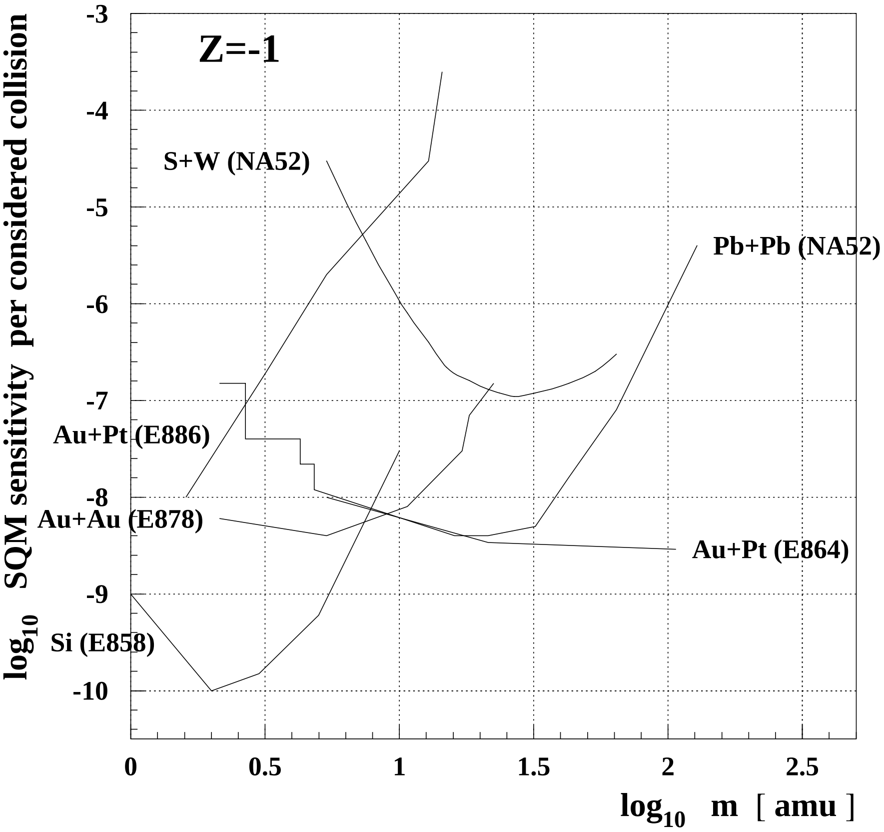

Figure 5.12: Compilation of achieved sensitivities by several experiments for long-lived strangelets with $Z = -1$.

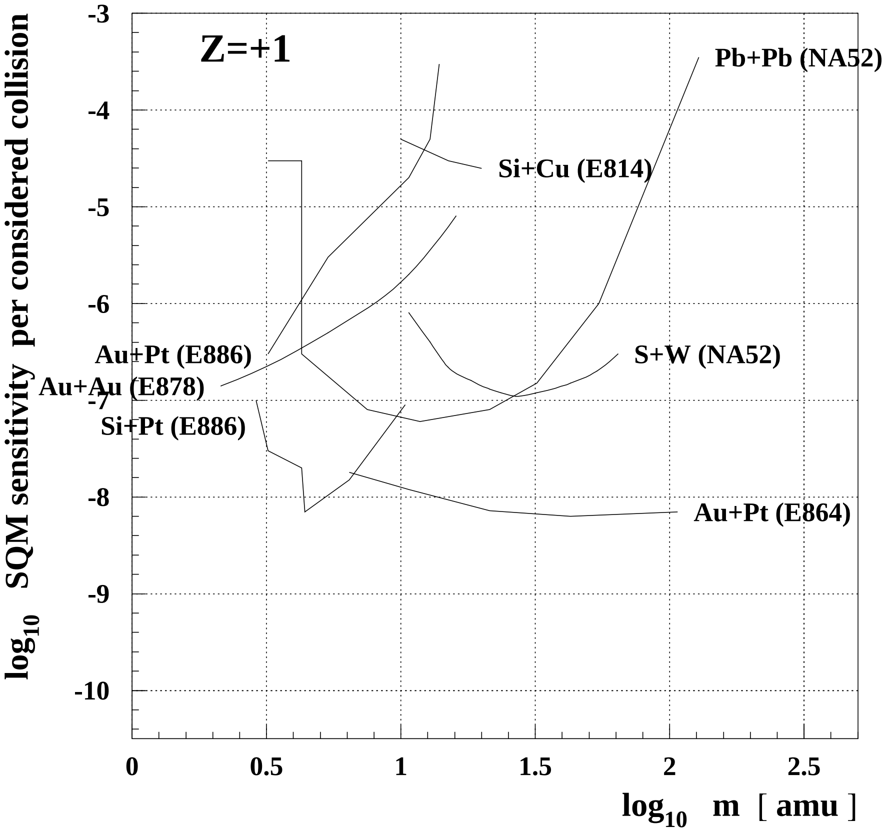

Figure 5.13: Compilation of achieved sensitivities by several experiments for long-lived strangelets with $Z = +1$.

Nevertheless, it should be noted that direct comparison of achieved sensitivities is difficult. On the one hand different colliding systems such as Si+Cu, Si+Pt, S+W, Au+Au, Au+Pt and Pb+Pb at different energies have been investigated, on the other hand different selections of the centrality of the interactions are made (minimum bias for E814, E878, E886, NA52 and 10% most central for E864). A compilation of limits for strangelets with $Z = +1$ is given in figure 5.13 including yet published NA52 data from Pb+Pb [49] and S-W [58] collisions.

These results allow also a comparison to theoretical predictions. Several production models have been proposed for positively charged strangelets. One of them is production through coalescence [27]. Baryons are combined to form hyper nuclei (or strange clusters) which can decay into strangelets and so act as a doorway for the SQM production. The idea is that the production probability is inverse proportional to baryon number and strangeness. The slopes of the dependency is obtained by combining measurements of nuclei and hyperon production. Pro-

duction probabilities of 10^{-2} (${}^{3}_{\Lambda}$He) to 10^{-6} (${}^{6}_{\Lambda\Lambda}$He) per minimum bias Au+Au collisions are obtained which are mainly ruled out by the experiments.
Another model is a thermodynamical model [59] calculating production probabilities by filling the phase space according to a Boltzmann distribution. The obtained production probabilities for hyper nuclei are similar to the ones from the coalescence model. Production probabilities for strange matter clusters are also calculated using a mass formula [60] to determine baryon number, charge and strangeness of the most stable objects. Such calculations give values from 10^{-12} (${}^{A}\mathrm{St}^{Z}_{S} = {}^{10}\mathrm{St}^{1}_{-8}$) to 10^{-27} (${}^{20}\mathrm{St}^{2}_{-16}$) per central Au+Au collision assuming a freeze out temperature of $T = 140$ MeV. These predictions for heavier objects are far out of reach of the experiments.

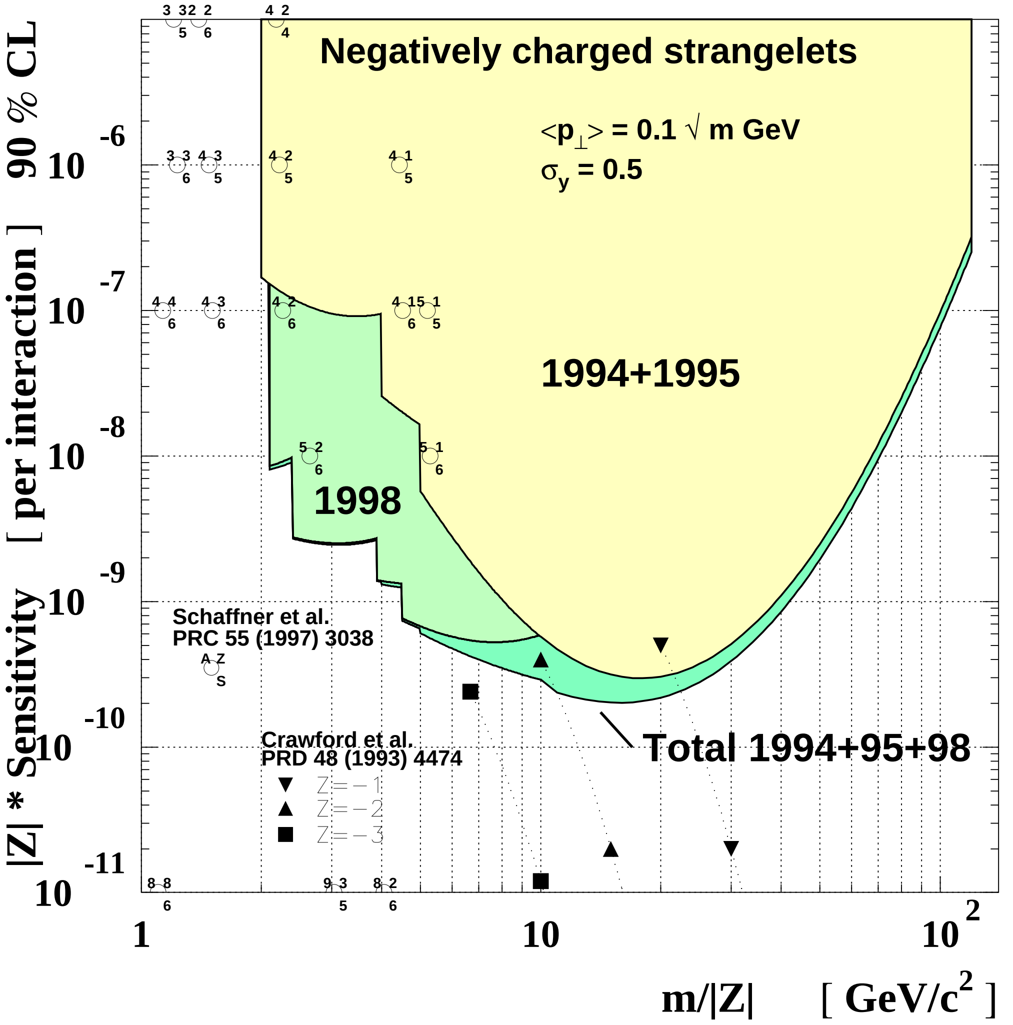

Figure 5.14: Comparison of the achieved sensitivity by NA52 and predictions by Crawford et al. [25] (filled symbols) and Schaffner-Bielich et al. [29] (open circles).

If nevertheless such objects would be found, this would give strong support to another production mechanism involving an intermediate quark gluon plasma (QGP) [28]. In this model strangelets are regarded as cool remnants of the QGP. Quantitative production probabilities for positively and negatively charged strangelets in Pb+Pb collisions were calculated by Crawford et al. [25]. A comparison of the results presented in this thesis and a selection of the highest production probabilities for negatively charged strangelets with lifetime $\tau > 10^{-7}$ sec is shown in figure 5.14 (filled symbols). As can be seen the reached sensitivity start to rule out also these predictions.

Later calculations [26, 29] favour the detection of light negatively charged strangelets (see figure 1.5 in the introduction). In contrast to the models mentioned above, here the emphasis has been put on decay schemes and stability of arbitrary quark compositions. Production probabilities of $10^{3-A-|S|}$ from a simple coalescence ansatz are proposed resulting in the predictions indicated in figure 5.14. Rather high production probabilities for the lighter strangelets are predicted which are ruled out. Heavier ones are out of reach.

The experimental techniques presented here and carried out so far have been restricted to the search for long-lived candidates. Correspondingly, achieved limits assume that the produced SQM is long-lived. However, the chances for the existence of short-lived metastable candidates are, at least theoretically, more probable. Therefore, a significant improvement in the detection of short-lived states would be desirable. This might be achieved by the searches for strong decaying low-mass states appearing as resonances.

Chapter 6

Results on particle searches

Besides the dedicated search for strangelets, NA52 measured light (anti)particle and (anti)nuclei production over a wide range of rapidity. Previous results have been performed in the framework of two PhD theses [44, 61] and published in [62, 49, 63, 64]. In this thesis results on particle production from the 1998 data are presented in terms of invariant differential production cross sections. In 1998 a scan of different target thicknesses was performed at rigidities of -20 GeV/c, -40 GeV/c, -70 GeV/c and -100 GeV/c. This allows in the analysis the use of a more sophisticated model than before to take target thickness into account which is presented here for the -20 and -40 GeV/c rigidities. Also $\overline{^3\text{He}}$ anti nuclei have been found. At -20 GeV/c one additional $\overline{^3\text{He}}$ to the one published in [64] and at -40 three $\overline{^3\text{He}}$ were identified. A compilation of the NA52 results on particle searches is given in section 6.3.

6.1 Target thickness scans

For the particle searches at -20, -40, -70 and -100 GeV/c in 1998 a target thickness scan is available. This allows to fully take the target thickness into account. In this section the model used and the particle cross sections derived from the -20 and -40 GeV/c data are presented.

6.1.1 $E\frac{d^3\sigma}{dp^3}$ target thickness dependency

The goal of the model is to describe how the true yield Y_S (see figure 6.1) can be determined taking absorption and reinteraction into account. In this subsection yields are used as the ratio of the number of secondaries per incident lead ions. The true yield $Y_S = N_s^x/N_{Pb}^x$ is used to calculate the cross sections with equation 4.1. The difficulty is that Y_S cannot be measured directly. The number of measured secondaries N_m in the beam line can be less than N_S^x because of absorption of the incident beam and the produced particles in the target. On the other hand

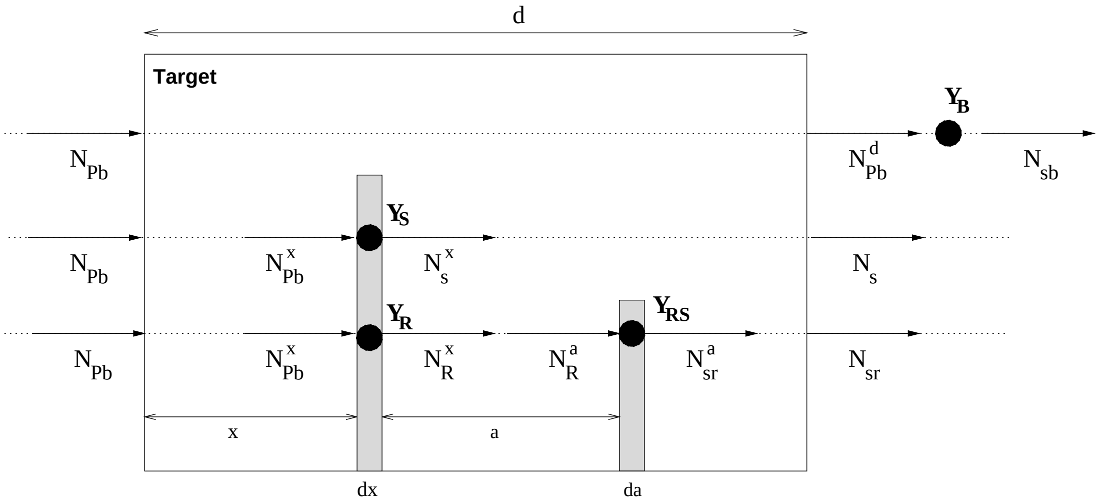

Figure 6.1: Cartoon of the different production channels for measured secondaries. The true yield Y_S of a secondary produced in a collision is the ratio of the number of secondaries N_S^x and the incident lead ions N_{Pb}^x. However, The number of measured secondaries in the beam line can be less than N_S^x because of absorption. On the other hand it can be larger since it gets extra contributions from reinteractions or interactions outside the target.

the measured N_m can be larger than N_S^x since it gets extra contributions from reinteractions or interactions outside the target.

Absorption

The number of Pb ions at a depth x as shown in figure 6.1 in the target is:

$$N_{Pb}^x = N_{Pb} \cdot e^{-x/\lambda_i}$$

where N_{Pb} is the number of incident Pb ions and λ_i the Pb-Pb interaction length. Therefore the number of secondaries N_s^x at a depth x writes:

$$N_s^x = N_{Pb} \cdot e^{-x/\lambda_i} \cdot Y_s$$

with Y_s the yield of secondaries.
In addition to the absorption of the incident beam also the produced secondaries are absorbed. With an absorption length for secondaries λ_s the N_s gets at the end of the target:

$$N_s = N_{Pb} \cdot e^{-x/\lambda_i} \cdot Y_s \cdot e^{-(d-x)/\lambda_{abs}}$$

Integrating N_s^x over the target thickness d gives:

$$N_s = \frac{N_{Pb} \cdot Y_s}{1/\lambda_i - 1/\lambda_s} \cdot \left(e^{-d/\lambda_i} - e^{-d/\lambda_s} \right)$$

Reinteraction

Besides the absorption described in the previous section, which results in a faked too low secondary rate, there is reinteraction or rescattering which increase the rate and so fake a too high rate.
We take into account the possibility that particles produced in the primary interaction Y_R (see 6.1) reinteract Y_{RS} producing a number of "secondaries" N^a_{sr}.
No tertiary interactions are considered in the model.
This additional production gives a term:

$$N_{sr} = \frac{N_{Pb} \cdot Y_R \cdot Y_{RS}}{1/\lambda_R - 1/\lambda_s} \cdot \left(\frac{e^{-d/\lambda_i} - e^{-d/\lambda_R}}{1/\lambda_i - 1/\lambda_R} + \frac{e^{-d/\lambda_i} - e^{-d/\lambda_s}}{1/\lambda_i - 1/\lambda_s} \right)$$

where λ_R is the absorption length of the reinteracting "secondary".

Interactions outside the target

Another faked extra contribution to the number of secondaries is given by the interaction Y_B of lead ions outside the target. Only contributions behind the target are considered. The interaction take place mainly in air. This gives a contribution of:

$$N_{sb} = Y_B \cdot N_{Pb} \cdot e^{-d/\lambda_i}.$$

Interpretation

The measured number of secondaries is:

$$N_m = N_{sb} + N_s + N_{sr}.$$

The goal is to determine Y_s. However, in this problem there are 6 additional parameters: Y_R, Y_{RS}, Y_B, λ_i, λ_s and λ_R.
Five of them are unknown, $\lambda_i = 37$mm is extrapolated from [47]. The idea is to fit N_m to the measured number of secondaries as a function of the target thickness. However, this could not be done, since it requires at least 7 measurements which are not available. A solution could be found by developing $N_s + N_{sr}$ to a form:

$$N_s + N_{sr} = a_1 \cdot d + a_2 \cdot d^2 + \ldots$$

which gives:

$$N_m = Y_B \cdot N_{Pb} \cdot e^{-d/\lambda_i} + a_1 \cdot d + a_2 \cdot d^2 + \ldots . \tag{6.1}$$

In this form N_m can easily be fit to the available measurements.
The problem is so transferred to the interpretation of the coefficients.which depend on the selection of the developing variable (e.g. λ_i/λ_S under the assumption that this ratio is small).

The result from different developments is that the linear term corresponds to the true yield per target thickness:

$$a_1 = Y_s/d.$$

All the other parameters appear only in higher order coefficients and cannot be disentangled.

6.1.2 Results

In 1998 we preformed target thickness scans at -20, -40, -70 and -100 GeV/c. Here the results from the -20 and -40 GeV/c data is presented. The acquired statistics at different target thicknesses is summarised in table 6.1. Also shown are the relative acceptances up to TOF3 and the particles which can be separated and counted in each setting. At these rigidities the time of flight fit allows to separate K$^-$, $\overline{\mathrm{p}}$ and $\overline{\mathrm{d}}$ if the lighter particles (π^-, μ^- and e$^-$) are vetoed by the Čerenkov counters. For the 40mm target and at -40 GeV/c also the K$^-$ or even the $\overline{\mathrm{p}}$ had to be vetoed because of their too high rate.

A compilation of the mass spectra for each setting can be found in appendix C. The particles are counted if they reach the TOF3 hodoscope (see figure 2.1). The number of observed secondaries with the reconstruction efficiency for each setting is listed in table 6.2.

In figure 6.2 the obtained ratios N_m/N_{Pb} are shown as a function of the target thickness for the -20 GeV/c data. The shown fit is done according to the model described in section 6.1.1. The values for the linear terms a_1 of the fit shown in figure 6.2 corresponds to:

$$Y_s/d = \frac{N_s}{N_{Pb}}\frac{1}{d}$$

used in equation 4.1 to calculate the cross section. One can see that even with thicker target we would still have gained in secondary rates in the beam line. It would be interesting to have measurements with thicker targets to see were the absorption of secondary starts to be relevant or what role rescattering plays.

The $Ed^3\sigma/dp^3$ calculated with the above determined Y_S/d are given in table 6.3 together with the ones from the -40 GeV/c setting.

A compilation of these cross sections with previously measured ones can be found in section 6.3.

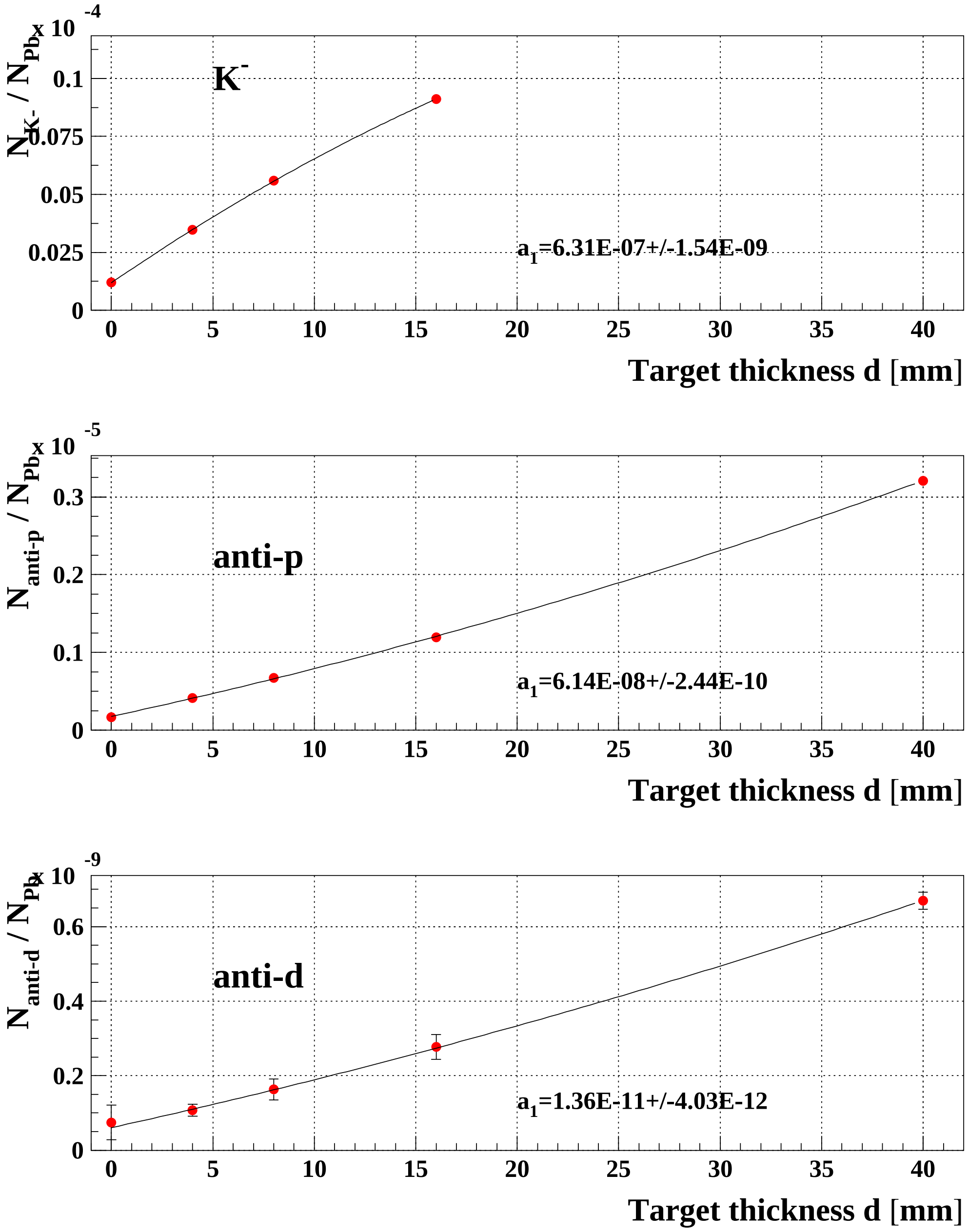

Figure 6.2: The ratios N_m/N_{Pb} are shown as a function of the target thickness for K^-, $\overline{\mathrm{p}}$ and $\overline{\mathrm{d}}$. The values shown are the linear terms of the fit corresponding to $\frac{N_s}{N_{Pb}}\frac{1}{d}$ used to calculate the invariant differential cross sections. The data shown is from the -20 GeV/c setting in 1998.

Rigidity [GeV/c]	Target thickness [mm]	Particles	Pb ions on target	Acceptance
-20	16 mm	K^-,$\overline{\mathrm{p}}$ and $\overline{\mathrm{d}}$	$2.55 \cdot 10^{11}$	$3.14 \cdot 10^{-8}$
-20	4 mm	K^-,$\overline{\mathrm{p}}$ and $\overline{\mathrm{d}}$	$4.1 \cdot 10^{11}$	$3.14 \cdot 10^{-8}$
-20	8 mm	K^-,$\overline{\mathrm{p}}$ and $\overline{\mathrm{d}}$	$2.07 \cdot 10^{11}$	$3.14 \cdot 10^{-8}$
-20	0 mm	K^-,$\overline{\mathrm{p}}$ and $\overline{\mathrm{d}}$	$3.44 \cdot 10^{10}$	$3.14 \cdot 10^{-8}$
-20	40 mm	$\overline{\mathrm{p}}$ and $\overline{\mathrm{d}}$	$1.29 \cdot 10^{12}$	$3.14 \cdot 10^{-8}$
-40	40 mm	$\overline{\mathrm{p}}$	$4.65 \cdot 10^{11}$	$3.60 \cdot 10^{-8}$
-40	40 mm	$\overline{\mathrm{d}}$	$1.45 \cdot 10^{12}$	$3.60 \cdot 10^{-8}$
-40	0 mm	$\overline{\mathrm{p}}$ and $\overline{\mathrm{d}}$	$4.39 \cdot 10^{10}$	$3.60 \cdot 10^{-8}$
-40	8 mm	$\overline{\mathrm{p}}$ and $\overline{\mathrm{d}}$	$1.04 \cdot 10^{11}$	$3.60 \cdot 10^{-8}$
-40	16 mm	$\overline{\mathrm{p}}$ and $\overline{\mathrm{d}}$	$4.85 \cdot 10^{10}$	$3.60 \cdot 10^{-8}$

Table 6.1: Summary of the acquired statistics for the target thickness scans at -20 GeV/c and -40 GeV/c in 1998. The name of the setting includes the information about the rigidity. Also shown are the relative acceptances up to TOF3 an the particles which can be counted in each setting.

Rigidity [GeV/c]	K^-	$\overline{\mathrm{p}}$	$\overline{\mathrm{d}}$	reconstruction efficiency
-20	$1.546 \cdot 10^5$	$2.325 \cdot 10^5$	54	0.76
-20	$9.61 \cdot 10^4$	$1.312 \cdot 10^5$	34	0.77
-20	$7.76 \cdot 10^4$	$1.075 \cdot 10^5$	26	0.77
-20	$2.81 \cdot 10^3$	$4.34 \cdot 10^3$	2	0.78
-20		$3.191 \cdot 10^6$	666	0.77
-40		$2.169 \cdot 10^6$		0.79
-40			2049	0.74
-40		$9.08 \cdot 10^3$	6	0.73
-40		$5.92 \cdot 10^4$	30	0.74
-40		$7.16 \cdot 10^1$	33	0.72

Table 6.2: Summary of the number of identified particles and the reconstruction efficiency for each setting.

Particle	Rigidity [GeV/c]	Rapidity	Inv. diff. cross section [barn/GeV$^2c^3$]
K^-	-20	4.40	15.22 ± 0.04
$\overline{\mathrm{p}}$	-20	3.75	1.483 ± 0.006
$\overline{\mathrm{d}}$	-20	3.06	$(3.3 \pm 1.0) \cdot 10^{-4}$
$\overline{\mathrm{p}}$	-40	4.45	$(3.39 \pm 0.02) \cdot 10^{-1}$
$\overline{\mathrm{d}}$	-40	3.75	$(1.9 \pm 0.5) \cdot 10^{-4}$

Table 6.3: Invariant differential particle production cross sections from the 1998 data.

6.2 Anti helium-3

After having seen anti protons and anti deuterons, the next challenge is to find anti nuclei with a mass of 3 amu, i.e. $\overline{{}^3\mathrm{He}}$ or $\overline{\mathrm{t}}$. The most copious production of anti matter is reached at mid rapidity corresponding to a rigidity of 12.8 GeV/c for $\overline{{}^3\mathrm{He}}$ and of 25.7 GeV/c for $\overline{\mathrm{t}}$. Assuming the same invariant differential production cross section, the probability of seeing an $\overline{{}^3\mathrm{He}}$ is four times larger than seeing an $\overline{\mathrm{t}}$ at the same rigidity because of the momentum dependency of the acceptance. Another advantage of the doubly charged objects lies in the net discrimination of higher charges (see section 4.3). One first $\overline{{}^3\mathrm{He}}$ was found in NA52 during 1994 in a -20GeV/c setting ([41, 44]). In 1998 one additional $\overline{{}^3\mathrm{He}}$ has been found at a rigidity of -20 GeV/c and three at -40 GeV/c.

The charge distribution of the -40 GeV/c setting in 1998 is shown in figure 6.3. One clearly identifies 4 candidates for Z=-2. One of them showed to be a two particle event after a closer look, three could be confirmed to be $\overline{{}^3\mathrm{He}}$. As an example one of this three is presented here in detail. The dE/dx of it, measured in individual counters along the beam line, is shown in figure 6.4. All the counters show an enhanced pulse height consistent with $Z = -2$. At the end of the beam line the $\overline{{}^3\mathrm{He}}$ deposited an energy of $E = 85.7$ GeV, which is compatible with a doubly charged object at a rigidity of -40 GeV/c. In the MWPC and in the TOF hodoscopes no multiple entries were recorded excluding multiple particles in the beam line. Also the reconstructed mass of $m = 3.5$ GeV/c is in accordance with an $\overline{{}^3\mathrm{He}}$.

The resulting invariant differential $\overline{{}^3\mathrm{He}}$ production cross sections at -20 GeV/c and -40GeV/c are shown in table 6.4. The cross section at -20 GeV/c include the 1994, 1995 and 1998 statistics.

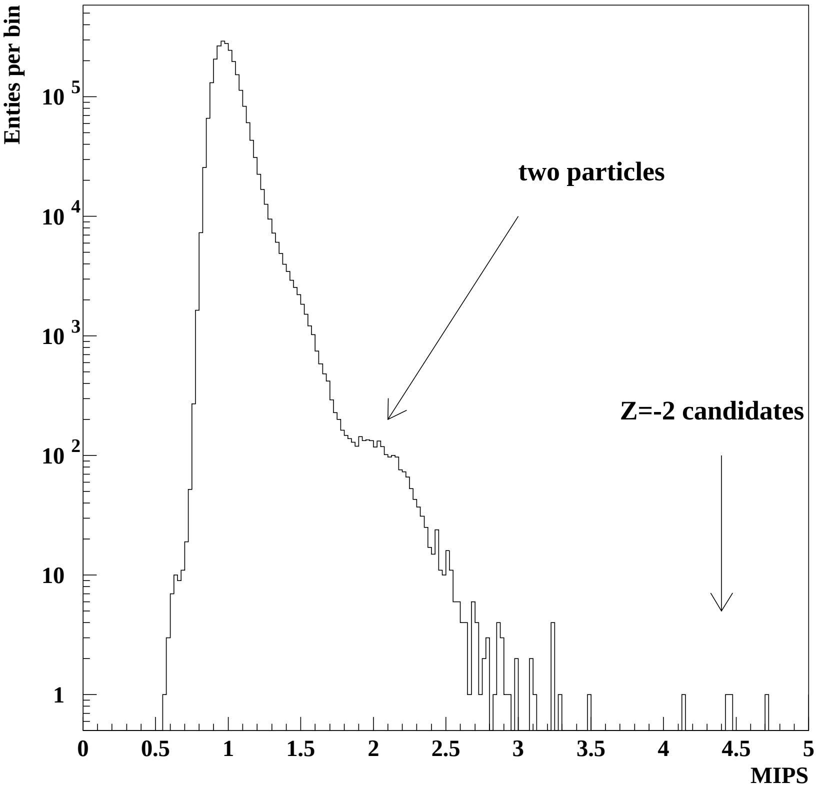

Figure 6.3: Charge distribution at -40GeV/c. One clearly identifies 4 candidates with a charge of Z=-2. The shoulder in the Landau tail is due to two particle events which have not been cut for this analysis. In fact also one of the four candidates showed to be a two particle event. The other three were confirmed to be anti helium 3.

Rigidity [GeV/c]	Rapidity	Number of events	Number of Pb+Pb interactions 94+95+98	Inv. diff. cross section [barn c^3/GeV^2]
-20	3.4	2	$8.9 \cdot 10^{11}$	$(4.1 \pm 2.9) \cdot 10^{-7}$
-40	4.0	3	$13.4 \cdot 10^{11}$	$(1.3 \pm 0.7) \cdot 10^{-7}$

Table 6.4: Invariant differential production cross section of $\overline{^3\mathrm{He}}$.

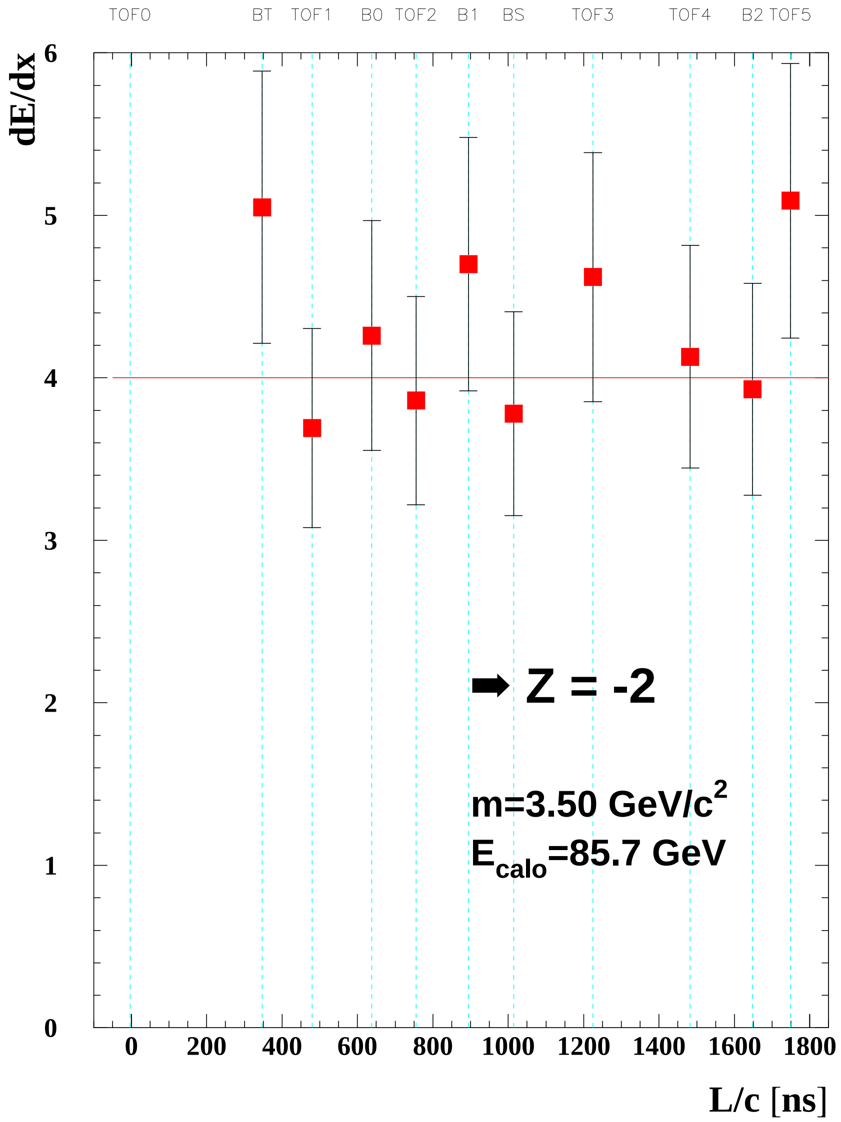

Figure 6.4: Energy loss in the scintillators along the beam line for one $\overline{^{3}\mathrm{He}}$ at -40 GeV/c. All the counters show an enhanced pulse height consistent with $Z = -2$. The energy of $E = 85.7$ GeV measured in the calorimeter at the end of the spectrometer is also consistent with a double charge.

6.3 Particle compilation and discussion

A compilation of the invariant differential anti particle production cross sections is given in figure 6.5.
Previous data ([44, 61]) is shown as open symbols in figure 6.5. The points from the target thickness scans in 1998 are shown as full circles and the $\overline{^3\mathrm{He}}$ cross sections as full squares with the full statistics of 1994,1995 and 1998. For all the points no centrality requirements have been applied. The values for anti protons are not corrected for Δ and Λ decays. The error bars correspond to statistical errors only. We assume a systematic error of 25% for the cross sections, which is mainly due to the uncertainties in the acceptance of the beam line and in the counting of the incident lead ions.
As can be seen some of the cross sections calculated with the target scan model are lower than the previously published ones. This can be understood as the applied model includes now rescattering which has not been considered before. The different method to derive cross sections is not the only difference compared to 1995. Also changes to the beam line have been applied. This includes movement of magnets to increase the acceptance and the installation of new scintillators and wire chambers increasing the multiple scattering and absorption of secondaries. To check the systematics of these detector modifications the cross sections have been also calculated using the previous method without rescattering. A comparison of such calculated cross sections is shown in table 6.5 for the 4mm target at -20 GeV/c available for 1995 and 1998. The agreement of the K$^-$ and anti proton values at 4mm means, that the changes to the beam line have been considered correctly in 1998. The lower values using the target scan method are therefore really due to rescattering. The discrepancy of the anti deuteron values needs further investigations.

Particle	p/Z [Gev/c]	y	1995 4mm	1998 4mm	1998 target scan
$\overline{\mathrm{p}}$	-20	3.75	1.993 ± 0.054	1.921 ± 0.005	1.483 ± 0.006
$\overline{\mathrm{d}}$	-20	3.06	$(7.0 \pm 1.5) \cdot 10^{-4}$	$(3.2 \pm 0.5) \cdot 10^{-4}$	$(3.3 \pm 1.0) \cdot 10^{-4}$
K$^-$	-20	4.40	15.6 ± 0.5	16.503 ± 0.005	15.22 ± 0.04

Table 6.5: Invariant differential production cross section with a 4mm target at -20 GeV/c available for 1995 and 1998 without rescattering. This values are compared to the new method, including rescattering, making use of the target scan data from 1998.

The $\overline{^3\mathrm{He}}$ found in 1994 at -20 GeV/c was a lucky punch and the cross section is now lower since in the much higher statistics of 1998 only one additional $\overline{^3\mathrm{He}}$ has been found.
The cross sections can be taken as input for models describing for example the thermodynamics of Pb+Pb collision. The results can also be interpreted within

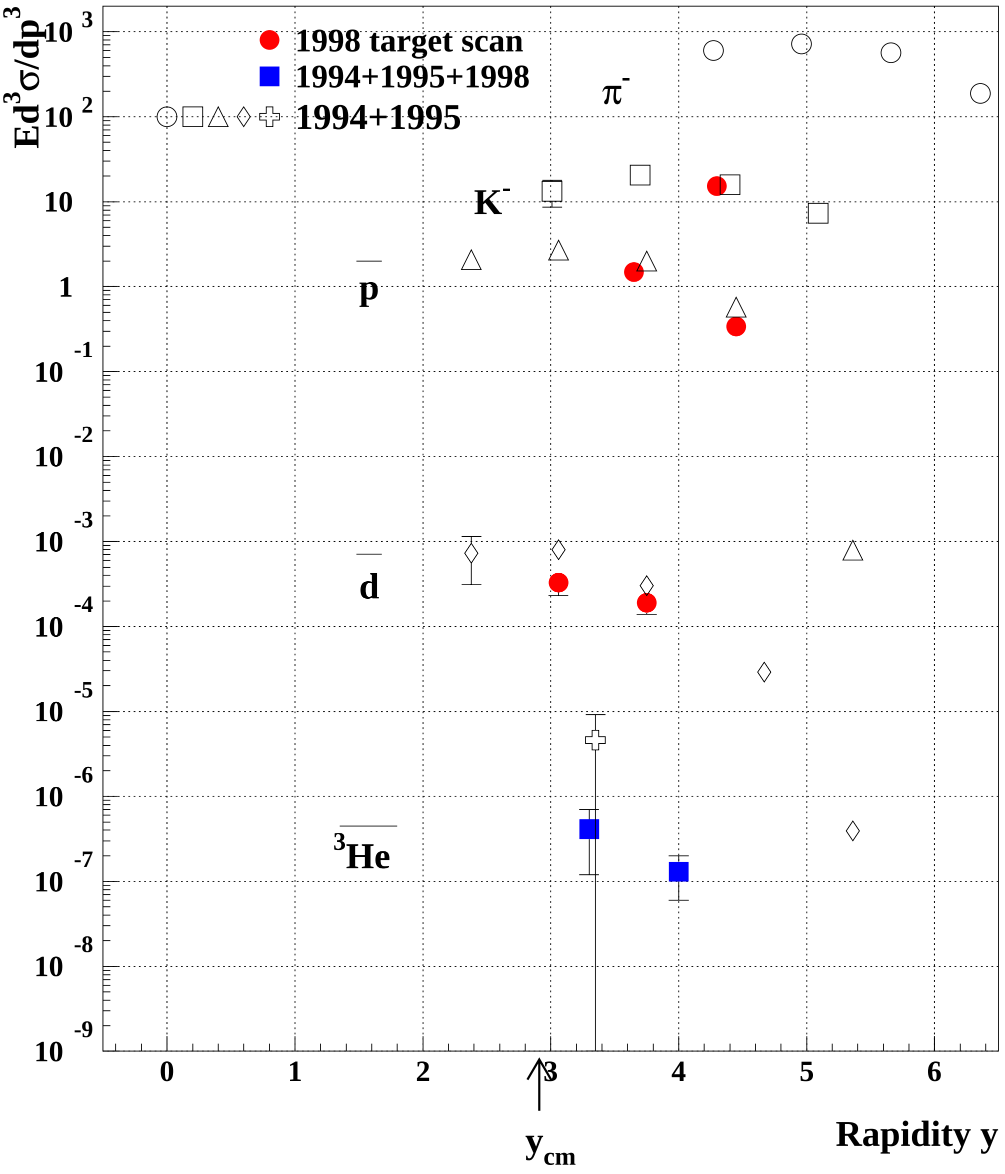

Figure 6.5: Invariant differential antiparticle production cross sections. The open symbols are from already published data [44, 61]. The filled circles are the new points from the 1998 data. Only statistical errors are shown. Some new points are artificially displaced horizontally in order to distinguish the error from the previous point (open symbol).

a coalescence model. One can see that the production probabilities of $\overline{\mathrm{p}}$, $\overline{\mathrm{d}}$ and $\overline{^3\mathrm{He}}$ differ at the same rapidity by three orders of magnitude for each nucleon added. More accurate calculations are being performed.

Chapter 7

Conclusions and outlook

The NA52 has had its last data taking in 1998. The final results from the strangelet and particle searches could be presented.

No strangelets have been found. NA52 has performed a very specific search at $p_t = 0$ with a very high statistics. The obtained differential upper strangelet production cross sections ($10^{-6} - 10^{-8}$ depending on the rigidity) are considerable. To answer the question of the overall existence of strangelets we extrapolate to the full phase space and obtain total production limits of $2 \cdot 10^{-10}$. The achieved total sensitivity limits exclude some of the predicted strangelets and are comparable to strangelet search experiments at BNL-AGS. The question of the existence of strangelets is today still open. The investigation of heavy ion collisions is continued at higher energies with the recently started RHIC at Brookhaven and will go on at LHC at CERN. In astrophysics the study of neutron starts is a promising field to test the existence of strange quark matter.

Besides the strangelet search, the small acceptance gives to NA52 the possibility to look at single particles from the collision and develop its very good particles identification capabilities. Particle production studies could be performed over a wide range of rapidity. Besides anti protons, thousands of anti deuterons and even 5 anti helium-3 could be identified. Invariant differential production cross sections have been presented. The interpretation of particle productions in terms of temperature, chemical potential and radii of the colliding system is currently being prepared for publication. In 1998 also a segmented quartz fibre calorimeter [65, 66] has been added to the setup just behind the target. This gives the possibility to measure the impact parameter of the colliding lead ions. Impact parameter dependency of the thermodynamical interpretations is also under study.

Bibliography

[1] S. A. Chin and A. K. Kerman. Possible long-lived hyperstrange multiquark droplets. Phys. Rev. Lett. **43** (18) (1979) 1292–1295

[2] C. Greiner and H. Stöcker. Distillation and survival of strange-quark-matter droplets in ultrarelativistic heavy-ion collisions. Phys. Rev. D **44** (11) (1991) 3517–3529

[3] E. Farhi and R. L. Jaffe. Searching for strange matter by heavy-ion activation. Phys. Rev. D **32** (9) (1985) 2452–2455

[4] J. Madsen. Mass formula for strange and nonstrange quark matter. Phys. Rev. D **47** (11) (1993) 5156–5160

[5] C. Greiner and J. Schaffner-Bielich. Physics of strange matter. In R. K. Gupta and W. Greiner, eds., to be published in *Heavy Elements and Related New Phenomena* (World Scientific, Singapore, 1998) Preprint LBNL-41324, e-print archive `nucl-th/9801062`

[6] E. P. Gilson and R. L. Jaffe. Stability of very small strangelets. Phys. Rev. Lett. **71** (3) (1993) 332–335

[7] J. Madsen. Shell model versus liquid drop model for strangelets. Phys. Rev. D **50** (5) (1994) 3328–3331

[8] R. Klingenberg. Strange quark matter searches. J. Phys. G: Nucl. Part. Phys. **25** (11) (1999) R273–R308

[9] C. Greiner and J. Schaffner. Physics of strange matter for relativistic heavy-ion collisions. Int. J. Mod. Phys. E **5** (2) (1996) 239–300

[10] J. Schaffner-Bielich and A. P. Vischer. Charmlets. Phys. Rev. D **57** (2) (1998) 4142–4153

[11] A. R. Bodmer. Collapsed nuclei. Phys. Rev. D **4** (6) (1971) 1601–1606

[12] E. Witten. Cosmic separation of phases. Phys. Rev. D **30** (2) (1984) 272–285

[13] A. De Rújula and S. L. Glashow. Nuclearites — a novel form of cosmic radiation. Nature **312** (1984) 734–737

[14] H. Cui, O. Eugster, W. Ke, P. LeCoultre and X. Tang. Search for fossil tracks formed by cosmic nuclearites in meteorites. Chin. Phys. Lett. **5** (5) (1988) 237–239

[15] M. Brügger, K. Lützenkirchen, S. Polikanov, G. Herrmann, M. Overbeck, N. Trautmann, A. Breskin, R. Chechik, Z. Fraenkel and U. Smilansky. Search for strange matter by Rutherford backscattering. Nature **337** (1989) 434–436

[16] T. K. Hemmick, D. Elmore, T. Gentile, P. W. Kubik, S. L. Olsen, D. Ciampa, D. Nitz, H. Kagan, P. Haas, P. F. Smith, B. B. McInteer and J. Bigeleisen. Search for low-Z nuclei containing massive stable particles. Phys. Rev. D **41** (7) (1990) 2074–2080

[17] M. C. Perillo Isaac, Y. D. Chan, R. Clark, M. A. Deleplanque, M. R. Dragowsky, P. Fallon, I. D. Goldman, R.-M. Larimer, I. Y. Lee, A. O. Macchiavelli, R. W. MacLeod, K. Nishiizumi, E. B. Norman, L. S. Schroeder and F. S. Stephens. Search for strange matter by heavy ion activation. Phys. Rev. Lett. **81** (12) (1998) 2416–2419

[18] R. L. Jaffe. Perhaps a stable dihyperon. Phys. Rev. Lett. **38** (5) (1977) 195–198. (erratum 617)

[19] M. Danysz *et al.*. The identification of a double hyperfragment. Nucl. Phys. **49** (1963) 121–132

[20] A. S. Carroll, I.-H. Chiang, R. A. Johnson, T. F. Kycia, K. K. Ki, L. S. Littenberg and M. D. Marx. Search for six-quark states. Phys. Rev. Lett. **41** (12) (1978) 777–780

[21] A. T. M. Aerts and C. B. Dover. $(\mathrm{K}^-,\mathrm{K}^+)$ reaction and the dibaryon H. Phys. Rev. Lett. **49** (24) (1982) 1752–1755

[22] S. Aoki *et al.*. Search for the H dibaryon in $(\mathrm{K}^-,\mathrm{K}^+)$ reactions. Phys. Rev. Lett. **65** (14) (1990) 1729–1732

[23] J. K. Ahn *et al.*. Search for the H dibaryon in $(\mathrm{K}^-,\mathrm{K}^+)$ reaction with scintillating fiber active target. Phys. Lett. **B378** (1996) 53–58

[24] H.-C. Liu and G. L. Shaw. Production and detection of metastable strange-quark droplets in heavy-ion collisions. Phys. Rev. D **30** (5) (1984) 1137–1140

[25] H. J. Crawford, M. S. Desai and G. L. Shaw. Prediction of enhanced production of strange matter at CERN SPS. Phys. Rev. D **48** (9) (1993) 4474–4477

[26] J. Schaffner-Bielich, C. Greiner, H. Stöcker and A. P. Vischer. Properties of exotic matter for heavy ion searches. J. Phys. G: Nucl. Part. Phys. **23** (12) (1997) 2107–2115

[27] A. J. Baltz, C. B. Dover, S. H. Kahana, Y. Pang, T. J. Schlagel and E. Schnedermann. Strange cluster formation in relativistic heavy ion collisions. Phys. Lett. **B325** (1994) 7–12

[28] C. Greiner, P. Koch and H. Stöcker. Separation of strangeness from antistrangeness in the phase transition from quark to hadron matter: Possible formation of strange quark matter in heavy-ion collisions. Phys. Rev. Lett. **58** (18) (1987) 1825–1828

[29] J. Schaffner-Bielich, C. Greiner, A. Diener and H. Stöcker. Detectability of strange matter in heavy ion experiments. Phys. Rev. C **55** (6) (1997) 3038–3046

[30] F. S. Rotondo. Search for strange matter in heavy ion collisions at Brookhaven's AGS. Nucl. Phys. B (Proc. Suppl.) **24B** (1991) 265–268

[31] M. Aoki *et al.*. Measurements at 0^o of negatively charged particles and antinuclei produced in collision of $14.6A$GeV$/c$ Si on Al, Cu, and Au targets. Phys. Rev. Lett. **69** (16) (1992) 2345–2348

[32] A. Rusek *et al.*. Strangelet search and light nucleus production in relativistic Si+Pt and Au+Pt collisions. Phys. Rev. C **54** (1) (1996) R15–R19

[33] D. Beavis *et al.*. Search for new metastable particles produced in Au+Au collisions at $10.8A$GeV$/c$. Phys. Rev. Lett. **75** (17) (1995) 3078–3081

[34] M. G. Munhoz. Search for neutral strangelets at the relativistic heavy ion experiment E864. J. Phys. G: Nucl. Part. Phys. **25** (1999) 417–422

[35] C. B. Dover, P. Koch and M. May. Production of the H dibaryon in relativistic heavy-ion collisions. Phys. Rev. C **40** (1) (1989) 115–125

[36] S. E. Eiseman *et al.*. Neutral V production with $14.6 \times A$GeV$/c$ silicon beams. Phys. Lett. **B248** (3,4) (1990) 254–258

[37] R. Longacre *et al.*. H_0 candidates from the decay $\mathrm{H}_0 \to \Sigma^-\mathrm{p}$, observed in heavy ion collisions with $14.6 \times A$GeV$/c$ Si beam on Pb target. Nucl. Phys. A **590** (1995) 477c–482c

[38] J. Belz *et al.*. Search for the weak decay of an H dibaryon. Phys. Rev. Lett. **76** (18) (1996) 3277–3280. see also [39]

[39] J. Belz *et al.*. Addendum to "Search for the weak decay on an H dibaryon". Phys. Rev. C **56** (2) (1997) 1164

[40] H. Caines *et al.*. First results from the H_0 di-baryon search and hyperon production measurements by the AGS experiment 896. vol. 661 of *Nucl. Phys.* A (North-Holland Elsevier Science, 1999) 170c–169c

[41] R. Klingenberg. Search for Charged Strangelets in Pb-Pb Interactions at $158 \cdot A\text{GeV}/c$. Ph.D. thesis, University of Bern, Bern, (1996)

[42] K. L. Brown and C. Iselin. Decay turtle, a computer program for simulating charged particle beam transport systems, including deacy calculations. Tech. Rep. CERN-74-2, CERN, (1974)

[43] T. Lindén. Strangelet search and particle production studies in Pb-Pb collisions at $158{\cdot}A$ GeV/c with the H6 beamline spectrometer at CERN. Ph.D. thesis, University of Helsinki, Helsinki, (2000)

[44] F. Stoffel. Particle Production Studies in Pb+Pb Collisions at $158 \cdot A\text{GeV}/c$. Ph.D. thesis, University of Bern, Bern, (1997)

[45] W. Volken. Strangelet Search in S-W Collisions at 200GeV/c per Nucleon. Ph.D. thesis, University of Bern, Bern, (1994)

[46] P. Hess. Produktion von Kernfragmenten in Pb+Pb-Stössen bei $158 \cdot A\text{GeV}/c$. Diplomarbeit, Universität Bern, Bern, (1997)

[47] E. Andersen *et al.*. A measurement of cross sections for ^{32}S interactions with Al, Fe, Cu, Ag and Pb at 200 GeV/c per nucleon. Phys. Lett. **B220** (1989) 328–332

[48] F. Dittus *et al.*. First look at NA52 data on Pb-Pb interactions at $158A\text{GeV}/c$. In J. Rafelski, ed., *Strangeness in Hadronic Matter (Jan 1995, Tucson, AZ)*, vol. 340 of *AIP Conf. Proc.* (American Institute of Physics, Woodbury, NY, USA, 1995) 24–31

[49] R. Klingenberg *et al.*. Strangelet search and antinuclei production studies in Pb+Pb collisions. Nucl. Phys. A **610** (1996) 306c–316c

[50] R. Klingenberg *et al.*. Strangelet search in Pb-Pb interactions at $158A\text{GeV}/c$. In J. Lemonne, C. Vander Velde and F. Verbeure, eds., *Proc. Int. Europhysics Conf. on Strangeness on High Energy Physics (27 Jul – 2 Aug 1995, Brussels, Belgium)* (World Scientific, Singapore, 1996) 361–362

[51] R. Klingenberg *et al.*. Strangelet search and particle production studies in Pb+Pb collisions. In J. Trân Thanh Vân, ed., *Proc. XXXIInd Rencontres de Moriond '97 QCD and High Energy Hadronic Interactions (March 22-29, 1997, Les Arcs, Savoie, France)* (Editions Frontieres, Paris, 1997) 497–502

[52] F. Stoffel *et al.*. Strangelet search and particle production studies in Pb+Pb collisions at 158AGeV/c at CERN SPS. In T. Csörgő, P. Lévai and J. Zimányi, eds., *Proc. Conf. on Strangeness in Hadronic Matter (15–17 May 1996, Budapest, Hungary)*, vol. 4 of *APH N. S., Heavy Ion Physics* (Akadémiai Kiadó, Budapest, 1996) 429–434

[53] B. Alper, H. Bøggild, P. Booth, L. J. Carroll, G. von Dardel, G. Damgaard, B. Duff, J. N. Jackson, G. Jarlskog, L. Jönsson, A. Klovning, L. Leistam, E. Lillethun, S. Olgaard-Nielsen, M. Prentice and J. M. Weiss. The production of charged particles with high transverse momentum in proton-proton collisions at the CERN ISR. Nucl. Phys. B **87** (1975) 19–40

[54] H. J. Crawford, M. S. Desai and G. L. Shaw. Production and detection of drops of strange matter. Phys. Rev. D **45** (3) (1992) 857–865

[55] H. J. Crawford *et al.*. Search for new negative particles produced in 14.6AGeV/c Si+A interactions. Nucl. Phys. B (Proc. Suppl.) **24B** (1991) 251–254

[56] T. A. Armstrong *et al.*. Search for strange quark matter produced in relativistic heavy ion collisions, (2000). submitted to *Phys. Rev. C*, e-print archive `nucl-ex/0010017`

[57] J. Barrette *et al.*. Search for strange quark matter in high-energy heavy-ion collisions. Phys. Lett. **B252** (4) (1990) 550–554

[58] K. Borer, F. Dittus, D. Frei, E. Hugentobler, R. Klingenberg, U. Moser, K. Pretzl, J. Schacher, F. Stoffel, W. Volken, K. Elsener, K. D. Lohmann, C. Baglin, A. Bussière, J. P. Guillaud, G. Appelquist, C. Bohm, B. Hovander, B.Selldèn and Q. P. Zhang. Strangelet search in S-W collisions at 200AGeV/c. Phys. Rev. Lett. **72** (10) (1994) 1415–1418

[59] P. Braun-Munzinger and J. Stachel. Production of strange clusters and strange matter in nucleus-nucleus collisions at the AGS. J. Phys. G: Nucl. Part. Phys. **21** (1995) L17–L20

[60] M. S. Berger and R. L. Jaffe. Radioactivity in strange quark matter. Phys. Rev. C **35** (1) (1987) 213–225

[61] R. Arsenescu. Pion Production Studies in Pb+Pb Collisions at 158AGeV/c. Ph.D. thesis, University of Bern, Bern, (1999)

[62] G. Ambrosini *et al.*. Antinuclei production in Pb+Pb collisions at 158AGeV/c. Phys. Lett. **B376** (1996) 245–250

[63] R. Arenescu *et al.*. New results from NA52 on particle production in Pb-Pb collisions at 158AGeV/c. J. Phys. G: Nucl. Part. Phys. **25** (2) (1999) 225–233

[64] G. Ambrosini *et al.*. Baryon and antibaryon production in lead-lead collisions at 158AGeV/c. Phys. Lett. **B417** (1998) 202–210

[65] M. Weber. Studie von Teststrahldaten eines Quarzfiber-Blei Kalorimeters. Diplomarbeit, Universität Bern, Bern, (1997)

[66] M. Weber *et al.*. A segmented quartz-fiber lead calorimeter. (1998)

Appendix A

Rigidity vs rapidity

Rigidity R and rapidity y are two quantities related to the longitudinal momentum of the particles in the beam line. The rigidity is used since defined by the spectrometer, and the rapidity is often used in results since additive under Lorentz transformations.
This appendix was included since the shown table and figure were often used by the author as a reference during the writing of the thesis.
The relations between R and y are:

$$y = \text{atanh}(\beta) = \text{atanh}(\frac{1}{\sqrt{1 + \left(\frac{m/Z}{R}\right)^2}}$$

$$R = \frac{m/Z}{\sqrt{(1/\tanh(y))^2 - 1}}$$

Particle	m/Z [amu]	Momentum [GeV]	Rigidity [GeV/c]	Rapidity
p	1.	8.6	8.6	2.91
d	2.	17.1	17.1	2.91
t	3.	25.7	25.7	2.91
^{3}He	1.5	25.7	12.8	2.91
α	2.	34.2	17.1	2.91
Strangelet	7.	60.2	60.2	2.91

Table A.1: Momentum and rigidity for selected particles at center of mass (mid-) rapidity. Anti particles have the same values.

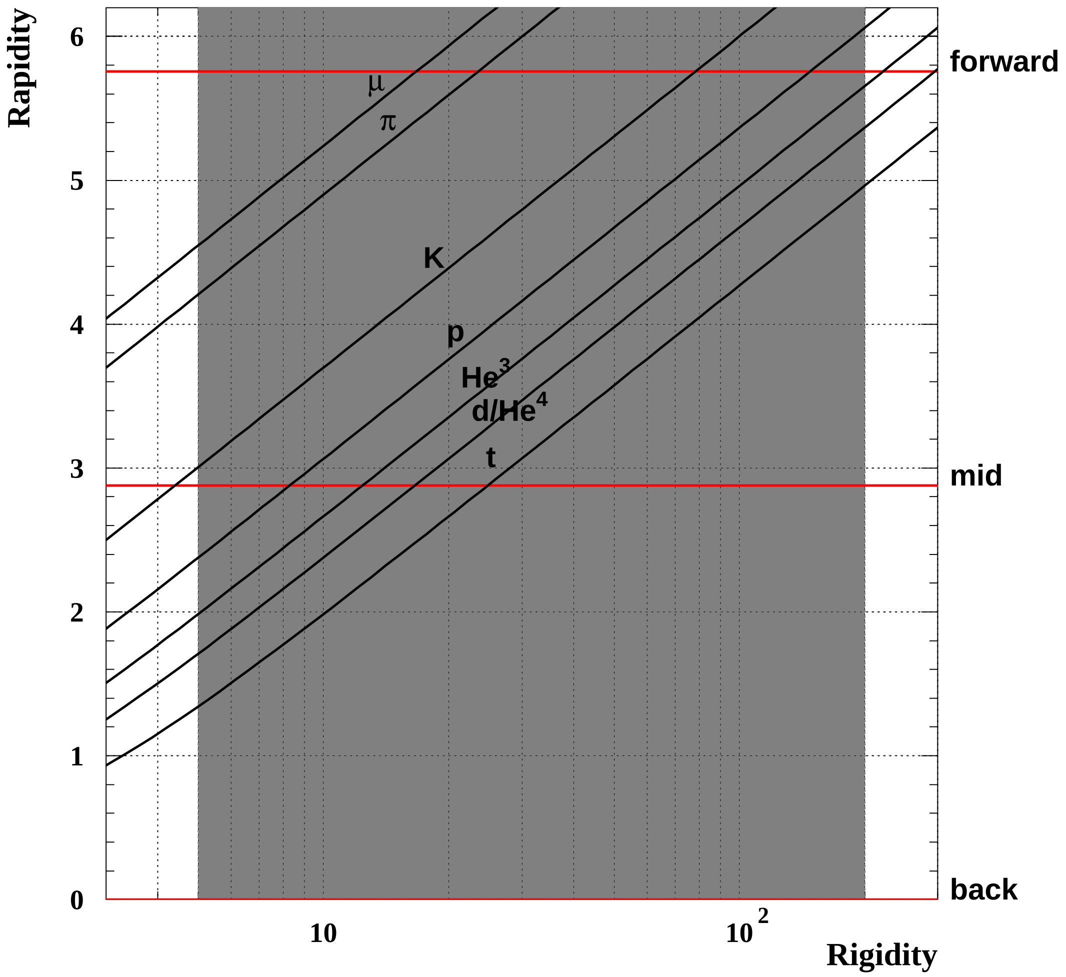

Figure A.1: Rapidity versus rigidity for different particle types. The dynamic range of the H6 beam line is shaded.

Appendix B

Selected detectors

Here, a more detailed description of detectors with important features for the analysis is given. This includes Čerenkov counters and the quartz counter TOF0.

B.1 Čerenkov counters

Threshold Čerenkov counters (Č0-Č2) are used to veto and/or tag particles with high velocities, which correspond to small $m/|Z|$. At a rigidity R the threshold mass to charge ratio m/Z below which no Čerenkov light is produced is related to the index of refraction n by:

$$\frac{1}{1+\frac{1}{2}\cdot\left(\frac{m/Z}{p/Z}\right)^2}=\frac{1}{n}.$$

In the threshold Čerenkov counters the index of refraction is changed by varying the pressure p of nitrogen in the detector to discriminate particles above a certain m/Z.
The relation between index of refraction and not too big pressures can be taken as linear:

$$(n-1)=(n_0-1)\cdot\frac{p}{p_0}.$$

For Nitrogen N_2 the index of refraction is $n_0 = 1.000298$ at 1.013 bar.
An overview on threshold pressures for different particle types as a function of the rigidity R is given in figure B.1.

B.2 TOF0

TOF0 is the only NA52 detector located in front of the target. It consists of four quartz quadrants. To have a deep understanding of this detector is crucial

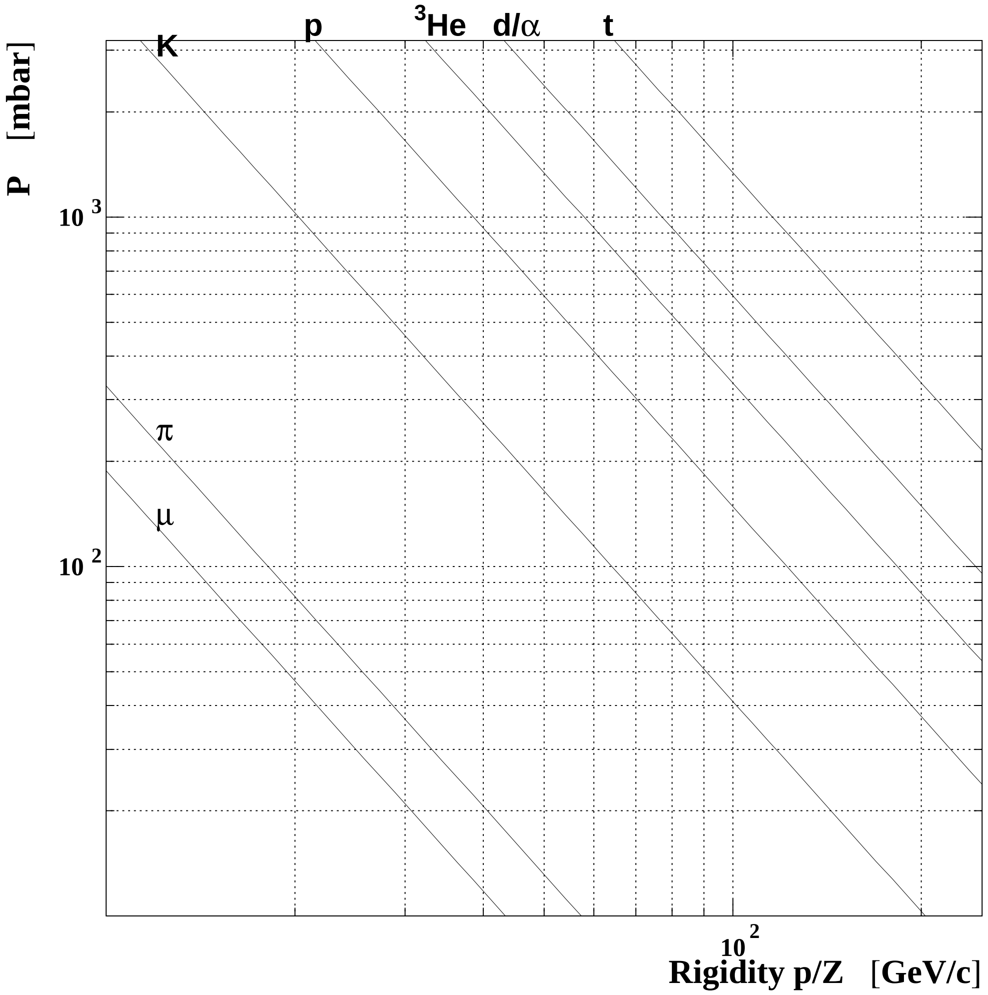

Figure B.1: Cerenkov threshold pressures as a function of rapidity for different particle types.

for the experiment. TOF0 lies at the largest distance from the trigger counter B1 and therefore has the largest lever in the TOF fit. Additionally it is used for counting the incident lead ions, which is essential for cross section calculations.

In particular pile up is a problem for TOF0 for both of the mentioned purposes, especially during 1998 when the incident lead ions reached 10^8 lead ions per second.

To cope with the high rates, each of the four quadrants is read out by a fourfold time demultiplexing system. In this way the counter has a double pulse resolution of 7 ns for statistically nicely distributed lead ions on the four quadrants.

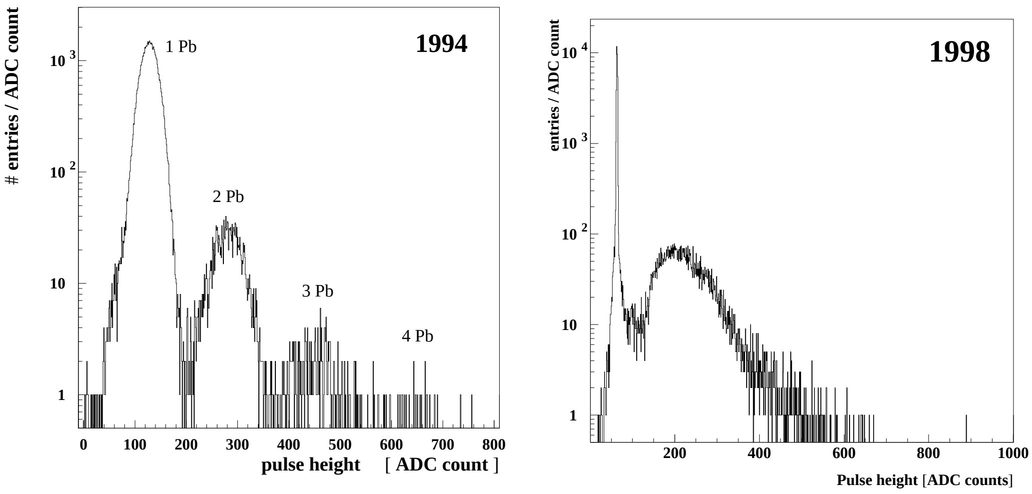

Figure B.2: Comparison of the pulse height spectrum of TOF0 in 1994 and 1998. In 1998 it became more difficult to recognise pile up.

The demultiplexing also assures that the time of up to 16 lead ions can be recorded. The time resolution of each time measurement is (100 ± 20) ns. The presumably correct lead ion can be determined offline by extrapolating a TOF fit to TOF0.

Additional time information of incident lead ions with a time resolution of 10 ns are also stored in a window of 2.5 μs around the trigger. From this information the homogeneity of the spill extraction and the mean rate of incident lead ions around the trigger can be estimated.

For the event by event analysis pile up can be identified by looking at the pulse height. However, the radiation damage of the detector limited the capacity of this method for the data taken in 1998. A comparison of the TOF0 pulse height spectrum in 1994 and in 1998 can be seen in figure B.2.

The analysis method for the lead ion counting is described in 4.4.

Appendix C

Compilation of analysed settings

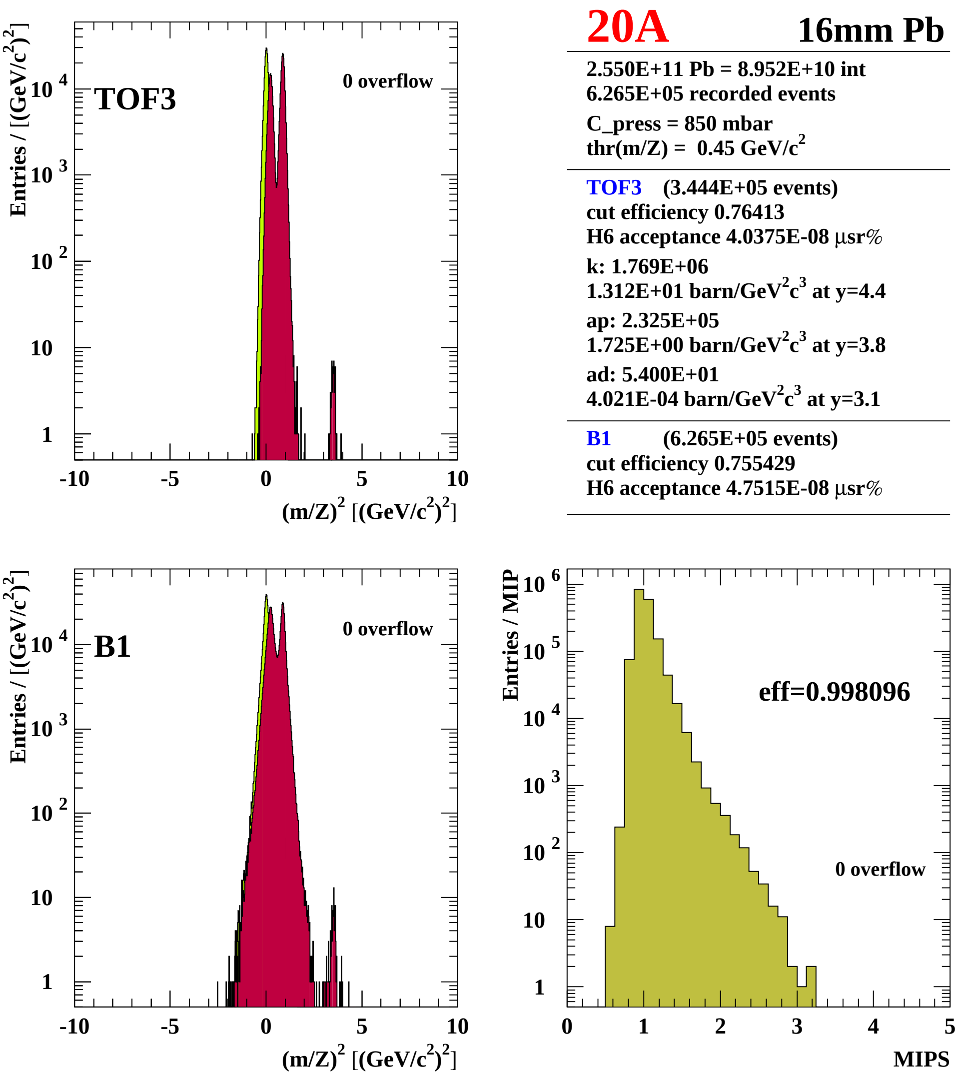

20A **16mm Pb**

2.550E+11 Pb = 8.952E+10 int
6.265E+05 recorded events
C_press = 850 mbar
thr(m/Z) = 0.45 GeV/c^2

TOF3 (3.444E+05 events)
cut efficiency 0.76413
H6 acceptance 4.0375E-08 µsr%
k: 1.769E+06
1.312E+01 barn/GeV^{2}c^3 at y=4.4
ap: 2.325E+05
1.725E+00 barn/GeV^{2}c^3 at y=3.8
ad: 5.400E+01
4.021E-04 barn/GeV^{2}c^3 at y=3.1

B1 (6.265E+05 events)
cut efficiency 0.755429
H6 acceptance 4.7515E-08 µsr%

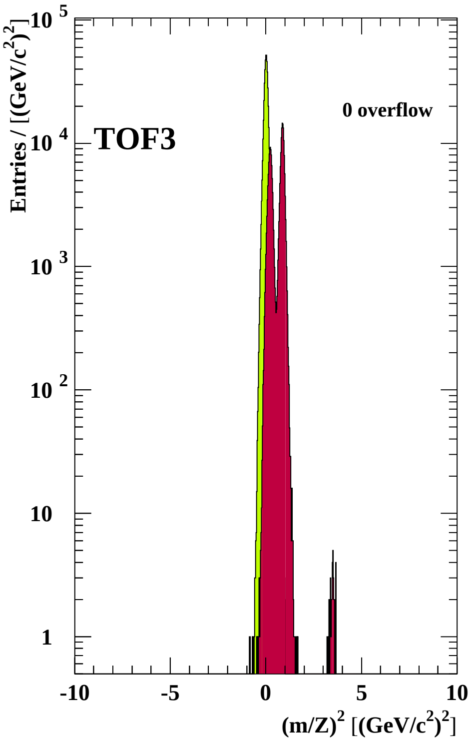

20B 4mm Pb

4.100E+11 Pb = 4.201E+10 int
1.049E+06 recorded events

C_press = 850 mbar
thr(m/Z) = 0.45 GeV/c^2

TOF3 **(5.956E+05 events)**
cut efficiency 0.774253
H6 acceptance 4.0375E-08 µsr%

k: 1.099E+06
1.714E+01 barn/GeV^{2}c^3 at y=4.4

ap: 1.312E+05
2.048E+00 barn/GeV^{2}c^3 at y=3.8

ad: 3.400E+01
5.324E-04 barn/GeV^{2}c^3 at y=3.1

B1 **(1.049E+06 events)**
cut efficiency 0.765672
H6 acceptance 4.7515E-08 µsr%

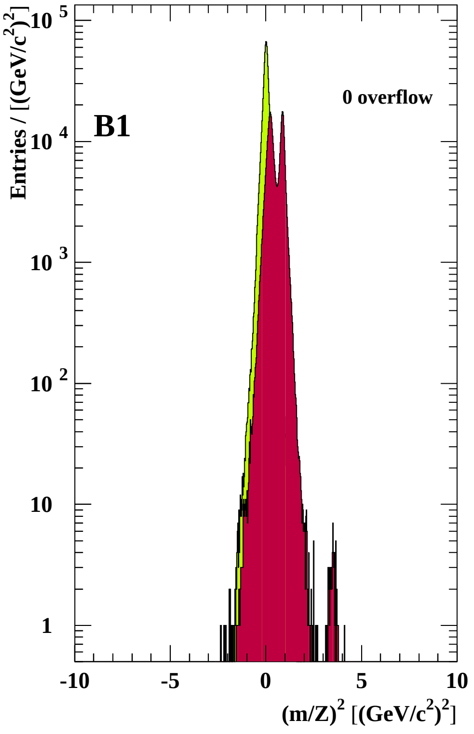

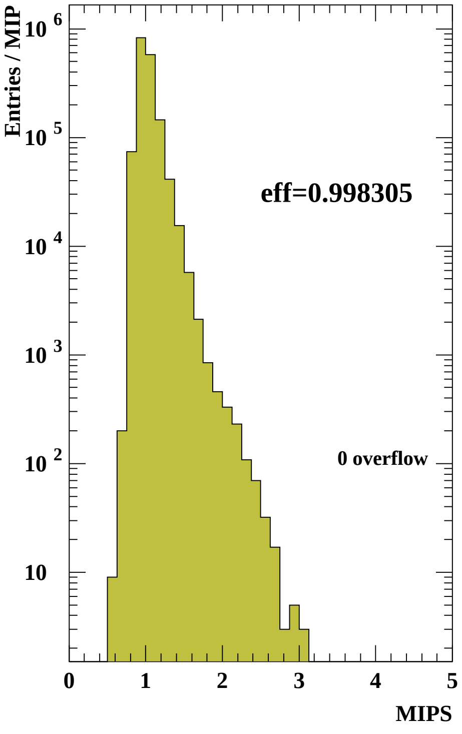

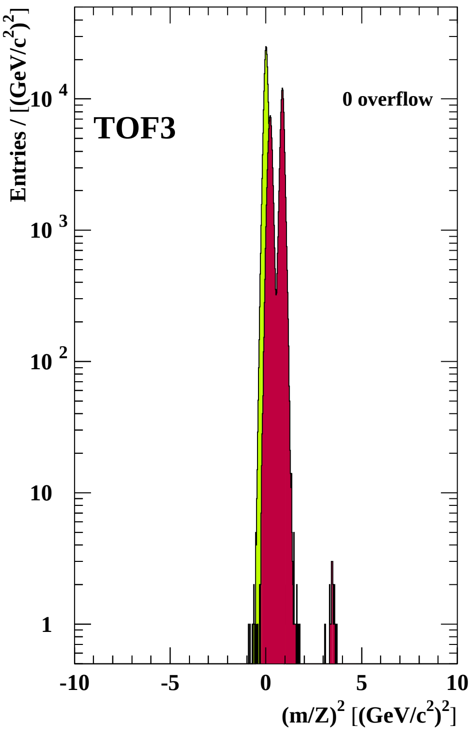

20C **8mm Pb**

2.070E+11 Pb = 4.025E+10 int

5.242E+05 recorded events

C_press = 850 mbar

thr(m/Z) = 0.45 GeV/c^2

TOF3 (2.919E+05 events)

cut efficiency 0.769781

H6 acceptance 4.0375E-08 μsr%

k: 8.872E+05

1.453E+01 barn/GeV^{2}c^3 at y=4.4

ap: 1.075E+05

1.762E+00 barn/GeV^{2}c^3 at y=3.8

ad: 2.600E+01

4.274E-04 barn/GeV^{2}c^3 at y=3.1

B1 (5.242E+05 events)

cut efficiency 0.761187

H6 acceptance 4.7515E-08 μsr%

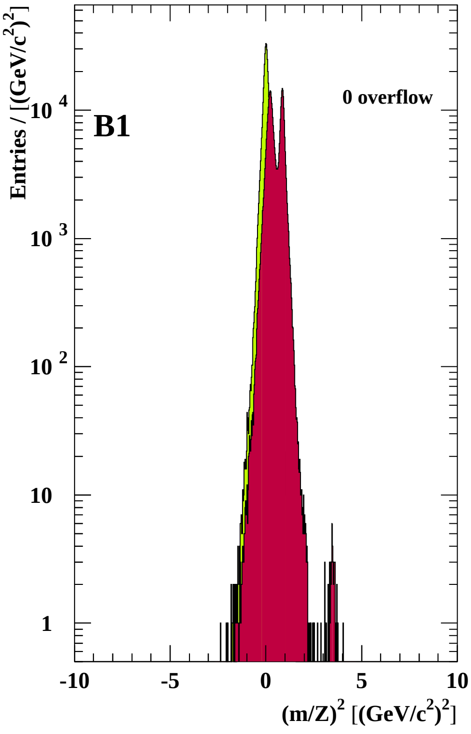

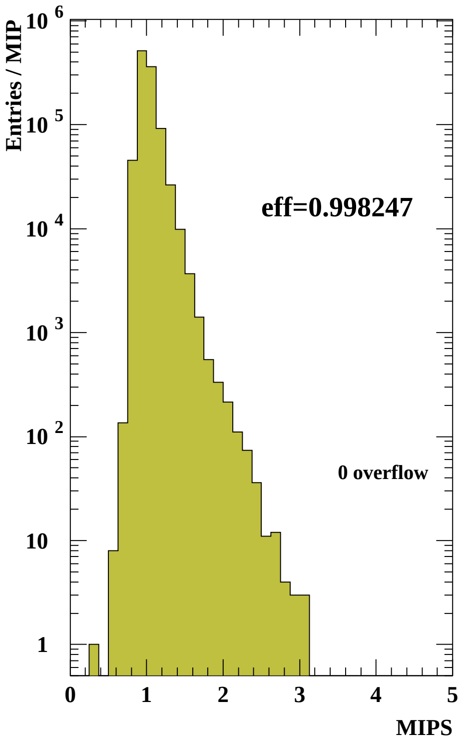

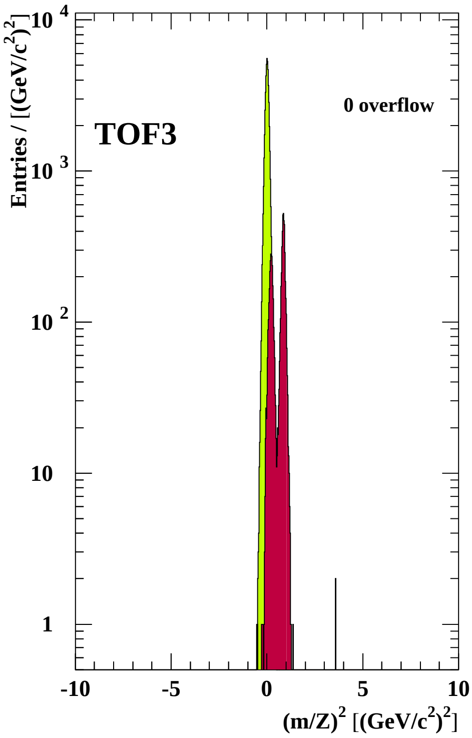

20D **0mm Pb**

3.440E+10 Pb = 0.000E+00 int

1.045E+05 recorded events

C_press = 850 mbar

thr(m/Z) = 0.45 GeV/c^2

TOF3 **(6.197E+04 events)**

cut efficiency 0.778904

H6 acceptance 4.0375E-08 μsr%

k: 3.222E+04

0.000E+00 barn/GeV^{2}c^3 at y=4.4

ap: 4.342E+03

0.000E+00 barn/GeV^{2}c^3 at y=3.8

ad: 2.000E+00

0.000E+00 barn/GeV^{2}c^3 at y=3.1

B1 **(1.045E+05 events)**

cut efficiency 0.771635

H6 acceptance 4.7515E-08 μsr%

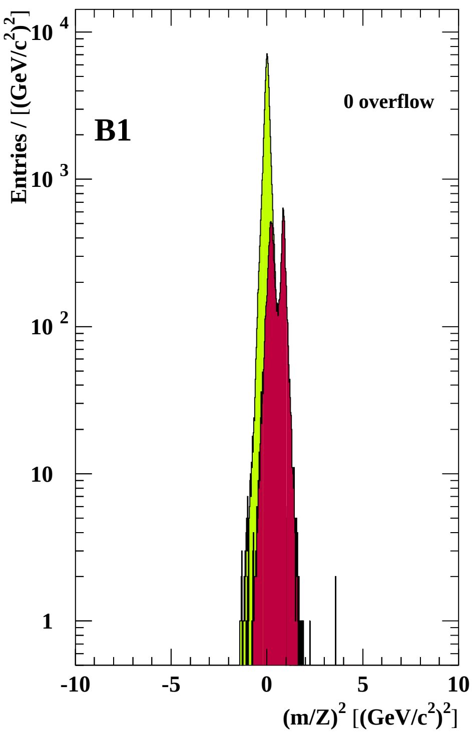

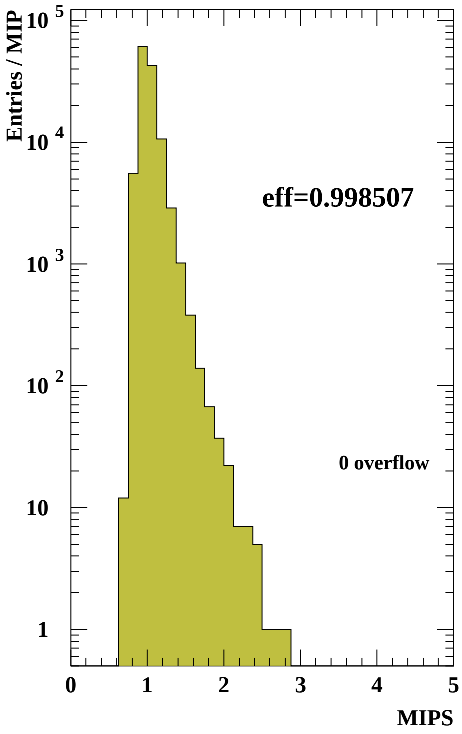

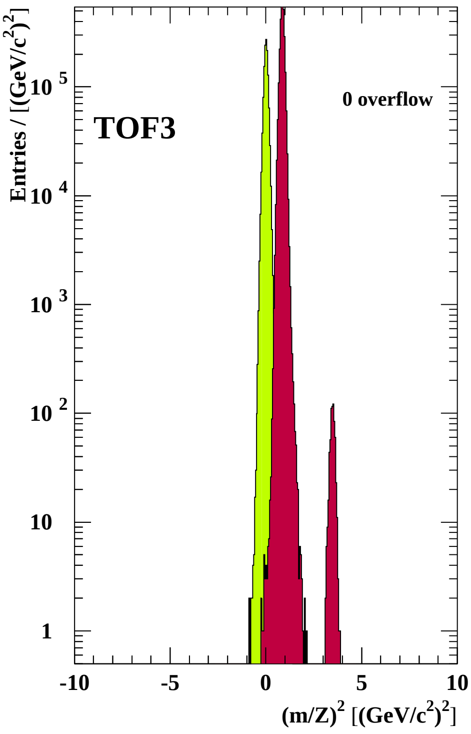

20T **40mm Pb**

1.290E+12 Pb = 8.524E+11 int

3.362E+06 recorded events

C_press = 3000 mbar

thr(m/Z) = 0.84 GeV/c^2

TOF3 (1.649E+06 events)

cut efficiency 0.770873

H6 acceptance 4.0375E-08 µsr%

ap: 3.191E+06

2.465E+00 barn/GeV^{2}c^3 at y=3.8

ad: 6.660E+02

5.162E-04 barn/GeV^{2}c^3 at y=3.1

ahe: 1.000E+00

1.495E-07 barn/GeV^{2}c^3 at y=3.4

B1 (3.362E+06 events)

cut efficiency 0.764995

H6 acceptance 4.7515E-08 µsr%

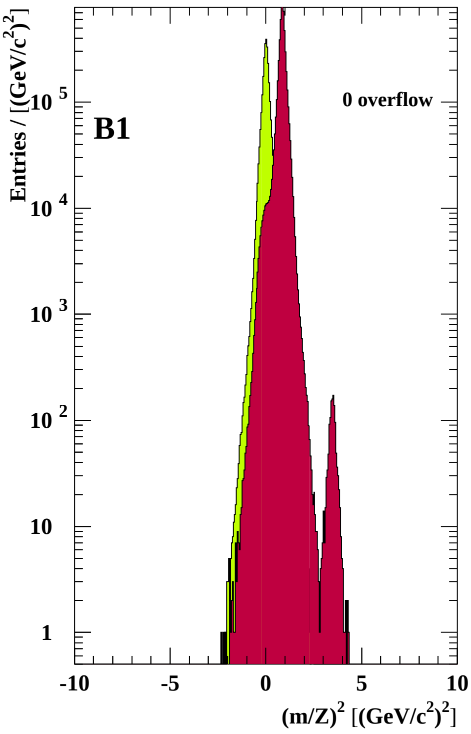

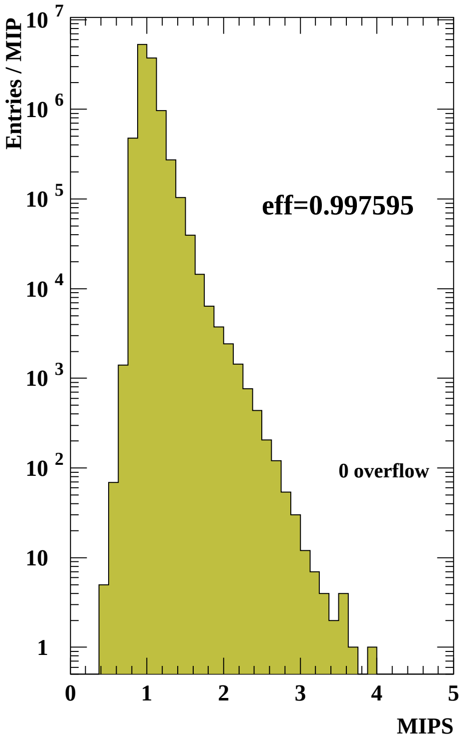

40A 40mm Pb

4.650E+11 Pb = 3.073E+11 int
1.437E+06 recorded events

C_press = 800 mbar
thr(m/Z) = 0.87 GeV/c^2

TOF3 (1.047E+06 events)
cut efficiency 0.78823
H6 acceptance 4.6325E-08 μsr%

ap: 2.168E+06
9.895E-01 barn/GeV^{2}c^3 at y=4.4

B1 (1.437E+06 events)
cut efficiency 0.787015
H6 acceptance 5.0235E-08 μsr%

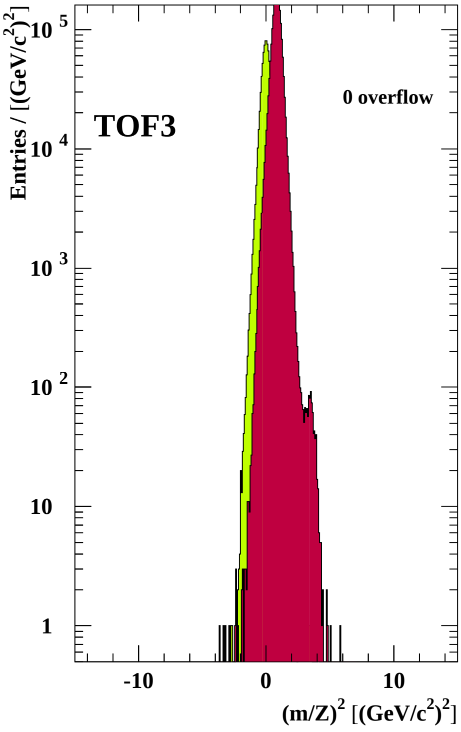

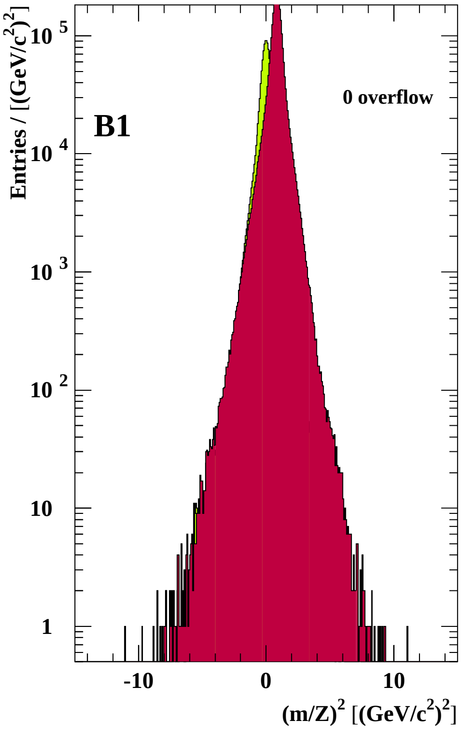

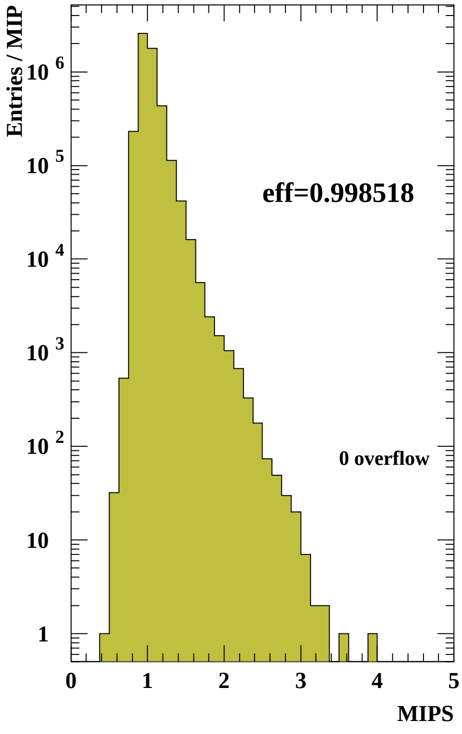

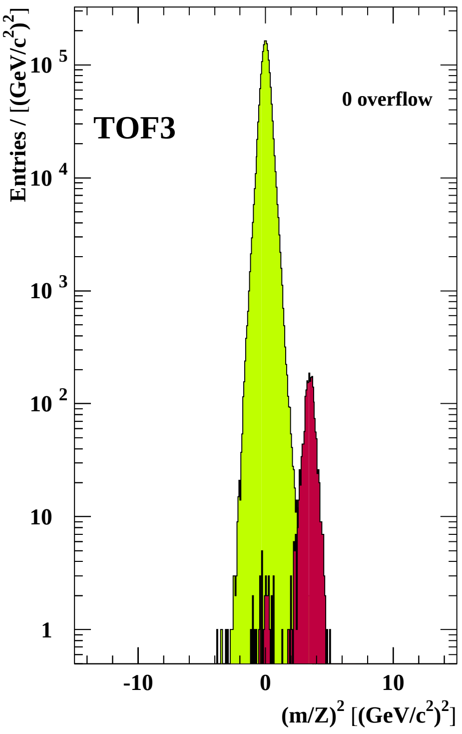

40B **40mm Pb**

1.450E+12 Pb = 9.581E+11 int
3.244E+06 recorded events

C_press = 1800 mbar
thr(m/Z) = 1.30 GeV/c^2

TOF3 (2.307E+06 events)
cut efficiency 0.742045
H6 acceptance 4.6325E-08 µsr%

ad: 2.049E+03
3.188E-04 barn/GeV^{2}c^3 at y=3.8

ahe: 3.000E+00
8.669E-08 barn/GeV^{2}c^3 at y=4.0

B1 (3.244E+06 events)
cut efficiency 0.742033
H6 acceptance 5.0235E-08 µsr%

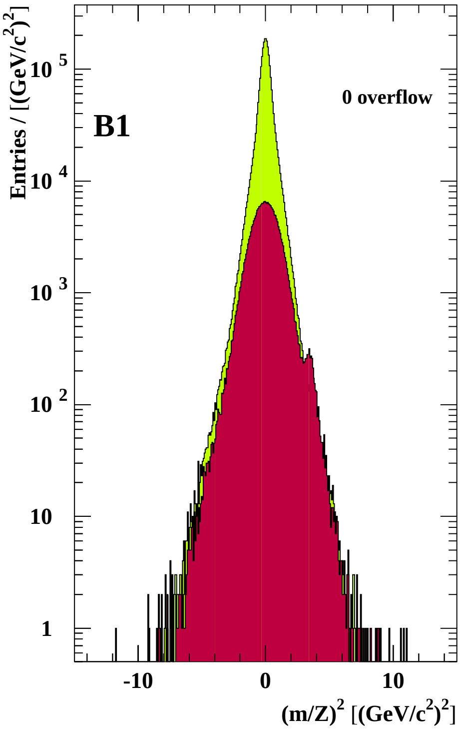

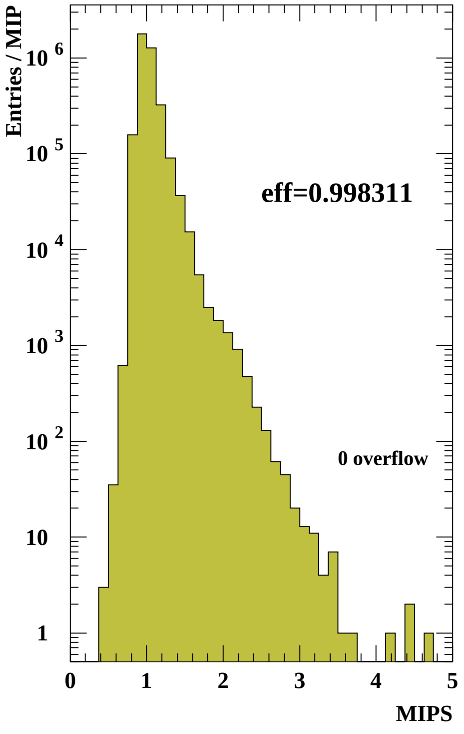

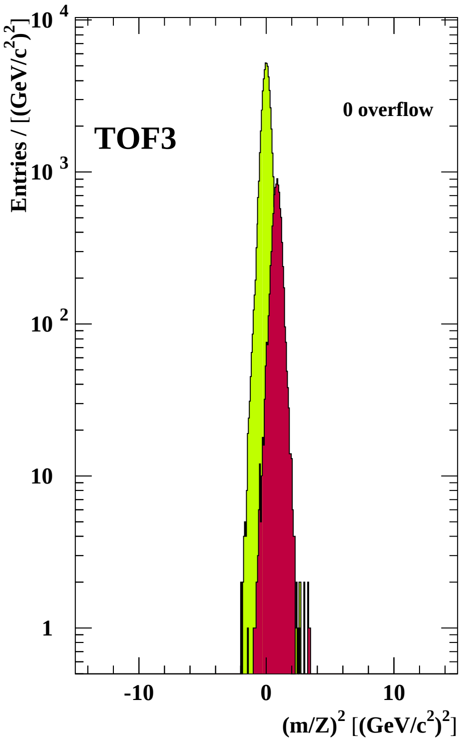

40C 0mm Pb

4.390E+10 Pb = 0.000E+00 int

9.886E+04 recorded events

C_press = 800 mbar

thr(m/Z) = 0.87 GeV/c^2

TOF3 (7.242E+04 events)

cut efficiency 0.73039

H6 acceptance 4.6325E-08 μsr%

ap: 9.080E+03

0.000E+00 barn/GeV^{2}c^3 at y=4.4

ad: 6.000E+00

0.000E+00 barn/GeV^{2}c^3 at y=3.8

B1 (9.886E+04 events)

cut efficiency 0.727503

H6 acceptance 5.0235E-08 μsr%

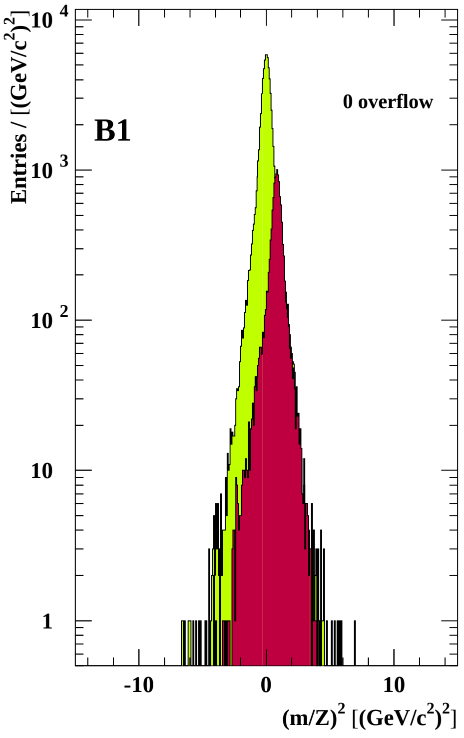

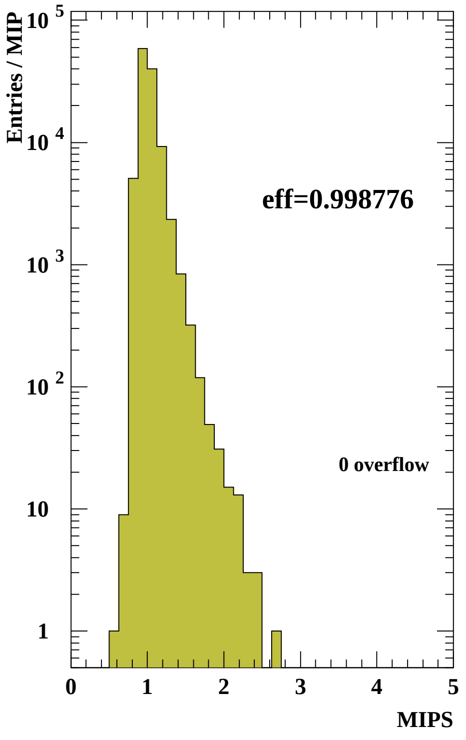

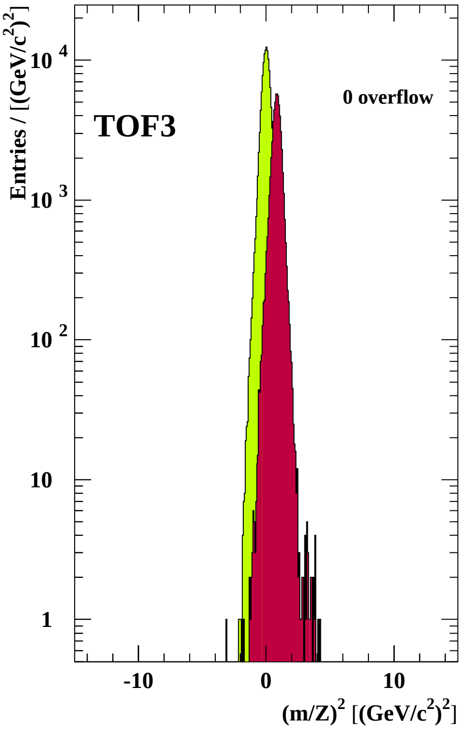

40D 8mm Pb

1.040E+11 Pb = 2.022E+10 int

2.313E+05 recorded events

C_press = 800 mbar

thr(m/Z) = 0.87 GeV/c^2

TOF3 (1.680E+05 events)

cut efficiency 0.744927

H6 acceptance 4.6325E-08 µsr%

ap: 5.928E+04

4.349E-01 barn/GeV^{2}c^3 at y=4.4

ad: 3.000E+01

2.203E-04 barn/GeV^{2}c^3 at y=3.8

B1 (2.313E+05 events)

cut efficiency 0.739979

H6 acceptance 5.0235E-08 µsr%

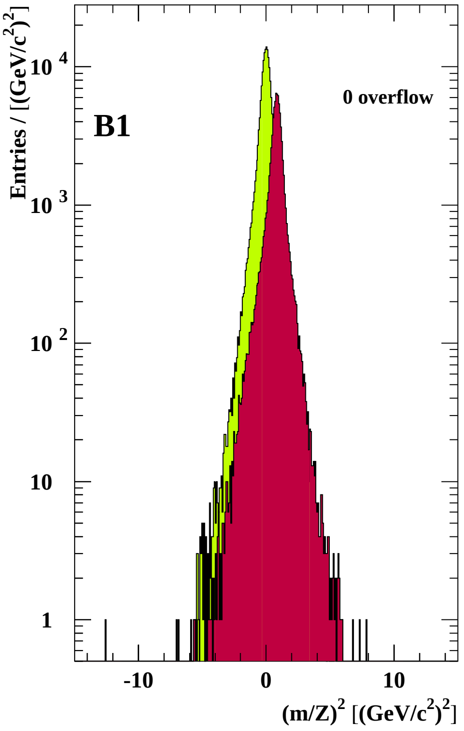

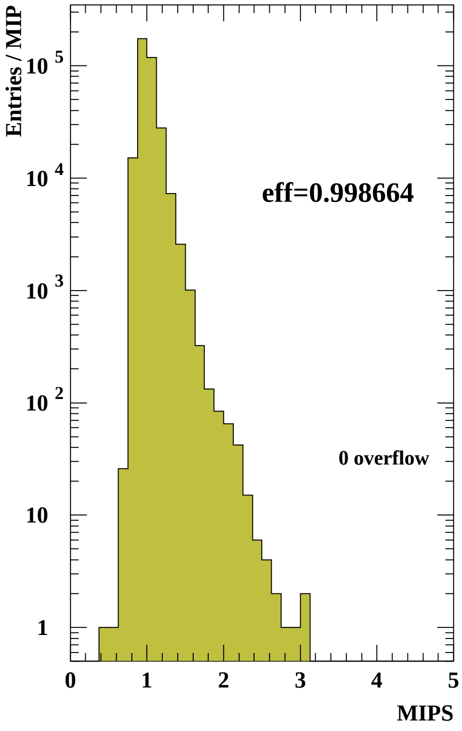

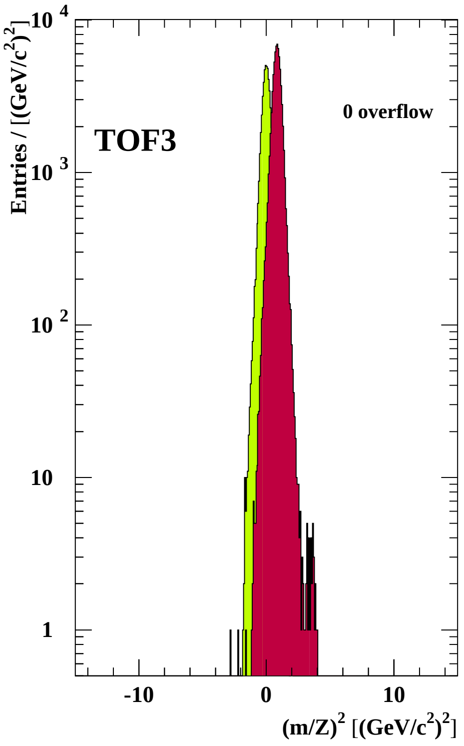

40E **16mm Pb**

4.850E+10 Pb = 1.703E+10 int
9.942E+04 recorded events

C_press = 800 mbar
thr(m/Z) = 0.87 GeV/c^2

TOF3 (7.174E+04 events)
cut efficiency 0.722346
H6 acceptance 4.6325E-08 µsr%

ap: 7.162E+04
6.436E-01 barn/GeV^{2}c^3 at y=4.4

ad: 3.300E+01
2.968E-04 barn/GeV^{2}c^3 at y=3.8

B1 (9.942E+04 events)
cut efficiency 0.719062
H6 acceptance 5.0235E-08 µsr%

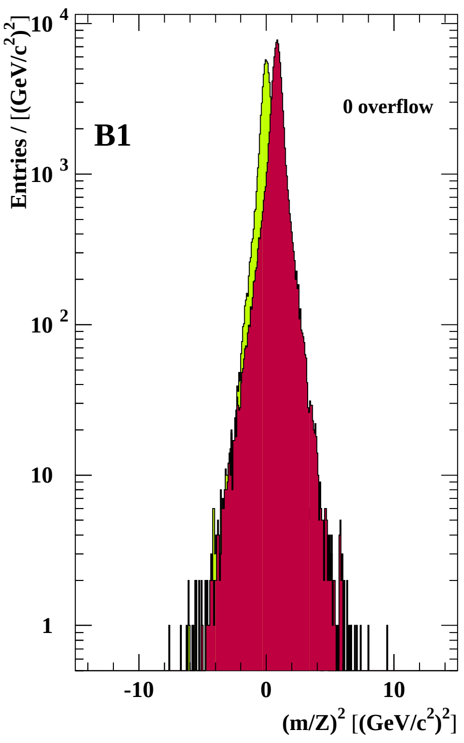

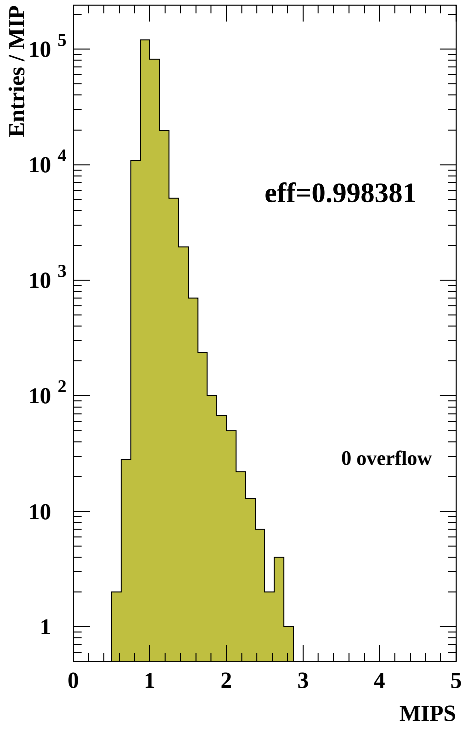

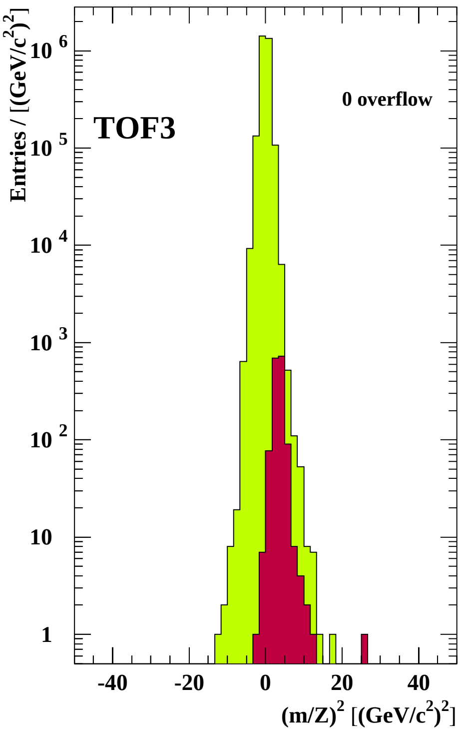

70C 40mm Pb

1.730E+12 Pb = 1.143E+12 int

5.001E+06 recorded events

C_press = 600 mbar

thr(m/Z) = 1.32 GeV/c^2

TOF3 (3.820E+06 events)

cut efficiency 0.787359

H6 acceptance 4.8195E-08 µsr%

ad: 1.601E+03

6.171E-05 barn/GeV^{2}c^3 at y=4.3

B1 (5.001E+06 events)

cut efficiency 0.783541

H6 acceptance 5.0745E-08 µsr%

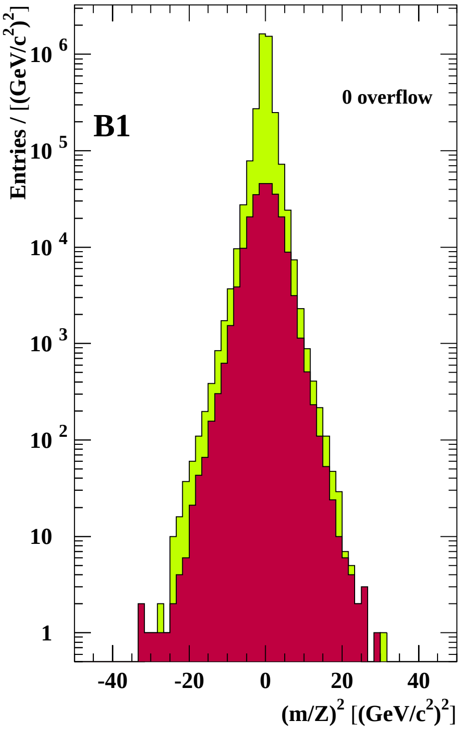

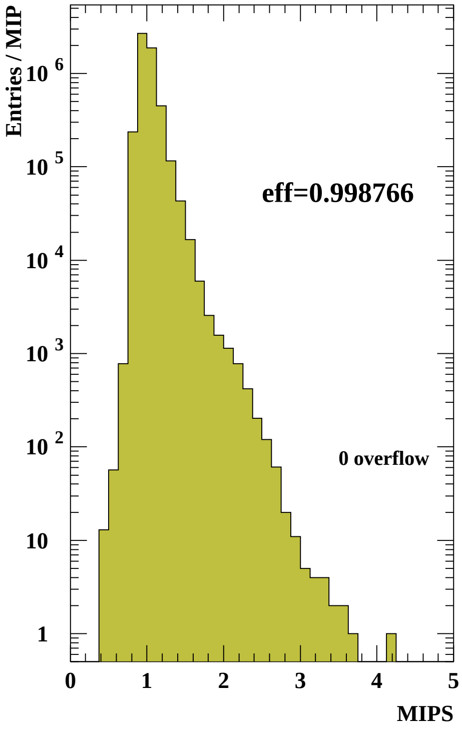

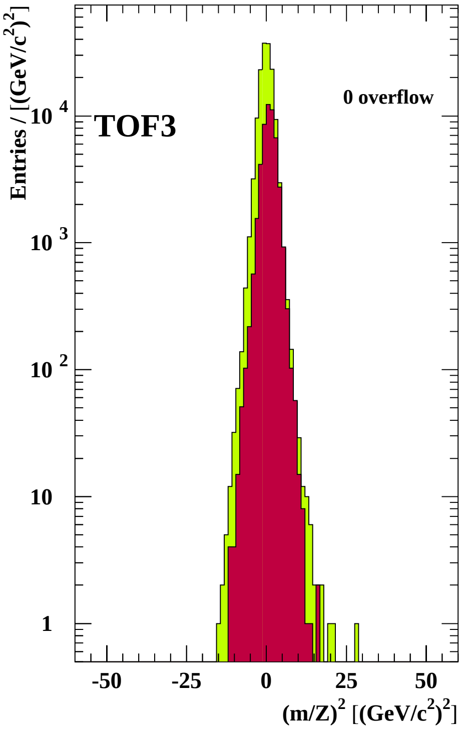

100E **16mm Pb**

1.070E+11 Pb = 3.756E+10 int

2.539E+05 recorded events

C_press = 130 mbar

thr(m/Z) = 0.87 GeV/c^2

TOF3 (2.042E+05 events)

cut efficiency 0.732814

H6 acceptance 4.8705E-08 µsr%

ap: 4.952E+04

3.025E-02 barn/GeV^2c^3 at y=5.4

B1 (2.539E+05 events)

cut efficiency 0.727197

H6 acceptance 5.0915E-08 µsr%

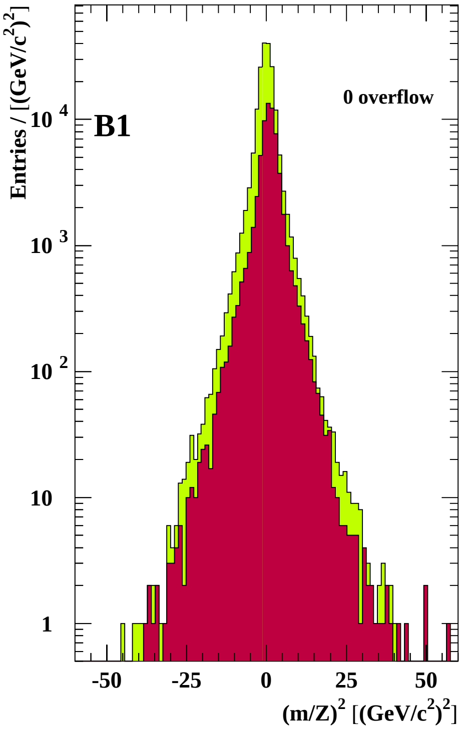

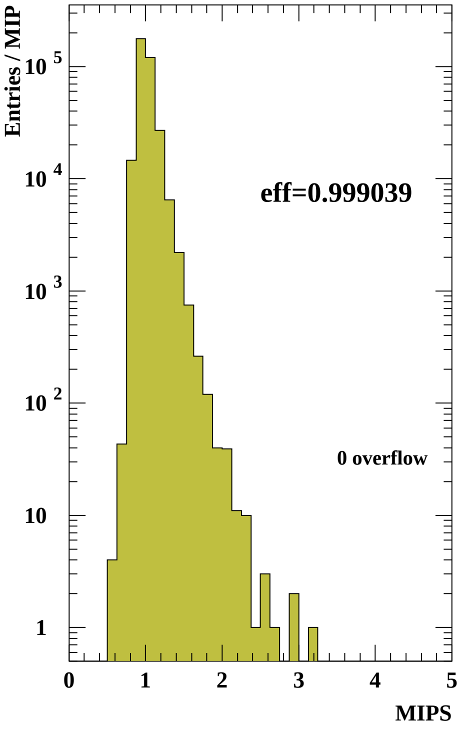

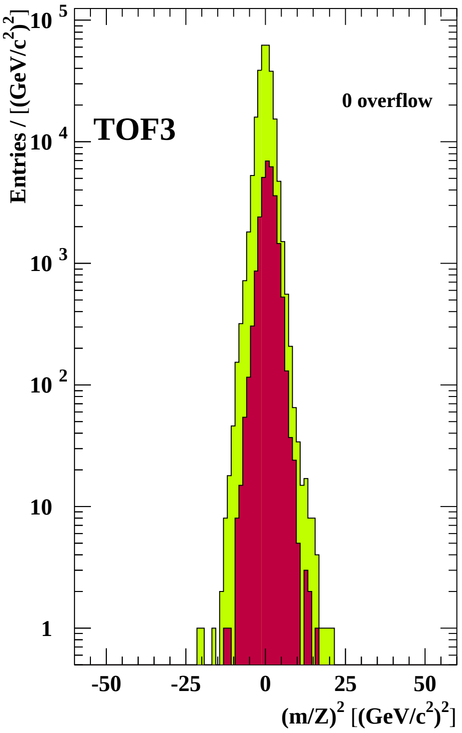

100F **4mm Pb**

1.550E+11 Pb = 1.588E+10 int
4.110E+05 recorded events

C_press = 130 mbar
thr(m/Z) = 0.87 GeV/c^2

TOF3 (3.304E+05 events)
cut efficiency 0.75394
H6 acceptance 4.8705E-08 µsr%

ap: 2.784E+04
3.909E-02 barn/GeV^{2}c^3 at y=5.4

B1 (4.110E+05 events)
cut efficiency 0.747634
H6 acceptance 5.0915E-08 µsr%

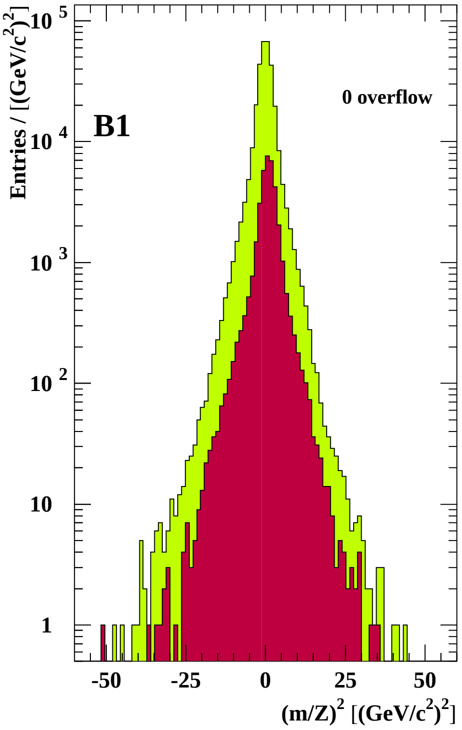

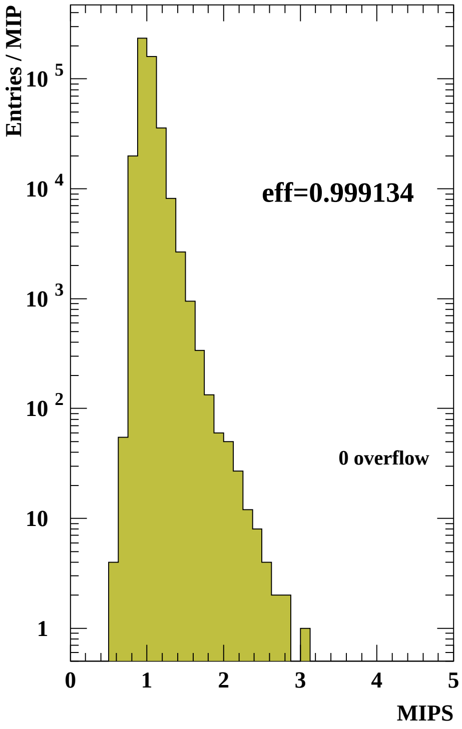

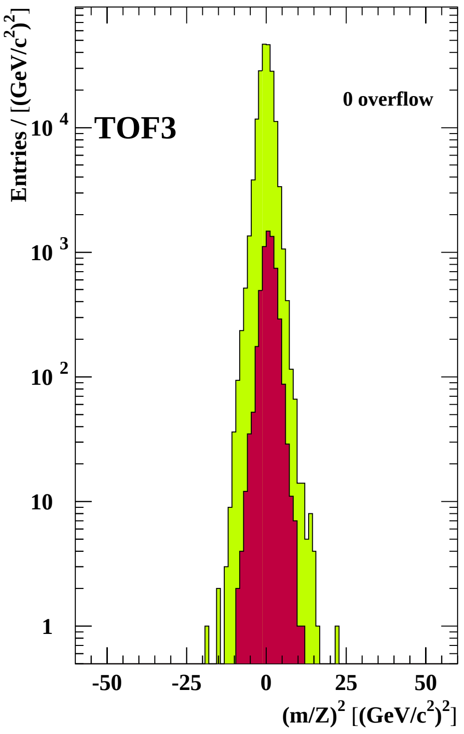

100G **0mm Pb**

1.170E+11 Pb = 0.000E+00 int

3.050E+05 recorded events

C_press = 130 mbar

thr(m/Z) = 0.87 GeV/c^2

TOF3 (2.454E+05 events)

cut efficiency 0.748656

H6 acceptance 4.8705E-08 μsr%

ap: 5.884E+03

0.000E+00 barn/GeV^{2}c^3 at y=5.4

B1 (3.050E+05 events)

cut efficiency 0.74217

H6 acceptance 5.0915E-08 μsr%

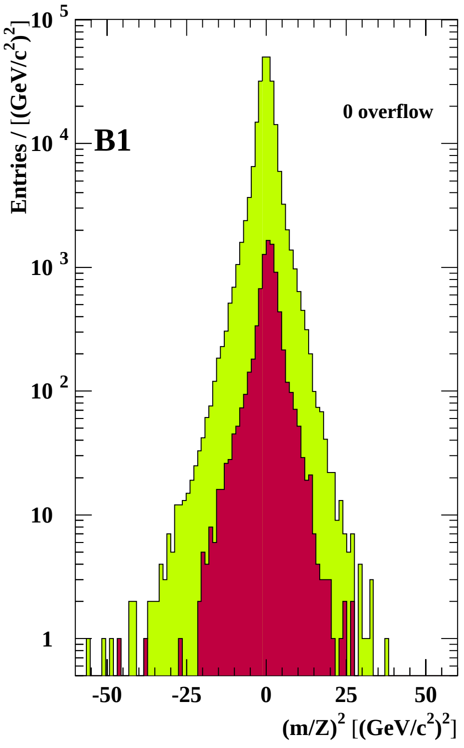

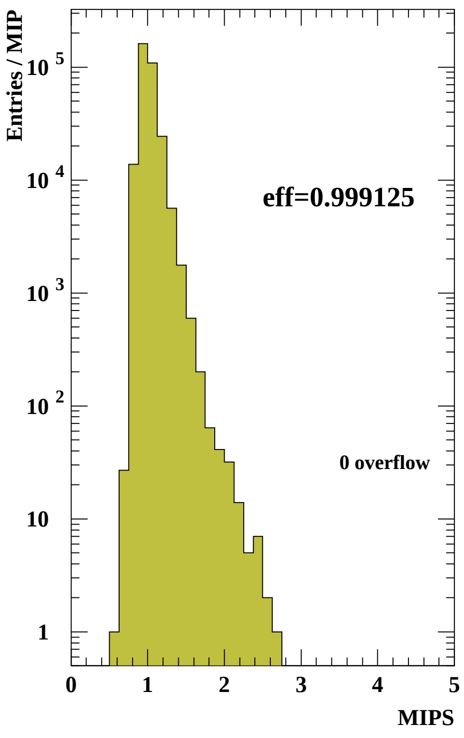

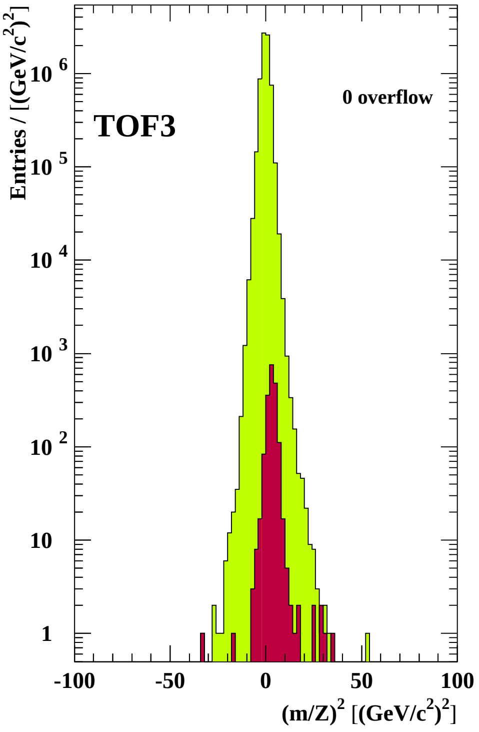

100T **40mm Pb**

3.330E+12 Pb = 2.200E+12 int

1.153E+07 recorded events

C_press = 300 mbar

thr(m/Z) = 1.33 GeV/c^2

TOF3 (9.207E+06 events)

cut efficiency 0.78831

H6 acceptance 4.8705E-08 µsr%

ad: 1.849E+03

1.793E-05 barn/GeV^{2}c^3 at y=4.7

B1 (1.153E+07 events)

cut efficiency 0.782532

H6 acceptance 5.0915E-08 µsr%

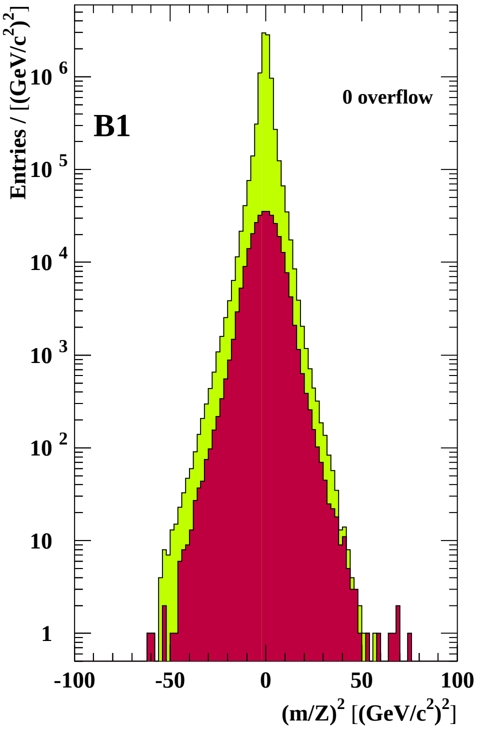

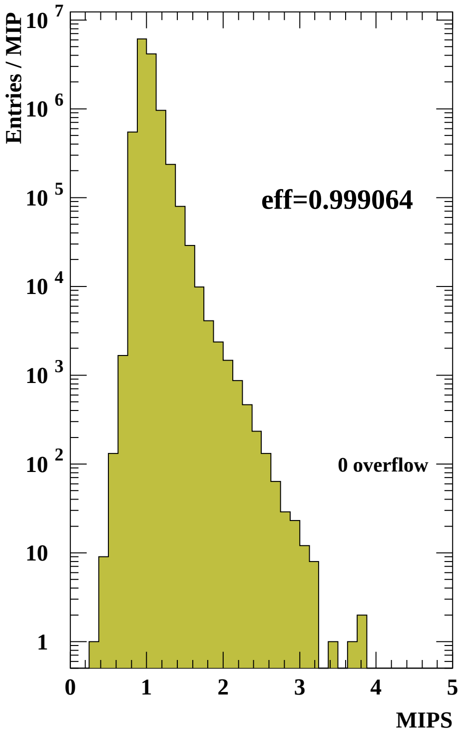

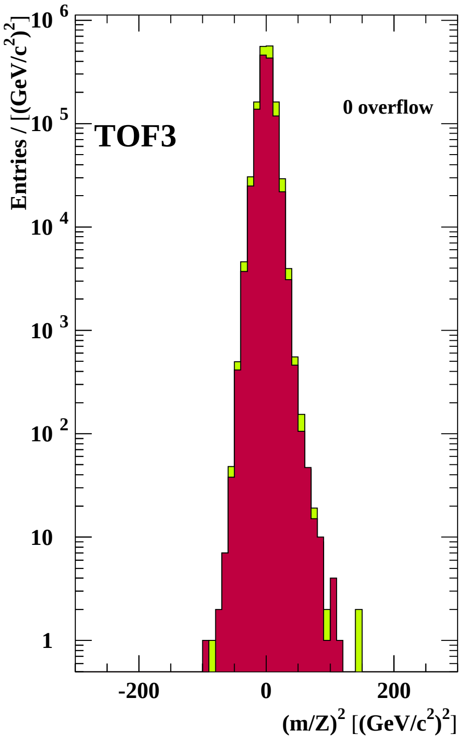

200A **40mm Pb**

1.140E+12 Pb = 7.533E+11 int

2.208E+06 recorded events

C_press = 30 mbar

thr(m/Z) = 0.84 GeV/c^2

TOF3 (1.895E+06 events)

cut efficiency 0.797595

H6 acceptance 4.9045E-08 µsr%

B1 (2.208E+06 events)

cut efficiency 0.791022

H6 acceptance 5.1085E-08 µsr%

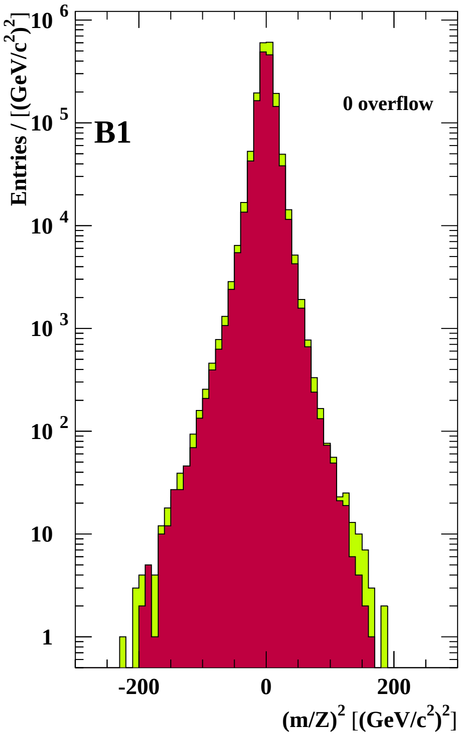

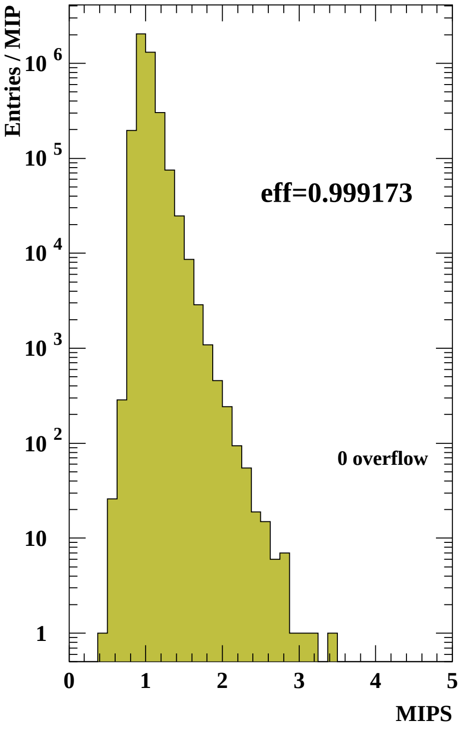

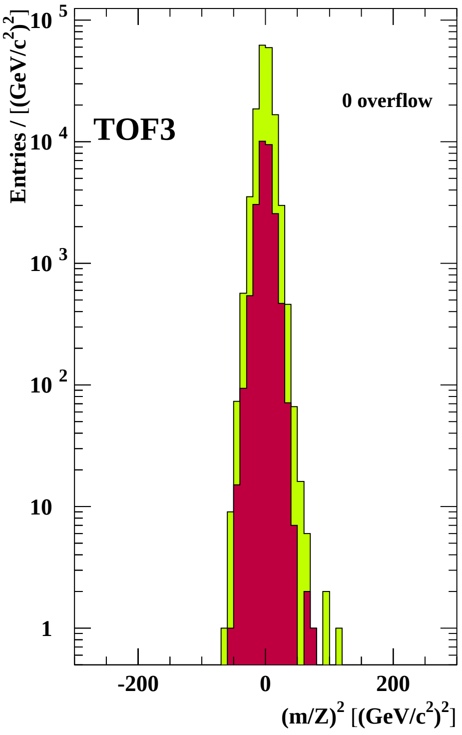

200B **40mm Pb**

1.250E+11 Pb = 8.260E+10 int

1.249E+05 recorded events

C_press = 30 mbar

thr(m/Z) = 0.84 GeV/c^2

TOF3 (1.077E+05 events)

cut efficiency 0.760433

H6 acceptance 4.9045E-08 µsr%

B1 (1.249E+05 events)

cut efficiency 0.753754

H6 acceptance 5.1085E-08 µsr%

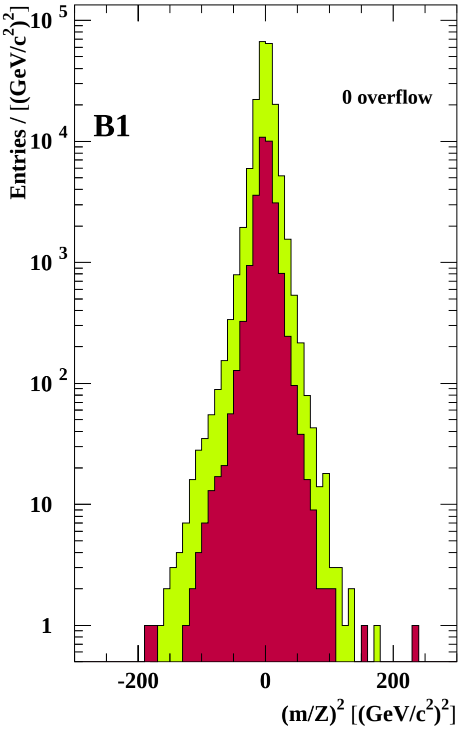

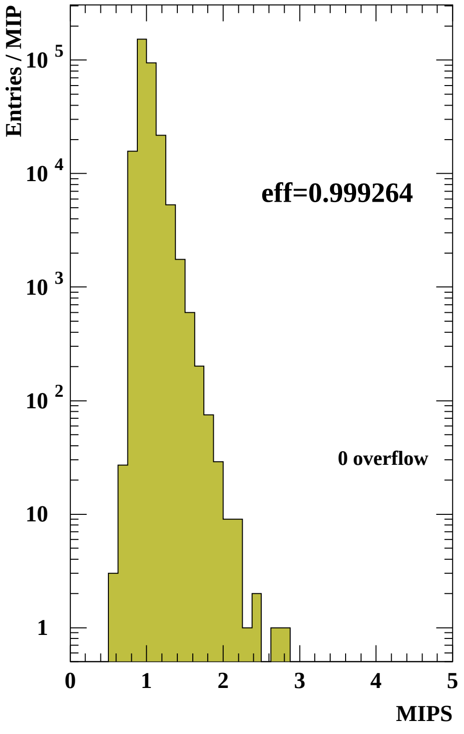

Acknowledgements

I would like to acknowledge all the people I spent the last years with.
It was a very pleasant and instructive time.
A big thank you to:

- Klaus Pretzl
- Anita and Bettina
- Reiner Klingenberg with Lili and Annika
- Urs Moser with Mirjana, Adi and Lara
- Remi and Dona Mommsen Ghosh
- Markus Hauser
- Luis Martinez
- Kurt Borer
- H.U.SCHütz, Simon Lehmann, Helmut Ruetsch and Fritz Nidegger
- Max Hess with Ursula, Matthias and Adrian
- Jean-Claude Roulin
- Jürg Schacher
- Irene Neeser
- Thomas Wälchli
- Christian Häberli
- Federico Hasenbalg with Paola
- Peter Oberli
- Sonja Kabana

- Peter Minkowski
- Konrad Elsener
- Jim Beam
- The NA52 collaboration
- The OPERA collaboration
- Christophe, Vreni, Luca and Kaspar Weber
- Kurt, Klärli, René, Dani und Martina Finger
- Hannes, Evi, Florian and Bernhard Heu-Brändli
- Heidi Brändli

Curriculum Vitae

Michele Weber

Birth:	November 11th, 1971 in Basel, Switzerland
Nationality:	Swiss
Marital status:	Married with Anita
Children:	Bettina, born November 18th, 1999

1978-1983	Elementary school in Bedigliora, Ticino
1983-1987	Secondary school in Bedigliora, Ticino
1987-1991	Gymnasium in Lugano, Ticino
1991-1995	Student of physics at the University of Bern
1995	Student exchange semester (Erasmus) Università Tor Vergata, Roma
1995-1997	Diploma student supervised by Prof.Dr.K.Pretzl at the Laboratory of High Energy Physics University of Bern
1997	Talk at CALOR'97, Tucson
1997-2001	PhD student supervised by Prof.Dr.K.Pretzl at the Laboratory of High Energy Physics University of Bern
1999	Talk at QM99, Torino
2000	Talk at S2000, Berkeley